Modeling Behaviour of Damaged Turbine Blades

for Engine Health Diagnostics and Prognostics

by

Jason Van Dyke

Thesis submitted to the Faculty of Graduate and Post Doctoral Studies as partial fulfillment for the degree of
M.A.Sc. in Mechanical Engineering

uOttawa

OTTAWA-CARELTON INSTITUTE

OF

MECHANICAL AND AEROSPACE ENGINEERING (OCIMAE)
UNIVERSITY OF OTTAWA CANADA
May 2011

Abstract

The reliability of modern gas turbine engines is largely maintained by careful damage tolerant design, a method of structural design based on the assumption that flaws (cracks) exist in any structure and continue to grow during use. With proper monitoring, largely in the form of periodic inspections at conservative intervals, reliability and safety are maintained. These methods, while reliable, can lead to the early retirement of some components and to unforeseeable failures if design assumptions fail to reflect reality. With improvements to sensor and computing technology, there is a growing interest in a system that could continuously monitor the health of structural aircraft components as well as forecast future damage in real-time.

Through the use of two-dimensional and three-dimensional numerical modeling, the initial goals and findings of the thesis include: (a) establishing measurable parameters directly linked to the health of the blade; and (b) assessing the feasibility of detecting damage to the blade and thermal barrier coating before they reach a critical size causing sudden failure.

The results of the thesis indicated that TBC-defects cause only minor changes to blade deformation and vibration frequencies which may not be detectable using current sensors. Crack damages also cause only minor changes to vibration frequencies. However, cracks can lead to substantial changes to blade deflexion and elongation in the range of 0.3 mm that can well be detected using standard sensors.

Changing modeling assumption from purely elastic to elastic-plastic material behaviour leads to larger changes in blade deflection and elongation particularly above the transition temperature where the material strength drops strongly with temperature. Changes in blade deflection are expected to be much larger since cracks lead to higher local temperatures which can then result in large creep deformation over time.

The primary limitation of the study is the lack of relation to statistical variation in blade demand and vibration. Therefore, it is difficult at this point to conclude whether the changes determined here are large enough to be isolated from the natural noise in blade vibration and deformation during use. Future work could focus on this aspect.

Contents

List of Tables

List of Figures

1 Motivation and Objectives of the Project

It has been well established in literature that the mechanical behaviour of a turbine blade, particularly the characteristics of the blade's vibration changes as damage is accumulated. This change is the result of a change in effective stiffness or flexibility of the blade which in turn reduces the natural vibrational frequency, and increases the blade deflection and elongation.

Thermal barrier coating (TBC) and advanced cooling techniques are common in today's turbines allowing blades to operate at gas temperatures higher than the structural limit of the material. This has made the operational lifetime of many turbine blades dependent on the performance of the TBC. However detection of TBC failure, or the onset of such a failure for a health monitoring system is relatively unexplored. While some techniques are capable of tracking this damage in lab conditions, no technology exists to track the onset of TBC damage in real-time within an operational gas turbine to date.

This project looks to explore the effects of damage on a coated turbine blade by constructing a series of FEA models each with varying degrees of damage. The solution to these models can be studied and parameters such as tip deflection and natural vibrational frequency used studied to establish a clear relationship with the modeled damage. The onset of TBC damage requires the modeling of mechanisms that occur on a very small scale and thus are not useful to incorporate in this study concentrating on larger measurable parameters relating to the damage. Instead, the project concentrates on the immediate effect caused by the TBC detaching from the blade (spallation). Previous studies linking crack damage to deflection and natural frequencies neglect the complex temperature distribution of a coated turbine blade and the associated TBC loss at the crack tip. This project aims to investigate the overall effects of damage by (a) establishing measurable parameters directly linked to the health of the turbine blades and (b) studying the feasibility of detecting accumulated damage to the structural material and thermal barrier coating as well as the onset of damage causing structural failure.

2 Introduction

Aerospace represents the height of engineering design. The industry has pushed the limits of materials, thermodynamics, and aerodynamics design while maintaining nearly unmatched reliability and safety.

Currently the design and life time prediction of aircraft components are largely based on fatigue mechanisms. Fatigue is the process by which cyclic loading of components initiates damage in the form of small surface cracks. Under continued loading these small cracks may propagate to a size that will weaken the component sufficiently to cause fracture.

There are several design approaches:

- Infinite life design - Provides unlimited safety as the design stresses are below the endurance/fatigue limit.
- Safe Life design – Use a designed finite life modified with a safety factor.
- Fail safe design – Assumes cracks exist and will propagate but structures retain sufficient residual strength until inspection and repair.
- Damage Tolerant design – A refinement of failsafe philosophy; crack growth is modeled and inspections/maintenance are scheduled to insure component maintains adequate residual strength until repair or replacement.

Most aircraft components are designed using damage tolerance allowing the complex system to be maintained economically without sacrificing safety. Damage as defined by damage tolerant design occurs in two categories, Slow Crack Growth (SCG), and Fail safe (FS). Under Slow Crack growth concept structures are designed such that initial damage will grow at slow, stable rate, during the service life time of the component. During this service lifetime the crack will never reach a size capable of causing rapid unstable propagation. Damage tolerance and safety is assured by:

- Maintaining a slow crack growth rate.
- Assuring residual strength capacity.
- Assuring that sub-critical crack damage will be: detected by inspection or, never reach unstable size before the component is replaced.

To design a damage tolerant component the following information must be established: (1) the residual strength of the component as a function of crack size; (2) the permissible crack size; (3) the time it takes a crack of permissible size to develop from a flaw of known size; (4) the interval of inspection, proof testing or replacement.

Structural parts are declared to be unsafe or unfit for service when the possibility of a crack growing to the point of component failure becomes foreseeable. This calculation, based on data collected largely from empirical tests, establishes the usable lifetime of a part. The more difficult a part is to inspect or proof test, the more conservative the lifetime estimation becomes. In addition to a more conservative service lifetime, more difficult to inspect parts are often replaced independent of their damage state at the end of the pre-set service life resulting in a large number of areoengine parts being retired without developing any significant damage. Another disadvantage of this conservative method is that it may fail to accommodate unforeseeable circumstances. For example a manufacturing defect within a part can cause the initiation and growth of cracks earlier than expected. This would effectively reduce the lifetime of the component and possibly cause failure before the designed maintenance period with catastrophic results [1-5].

A component can be made safer and more damage tolerant if it can be inspected or maintained easily, insuring the residual strength of the component is sufficient for service and thus effectively increasing the service life of the component. In practice this is difficult as frequent inspections and maintenance lead to large periods of aircraft downtime.

If a components residual strength or health could be evaluated and its remaining service life calculated continuously, it would obviously be possible to: (1) increase their service life; (2) improve maintenance scheduling and reduce aircraft downtime; and (3) increase their reliability through continuous re-evaluation of their service life [2]. Overall, an integrated diagnostic and prognostic health management system can contribute to increase the efficiency and reliability of the damage tolerant design. Such a system must be capable of predicting in real-time, within a specified confidence, the remaining time to failure of critical engine components [3].

3 Literature Review

3.1 Introduction to Gas Turbine Engines

A gas turbine is a rotary engine that extracts energy form the flow of expanding gases. In order to produce this expansion a pressure ratio must be provided by first compressing the working fluid in a compression stage. Heat is then added to the compressed fluid, typically through combusting fuel. The hot working fluid is expanded through the "hot" turbine stage where work is extracted producing enough power to produce usable work in addition to powering the compression stage. This usable work in terms of aero-engines is typically used to power a propeller (shaft power) or thrust as can be seen in Figure 1.

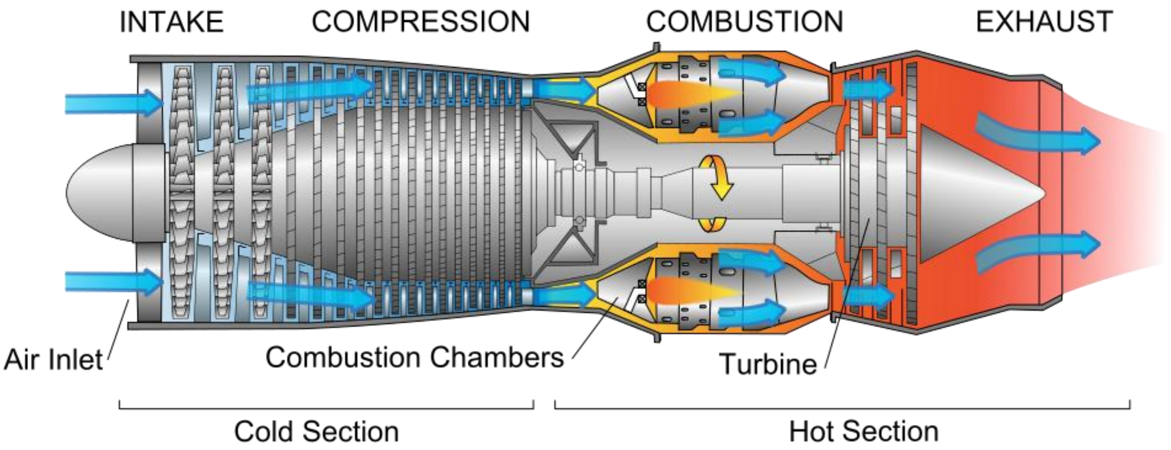

Figure 1: Axial gas turbine engine

3.2 Integrated Prognostic and Diagnostic Health Management Systems

Currently systems used in modern military aircrafts are capable of basic prognostic (predictive) health management. The system monitors sensors located in the engine during its operation for thermal and mechanical stresses. These measured parameters are related to known healthy engine parameters or operational limits. By comparing the sensor data the onboard system determines the state of the component and assesses the damage accumulated during operation from engine operating conditions (ie. turbine rpm, gas path analysis including temperature) [1, 4]. The actual operational state of individual components can be extrapolated from these data and compared to either theoretical damage progression data or databases of historically defined failure modes and damage progression. Fuzzy logic and neural network algorithms, capable of "human like" experiential learning may also be used to calculate this real time damage accumulation and thus become more accurate over time [3].

The basic knowledge needed for a component to operate in a prognostic/diagnostic system is:

- The failure mode; including the damage mechanism and measurable parameters symptomatic of incurred damage.
- The Location of the component including features, details, and operational dependencies.
- Methodology for determining the exact operational conditions and calculating the damage accumulated from measurable parameters. This requires the development of empirical or physical models [1].

From these basic elements it is possible to establish measurable engine damage indicators which can be transmitted, stored, and analysed by both onboard and ground based systems. Generally the onboard systems calculate and monitor the accumulated damage of a component, track individual component life, and assess the overall health of the engine. The ground based systems store the data for fleet wide access, predicts component life, communicates with fleet logistics, and schedules future maintenance [3, 6].

With advances in sensor technology it is becoming increasingly possible to monitor particular critical locations within a gas turbine that due to extreme operating environment have previously been impossible. Comparing the data to theoretical and measured engine parameters the real-time damage for a critical location can be calculated to an even greater degree of accuracy. A prime example of this would be the blades located in the hot section of an operating turbine which are subjected to high temperatures, static and cyclic stresses, aggressive environments, and foreign object damage.

The present system lacks predictive ability and cannot identify the actual cause of damage or its location. Improvements to future systems rely on enhanced diagnostic and prognostic algorithms to fuse information from multiple diagnostic sources together to provide a more confident diagnosis, estimate the importance of associated events, and provide synergistic integration with ground based maintenance and logistics [3, 6].

3.3 Technical Development of Systems

In order to develop a more robust diagnostic and prognostic system a probabilistic framework is desirable as any prognostic result reported from such systems needs an associated confidence interval. To eliminate the possibility of sensor malfunctions, diagnostic algorithms must collect and fuse data from a variety of sources to improve fault detection. For example information from measured vibration data, performance parameters, and oil related measurements are processed and compared to detect a bearing fault with a high degree of certainty [3].

To obtain a high level of certainty within collected data, the robustness of the sensor and signal processing system is critical. Sensor validation and diagnostics techniques fall in two categories; signal processing-based and physics-based. Signal processing techniques detect and diagnose sensor anomalies, independent of the monitoring system characteristics. The physics based techniques accomplish the actual sensor recovery and “virtually sense” component parameters, (ie. the stiffness of a turbine blade through blade-tip displacement). Information from the two techniques are combined by comparing the two signals eliminating errors such as sensor "spiking" which could otherwise be interpreted as a fault [6].

Another important aspect for fault detection is the establishment of a statistical engine baseline model. This is accomplished through physics based engineering analysis and/or computer simulation of the operating engine. The developed model is used to establish a "baseline" data representing the "normal" operating conditions of the engine. Any statistical deviations from the model are used to detect engine faults. Prognostic elements are introduced by monitoring the shift in engine performance. Algorithms are used to analyse the shift in performance and compare to shifts associated with engine degradation [3].

By continually tracking significant parameters such as flow, vibration, operating temperature, etc, of a degrading system and reincorporating the data with the baseline data the robustness of the system is increased. Effective database storage and mining can also be used to create, or reinforce a “baseline” model. An effective database would be capable of storing for analysis: fault trends, damage accumulation, significant operating conditions, and a log of all anomalies [7]. With the formation of a fleet wide data base comparison, an analysis can be done on components with a variety of operational histories. To make an effective prediction on the future lifetime of a component, data capable of trending future engine usage must also be monitored.

3.3.1 Modeling of a Component

Traditionally a physics-based stochastic model is used for component failure mode prognostics. The model is used to evaluate a statistical distribution of remaining useful component life dependent on the component's strength and stress condition. The results from the model are used as a basis to create a neural network or probabilistic based autonomous system to predict, in real-time, failure of the component [3].

Predictions made from the prognostic model can be further divided into failure and condition prognostics [3]. Failure prognostics typically refer to the continuous damage accumulated in a component, or system of components, with or without the presence of any identified faults. Components designed using crack initiation concepts often fit into this category. Condition prognostics are most often associated with faults being diagnosed prior to a vibration or performance-related limit being exceeded. Detected faults are diagnosed for cause and severity so the remaining useful life can be determined. The useful life is defined as the time between this fault detection and the failure condition of the component (see section 3.4.3 *Time-Dependent Crack Growth and Damage Tolerance*).

A physics based model typically incorporates mechanical and thermodynamic deterministic models as their basis. For a model to be of reliable use for in-service engines it must incorporate the statistical variability of parameters affecting the lifetime of the component [3]. Typical factors include material data, dynamic loading, and difference in operational conditions. Analysing possible combinations of theses parameters with appropriate lifetime calculations can yield a distribution for the predicted lifetime of the component. By incorporating data from the continuous monitoring of operational conditions, parameter evolution, and performed maintenance, life predictions can be re-evaluated and updated [4, 6]. More advanced models should be able to predict the evolution of limiting parameters and diagnose the propagating failure mode type.

All deterministic models need to be calibrated/verified using in service data. For example a finite element model should incorporate known crack initiation regions from infield experience and inspection data. Models based on empirical tests should have clear relationships between measured parameters, damage accumulation, and diagnosed fault severity.

3.4 Fracture Mechanics and Damage Tolerant Design

3.4.1 Basics - Failure Prevention

Components and structures can fail in a variety of modes:

- General yielding or excessive plastic deformation.
- Buckling or general instability.
- Sub-critical crack growth. Initiated by fatigue, stress corrosion, or corrosion fatigue leading to a loss of section or unstable crack growth.
- Unstable crack growth leading to partial or complete failure.
- Corrosion or creep.

Yielding and buckling occur over very short time spans and are typically caused by either under design or overload. Creep, corrosion, and crack growth, typically occur over larger time frames. While failures in yielding and buckling modes do occur and can be catastrophic, they are in the minority of engineering failures. Most failures occur from progressive damage and fatigue/crack growth related processes [8].

Fracture control is used to ensure the safe operation of structures without catastrophic failure. The susceptibility of a structure to fracture is affected by 3 primary factors:

- The fracture toughness of the material.
- Size, shape and orientation of crack.
- Applied stress.

This can be contrasted with strength of materials approach which considers only the applied stress and the yield or ultimate tensile strength of the material [9].

The level of fracture control applied during design depends on how critical the component or structure is, what the economic consequences are if the structure is out of service, what damage could be caused by failure, and most importantly, what is the potential for loss of life? Once this has been defined the structure can be designed to be more or less damage tolerant.

3.4.2 Fracture Mechanics

Three fundamental modes of crack propagation exist as shown in Figure 2. Mode I facture, the tensile or opening mode is the principal mode of crack loading observed and the mode that is most often considered in design. In fact, improvements with respect to mode I fracture resistance also lead to improvements regarding the fracture resistance in multiple mode cases. Sliding (mode 2), tearing (mode 3) and multimode fractures do exist, but they are relatively uncommon [10].

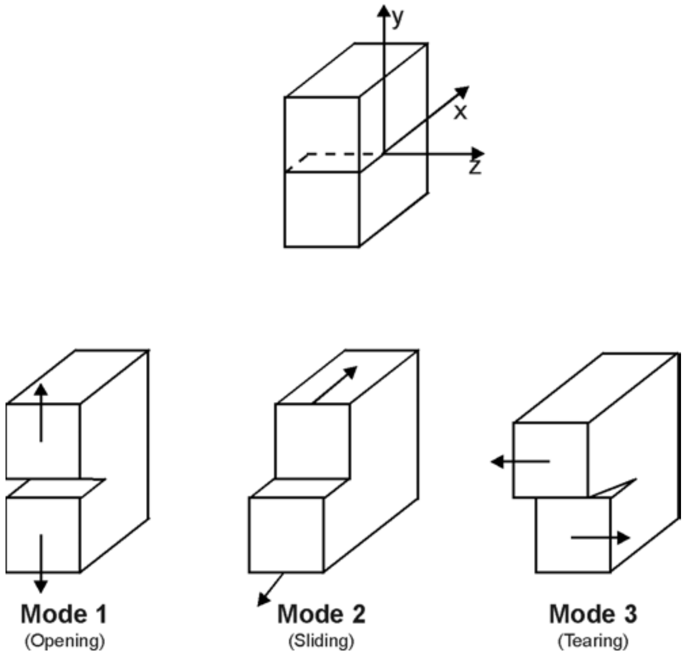

Figure 2: Crack loading modes [10, 11]

The stress intensity model is based on the use of linear elastic stress analysis, and thus assumes that any localised plastic deformation is small and considered within the elastic stress field [10, 11]. Figure 3 shows the stress present on an element near a crack of length 2*a* in mode I extension. A nominal stress σ exists in the element of thickness *B.* The stress intensity factor K_i quantifies the stress at the crack tip (points A and B) in linear elastic materials. If it is assumed that the material fails locally at a critical stress, then it stands to reason that there is a critical stresses intensity K_{ic}. Thus when $K=K_{ic}$ unstable crack growth occurs resulting in uncontrollable fracture. This critical stress intensity factor can be used to measure the fracture toughness of a material. The general equation that determines K_i is given by [10, 11]:

$$K_I = \sigma\beta\sqrt{\pi a}$$

Where *β* is used to relate the gross geometrical features to the stress intensity factors. Note that *β* can be a function of crack length (*a*) as well as other factors [10].

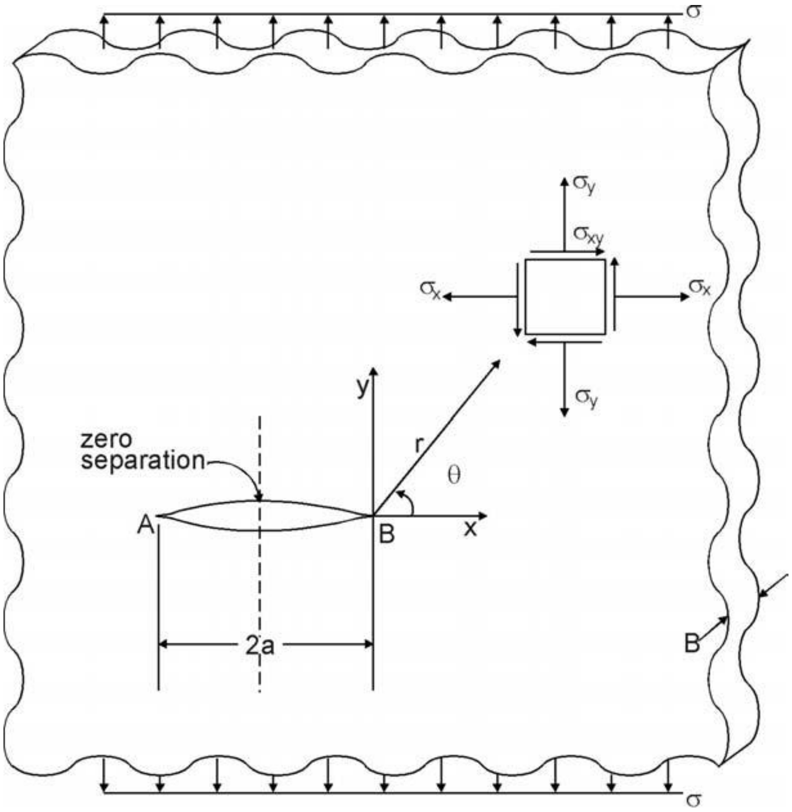

Figure 3: Stresses near the tip of a crack in an elastic material [10]

3.4.3 Time-Dependent Crack Growth and Damage Tolerance

Fracture mechanics play a key role in the life time prediction of components that are subject to time dependent crack growth mechanisms such as fatigue or stress corrosion cracking [10, 11]. Experience and testing have shown that, in the case of tough materials such as turbine blades, the time taken for crack initiation relative to the overall lifetime of a component is relatively small (5%). During the remaining lifetime of the component, initiated cracks continue to grow until eventually a critical size (a_c) is achieved, at which point sudden fracture occurs [10]. The rate of this cracking or damage accumulation can be described by the empirical Paris equation [10, 11]:

$$\frac{da}{dN} = C \ \Delta K^{m}$$

Where da/dN is the crack growth per cycle; *ΔK* is the stress intensity range; and *C* and m are material constants. The principle is illustrated in Figure 4.

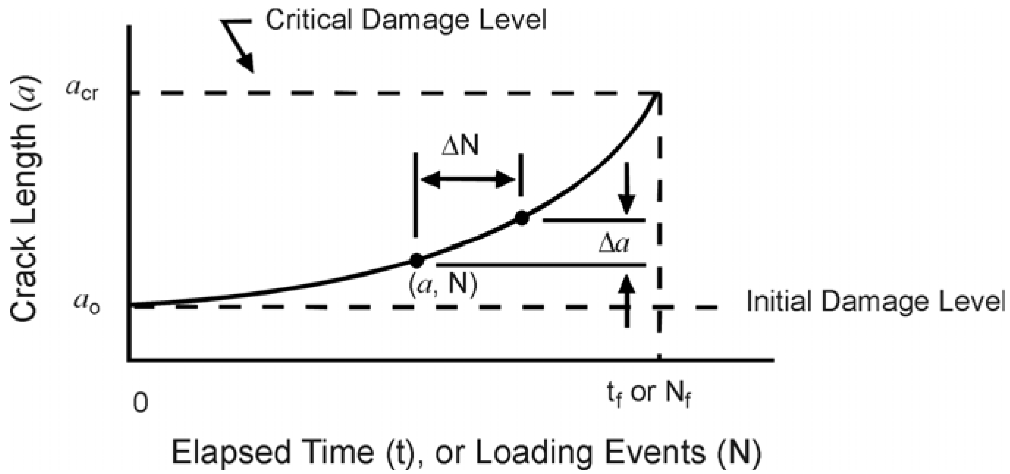

Figure 4: Crack growth behaviour for a typical structural cracking problem

The crack growth is due to cyclic loading of the structure. A crack grows by *da* in a given number of loading events *dN*. At the critical crack size a_{cr}, the crack growth becomes unstable causing failure of the structure. t_f or N_f is the structural life limit of the structure, the time it takes for the crack to grow from (a_0) to (a_{cr}). While this growth from a_0 to a_c may require a large number of cycles, the time to failure once the critical crack size is reached can be near instantaneous [10].

Damage tolerant design allows for structures to have sub-critical damage without immediately being retired from service by establishing an allowable flaw size. Traditionally the allowable flaw size is defined by dividing the critical size by an appropriate safety factor. *The service life of the component can then be determined by calculating the time needed for the crack to grow to the maximum permissible size.*

Growing cracks can significantly affect the overall strength of a structure. To ensure catastrophic failure is avoided the load carrying capacity of the damaged structure must be analysed. In an undamaged structure calculating the residual strength is straight forward - it is simply the ultimate tensile strength of the material. The introduction of cracks in a structure causes a high stress concentration resulting in reduced residual strength. When the crack reaches the critical size where uncontrollable crack growth occurs, the residual strength of the structure rapidly reduces to zero. The goal of damage tolerant design is therefore to ensure that a minimum residual strength of a structure is maintained. The residual strength of a structure as the crack size is increased over the course of its service life is shown in Figure 5.

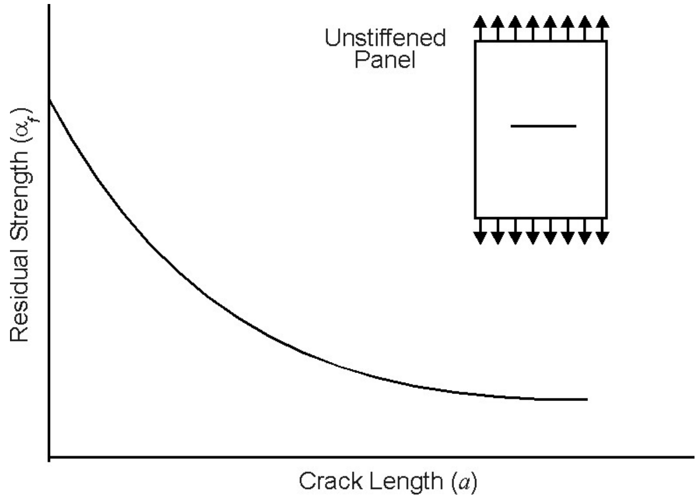

Figure 5: Residual strength diagram for abrupt failure of a single load path structure [10]

To account for this change in residual strength over time it is necessary to determine the crack size as a function of time (Figure 4). The residual strength as a function of time could then be calculated as shown in Figure 6.

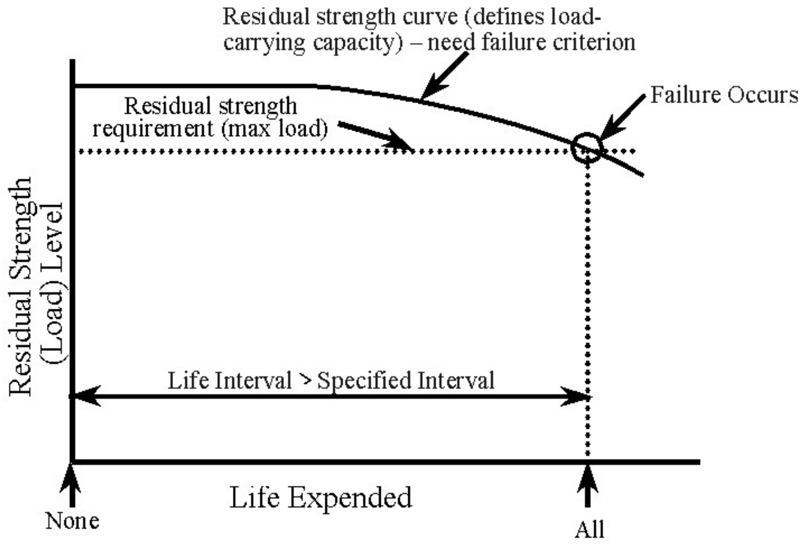

Figure 6: Relationship between the life expended and residual strength capability showing a monotonic decrease in load carrying capacity due to damage [10]

This however is not sufficient. For damage tolerant design a complete understanding of the problem is required. Damage tolerant assessments consider residual strength, damage growth, multiple interactive damage sites, quantitative structural maintenance, and in-service evaluations, in addition to the classification in two damage tolerant design categories: slow crack growth, and fail safe[10].

In a slow crack growth structure initial damage will grow at a stable, slow rate in the service environment and not achieve a size large enough to achieve rapid unstable propagation [10]. Damage tolerance is assured by acceptable slow crack growth rate, sufficient residual strength capacity, and the safe detection of subcritical damage below the critical size for unstable crack growth within the designed life time of the structure. Figure 4 to Figure 6 represent a slow crack growth structure and Figure 7 shows the residual strength and inspection criteria for a slow crack growth structure.

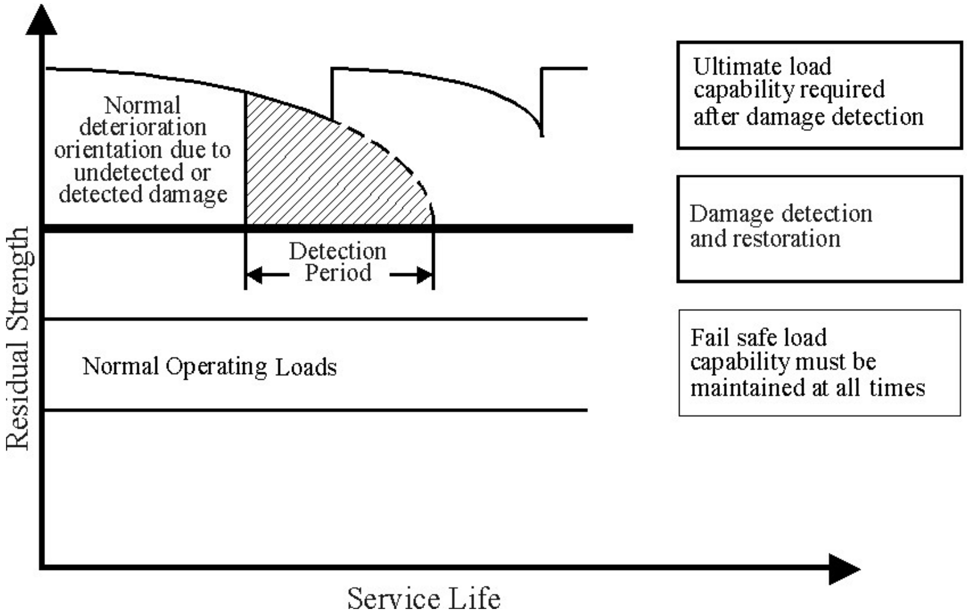

Figure 7: Strength criteria for periodically inspected damage tolerant structure[10]

The simulated or estimated residual strength is corrected after an inspection if the assumed crack length at the time of inspection has been found to be inaccurate. The residual strength of the structure is set equal to a structure with the minimum detectable crack size in cases where no defect is detected.

3.4.4 Inspection and Fracture Control

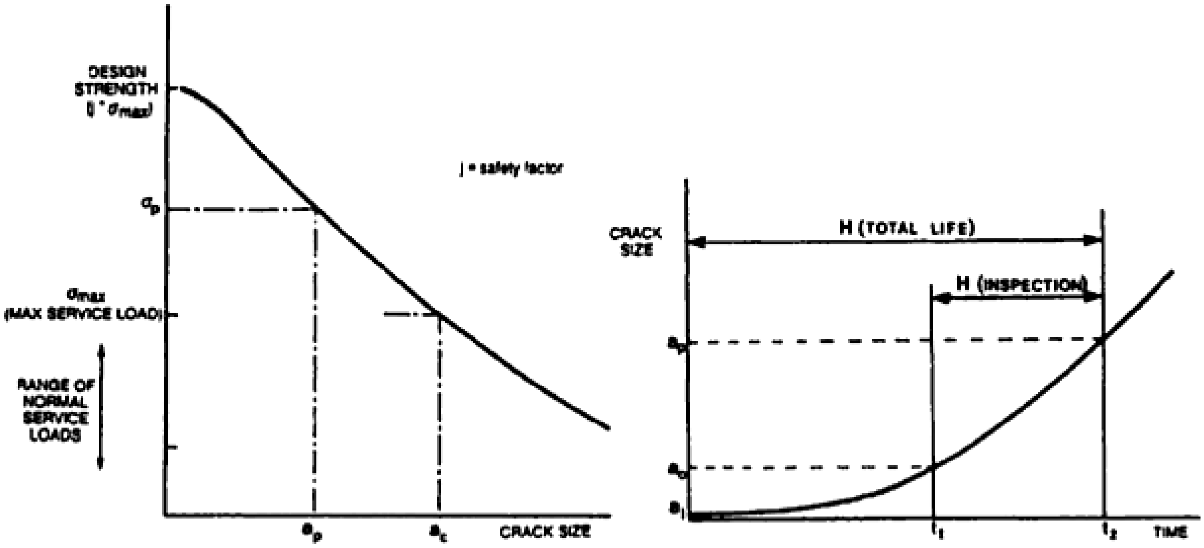

Figure 8: Time available for fracture control: (a) residual strength diagram providing the permissible crack size a_p ; and (b) crack growth curve providing the total life for achieving a_p (*H*) [9]

Using fracture mechanics concepts the residual strength can be calculated as a function of crack size. However conditions (generally official rules, regulations, or requirements) must be set to insure safety of the structure. Referring to Figure 8 the minimum residual strength required (σ_{max}) determines the critical crack size (a_C). Applying an appropriate safety factor the permissible residual strength (σ_p) is calculated and the corresponding maximum permissible crack size (a_p) is determined. Using the appropriate crack growth curve the essential information, total life for achieving a crack with the size a_p (*H*), of the structure is determined. As no crack is allowed to grow past a_p the implementation of a repair and inspection for fracture control is required when a_p is reached [9].

Several options exist for fracture control:

1. Periodic inspection: repair upon crack detection.
2. Fail safe design: repair upon occurrence of a partial failure.
3. Durability design: replacement or retirement after time *H.*
4. Periodic proof testing: repair after failure in proof test.
5. Stripping: periodic removal of crack.

Damage tolerance requirements sometimes prescribe the fracture control procedure. For example military airplanes requirements prescribe methods (1) and (3); commercial airplanes requirements prescribe methods (1) and by intent method (2)[9].

Various inspection methods are available to date. Regardless of the method used, there is a crack size a_0 below which detection becomes difficult. Cracks smaller than this size are assumed to be undetectable. Thus, an effective inspection shall take place within the time interval between a_0 and a_p. Safety can then be maintained by inspecting every half lifetime ($H/2$).

With the introduction of a real-time diagnostic and prognostic system the residual strength can be continuously audited allowing inspection and maintenance procedures to be economically modified while improving safety.

3.5 Critical Component - Turbine Blade

Among the most critical components within a gas turbine are the turbine blades. Operating in an extreme environment the blades are subjected to a variety of damage mechanisms: chattering, high cycle fatigue (HCF), low cycle fatigue (LCF), thermal fatigue, creep, corrosion, and foreign object damage (FOD). Failure typically occurs as a result of a complex interaction between these modes. Cumulative damage effects lead to crack initiation and propagation to a critical failure size. To ensure a high level of reliability, maintenance and inspection are scheduled to detect or replace a damaged blade while the damage is at its incipient stage. Turbine blades are among the most commonly rejected or replaced components [12].

3.5.1 Damage Accumulation in Turbine Blades

3.5.1.1 Foreign Object Damage (FOD)

FOD within gas turbines is largely contained within the cold section (ahead of the combustor, Figure 1) and thus largely limited to the compressor blades. Impact with larger ingested objects can cause necking and bending of the blades. These defects disrupt the airflow around the blade causing increased vibration and possible crack initiation sites and thus the eventual fatigue failure of the blade. Sand and other fine particles can also be a problem causing abrasive wear on the blades. FOD is a rare damage mechanism in the rear or "hot" section of the turbine as any object will have been minced and then incinerated before reaching it. However, lost particles from engine components ahead of the hot section, such as a spalling thermal barrier coating (a coating that has become detached from the blade), may cause damage to turbine blades [12].

3.5.1.2 Fatigue

While many damage mechanisms affect turbine blades, fatigue is the mechanism that generally propagates initial damage to finale failure. Blades experience both high cycle fatigue (HCF) from high frequency engine vibrations and low cycle fatigue (LCF) from the extreme cold and hot phases. Crack propagation (damage accumulation) can be produced from a complex interaction of LCF and HCF [13].

Due to careful and conservative design HCF failures are relatively rare in gas turbines unless some form of substantial initial damage is sustained from other sources[12]. Typically the designed HCF fatigue life of a turbine blade is well in excess of the low cycle fatigue or creep lifetime. However if initiating damage is sustained, from the aforementioned FOD or manufacturing defects, the cycles to failure can be near instantaneous due the quick accumulation of stress cycles caused by the high rotation speed.

LCF however is one of the main reasons for cycle limitation on component life and is due to large differences in loading states experienced by the blade during operation [12]. When stopped the engine disks and blades are at rest and subjected to only a static load at room temperature. During standard flight the blades and disk are subjected to a large, although fairly constant loading from centrifugal forces and still operate at an elevated temperature. During takeoff the same components are subjected to even higher loads at operating temperatures near the material limit. The rate of change between these states is rapid thus causing high levels of thermal stress on both the take-off and cool-down phases. Additional thermal stresses are created due to the blades heating faster than the disk and surrounding shroud. Typically the frequency of these cycles dictates the actual lifetime of the components [14]. Thus an aircraft with an operational profile of numerous short flights will have to retire its components before an aircraft with a few long flights, despite a large difference in actual in-flight hours.

3.5.1.3 Corrosion and Oxidation

Turbine blades can be exposed to aggressively corrosive conditions created from combustion products and at high temperatures elements like sulphur, vanadium, or even lead and bromine, are strong oxidising agents [15]. The majority of turbine blades are protected with thermal barrier coatings which also provide protection from corrosion. Attack is inevitable if the blade is operating in a sufficiently hot contaminated environment and can often lead to, or assists crack initiation and growth [16].

3.5.1.4 Thermal Barrier Coating Failure

Most modern turbines operate at extremely high temperatures. Even with advancements in high temperature super alloys the use of a thermal barrier coating (TBC) is required. TBC's lower the effective operating temperature experienced by the structural (substrate) alloy of the turbine blade allowing the turbine to operate at higher combustion temperature.

Coating technology has been used for decades to protect materials from environmental effects improving the durability of engineering materials or even improving their properties. Thermal Barrier Coatings are suitable to operate in the most demanding of high temperature environments, and are often used in gas turbine applications to insulate turbine and combustor components from the hot gas stream. The extremely high turbine operating temperatures and the reliance on TBC's unfortunately have effectively made turbine blades less predictable as once the TBC has been sufficiently damaged the effective component temperature increases significantly. This temperature increase can cause failure of the component within relatively few operational cycles [17].

TBCs are composed of a relatively complex structure typically consisting of four layers: 1) the substrate; 2) the bond coat; 3) the thermally grown oxide (TGO); 4) and the ceramic top coat (See Figure 9).

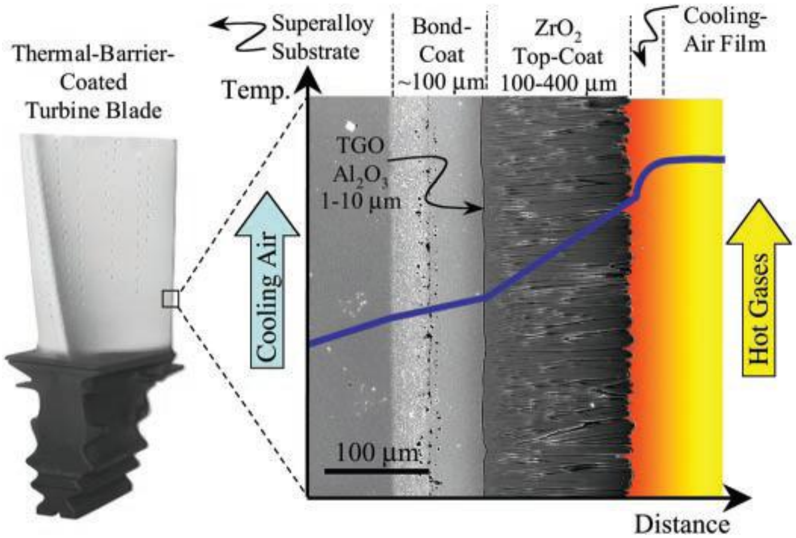

Figure 9: Anatomy and temperature reduction of a thermal barrier coating [18]

Internal cooling and the application of TBC's have allowed major reductions in effective operating temperatures (100° C to 300° C) of the turbine blade substrate alloys. This reduction has allowed modern gas engines to operate at increased thermodynamic efficiency and correspondingly higher gas temperatures, sometimes above the melting temperature of substrate! Even for lower gas temperatures TBCs help to further reduce the operating temperature of the component making them more durable [18, 19].

The growing number of TBC applications and advances in coating techniques has lead to increased reliance on TBCs. Thus their *premature failure during service resulting in the exposure of the bare substrate to dangerously hot gases is of great concern.* The causes of TBC coating failure are varied and interact with each other; the most important ones are:

- Difference in thermal stresses caused by differences in thermal expansion of coating and substrate.
- The oxidation of the substrate.
- The continuously changing compositions, microstructures, interfacial morphologies, and properties of the TBC system.
- Growth of the thermally grown oxide (TGO) between bond and top coat.

The mechanism causing TBC damage is a complex interplay between diffusion, oxidation, phase transformations, elastic deformation, plastic deformation, creep deformation, thermal expansion, thermal conduction, radiation, fracture, fatigue, and sintering. The concern of premature failure and the lack of comprehensive understanding of the TBC system has slowed, or caused over conservative use of TBC, the full potential of which is yet to be achieved [12].

3.5.1.5 Structure of a Thermal Barrier Coating

The Substrate is the structural material of the blade and is typically comprised of a nickel or cobalt based superalloy. In modern gas turbines the substrate material is often air cooled from the inside through internal hollow channels. This establishes a thermal gradient across the component wall. At high temperatures the diffusion of elements can occur between the layers. This interdiffusion is known to have a strong effect on the spallation life of the TBC. Some TBC systems currently still in development introduce a fifth anti-diffusion layer to mitigate this issue [19].

The bond coat is an oxidation resistant metallic layer, 75-100 µm thick and typically composed of NiCrAlY or NiCoCrAlY alloys. It is typically applied using air-plasma spray (APS) or electron-beam physical vapour deposition (EB-PVD) [18]. The bond coat prevents oxidation of the substrate while providing a good bonding surface for the ceramic top coat. During operation the bond coat experiences high temperatures and is exposed to combustion gases due to the porosity of the top coat. Inevitably this results in oxidation of the bond coat creating a TGO layer between top and bond coat (1-10µm thick). The bond coat is engineered to promote a slow uniform growth of this layer as stable alumina (Al_20_3). The rate of this formation is primarily dependent on the inward diffusion of 0_2 but in some cases can be dependent on the outward diffusion of Al [20]. This slow uniform oxide growth mitigates the development of internal stresses and also acts as a diffusion barrier for oxygen, further slowing TGO growth. The composition of the bond coat is also further designed to promote the formation of a TGO with strong adhesion to both bond and top coat [18].

The ceramic top coat provides the functional thermal insulation and is typically made of Y_2O_3 stabilised ZrO2 (YSZ). YSZ has numerous desirable properties including a high thermal expansion coefficient, high elastic modulus, low density, high hardness, high melting point, and most importantly one of the lowest thermal conductivities of all ceramics [18]. The coating properties are strongly related to the microstructure created by the deposition techniques [18].

Air Plasma Spray (APS) deposition usually creates a top coat layer 300 µm to 600 µm thick depending on application. APS deposition creates a flat grained morphology with layers of flat, large diameter (1-5 micron thick, 200 to 400 micron diameter) grains. The resulting grain boundaries and porous cracks are aligned parallel to the metal-ceramic interface. Maintaining a porosity of 15-25% by volume further reduces the thermal conductivity and creates a low elastic modulus, mitigating the strain differential between layers. The interface between the top and bond coat undulates necessarily to increase interlocking adhesion. These undulations also have a detrimental effect, creating out-of plane stresses that cause in service failures of the TBC. APS applied coatings are cheaper than PVD coatings but typically have shorter thermo-cycling lives due to the large number of defects parallel to the interface and the relatively strong out-of-plane interfacial stresses (see Figure 10) [18, 21].

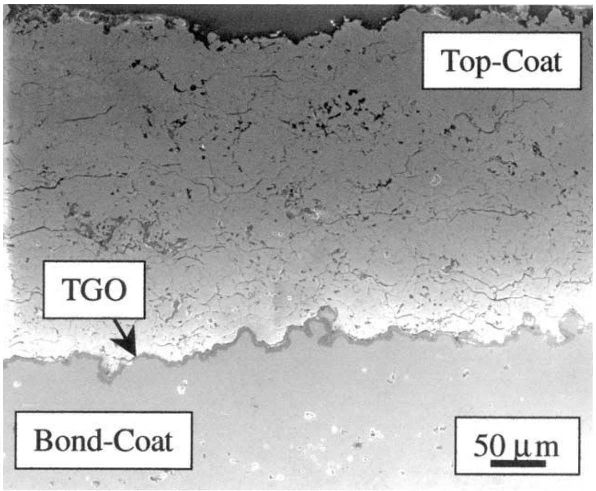

Figure 10: Cross-sectional SEM micrograph showing the microstructure and distinct layer in the APS TBC. TGO has developed after thermal cycling [18]

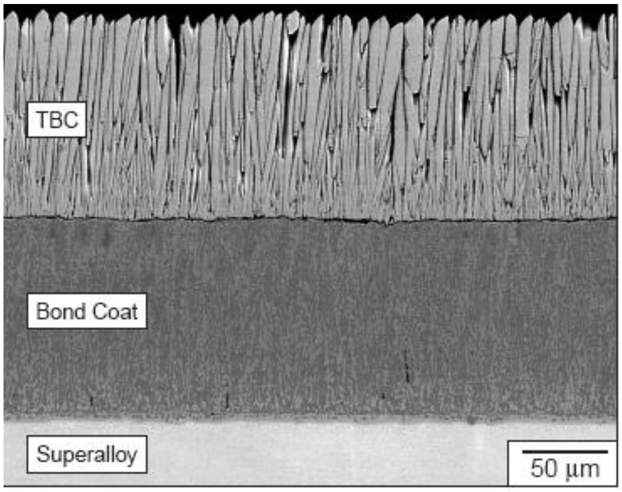

Figure 11: Cross-section SEM micrograph showing the microstructure and distinct layers in the EB-PVD TBC [22]

Electron-beam physical vapour deposition (EB-PVD) TBCs in contrast can be applied to a smooth surface and have a typical thickness of 125 µm. EB-PVD also forms a more complex microstructure. Starting near the bond coat interface a thin region of polycrystalline YSZ with small (0.5 to 1 µm) equiaxed grain structure exists. Growing from this structure is a disconnected columnar YSZ structure (2-10 µm in diameter). Individual columnar grains contain nano-scale porosity and are separated from each other by channels perpendicular to the bond coat interface. The disconnected structure allows separation between the grains to occur at high temperatures. This effectively increases the coefficient of thermal expansion and mitigates mismatch thermal stress. The channels and porosity also help reduce thermal conductivity (1.5 to 2 W/mK) although not to the extent of APS as the EB-PVD channels are parallel to the heat flow (see Figure 11). More durable and expensive than their APS counterparts, EB-PVD TBCs are often used for severe applications such as turbine blade protection in aircraft engines.

3.5.1.6 Thermal Barrier Coating Failure

The ultimate failure of a thermal barrier coating results in the spallation of the top coat. This failure is largely cycle dependent. This is likely because the primary driving mechanism of TBC failure is the growth of TGO which is a cycle dependent process [18, 23]. However due to the large variety in TBC operating conditions, the damage mechanisms are complex and are still not completely understood. The formation of TGO in a constrained volume creates a compressive stress that persists at all temperatures (0.5-1 GPa) [24, 25]. The TGO also has poor thermal expansion properties leading to even larger thermal compressive stresses created from mismatch expansion between the bond coat and the TGO. The peak stress is reached at ambient temperatures, after the engine has been allowed to cool. The strain energy varies linearly with thickness and quadratically with the TGO stress driving the fracture [18].

The formation of TGO predominantly composed of alpha-Al_2O_3 depletes the bond coat of Al and results in the formation of other oxides such as Ni or Co containing spinels of $Y_3Al_5O_{12}$, and Y_2O_3 [22]. The formation of these oxides disrupts the uniform composition of the TGO and creates fast oxygen diffusion paths accelerating localised oxidation.

During extensive thermal cycling the interface between the bond coat, the TGO and the top coat progressively roughens, a process referred to as "ratcheting". Ratcheting causes the imperfections already present in the bond coat to worsen. This causes the undulations present in the case of APS TBC’s to accentuate more and in the case of EB-PVD TBCs the roughening results in the TGO penetrating the bond coat [24, 26]. The net result in both cases is the increase or creation of out of plane stresses normal to the metal/ceramic interface, the severity of which increases with further cycling [18].

Damage initiation occurs in the form of micro-cracks. The cracks then propagate and coalesce resulting in large scale spallation failure [23]. The exact mechanisms are dependent on the individual TBC system. The failure mechanisms are also different for APS and EB-PVD TBC's.

In an APS TBC with an undulating top coat/TGO interface, the stresses are tensile at the crests of the undulation and compressive at the troughs. As the TGO thickens the tensile stresses increase causing cracking between the TGO and the bond coat (I in Figure 12) [27]. The mismatch in thermal expansion between the TGO, top coat, and bond coat also causes compressive stresses at the troughs and tensile stresses at the peaks. This tensile stress results in cracking at the TGO/top coat interface or in the brittle top coat itself near the peak. The tension causes cracks between the top coat and the TGO interface and within the brittle top coat itself (II and III in Figure 12). Beyond a certain TGO thickness the thermal expansion coefficient of the bond coat/TGO composite becomes lower than that of the top coat and the bond coat reverses the stresses at the troughs from compression to tension. This reversal causes cracking within the top coat in the trough of the undulation (IV in Figure 12) [18, 24].

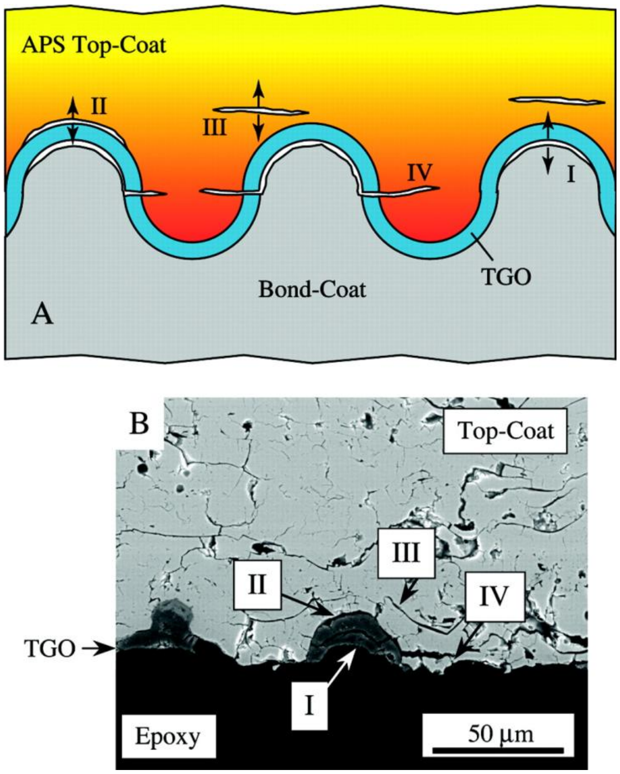

Figure 12: Damage mechanisms in APS TBC [18]

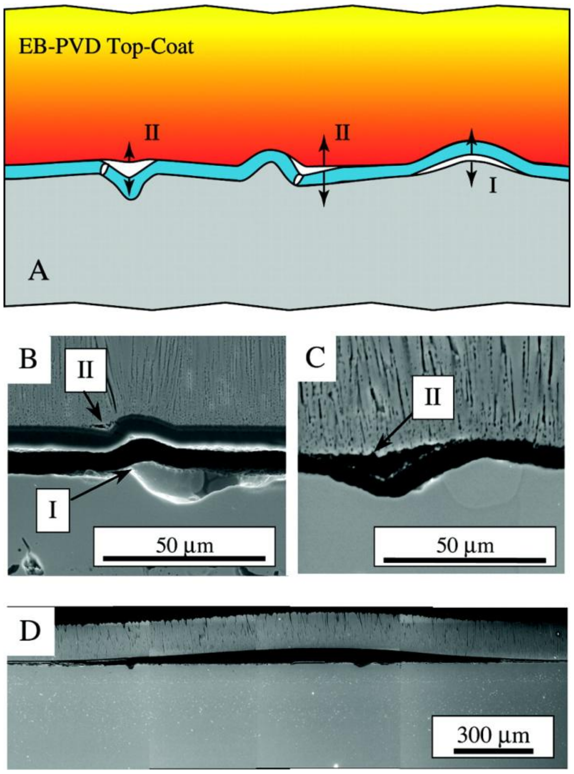

Figure 13: Damage mechanisms in a EB-PVD TBC [18]

Separation of the bond coat from the TGO interface in EB-PVD is similar to that of the APS coatings. However it occurs at ridges, imperfections left on the bond coat before top coat deposition (I in Figure 13). The 2nd crack initiation mechanism is caused by the separation of the TGO/top-coat interface and penetration of the TGO into the bond coat resulting from either progressive TGO roughening caused by cyclic creep of the bond coat, accelerated growth of oxides within the bond coat due to TGO cracking, or cavity formation within the bond coat (II in Figure 13). In an EB-PVD TBC's with relatively large flat surfaces the compression in the TGO causes large scale buckling of the top coat (D in Figure 13). Spallation of the top coat can also be accelerated by sintering at operating temperatures which result in the healing of the channels between the columnar grains. This causes a corresponding drop in the "strain tolerance" of the top coat and an increase in the thermal conductivity, making the top coat more susceptible to cracking and causing a higher surface temperature of the metal surface with an increase in bond coat oxidation and creep [18].

3.6 Sensors

Sensors are the critical technology necessary to enable the design and function of real time diagnostic and prognostic health management systems. Today's aircraft propulsion systems are already equipped with a suite of control sensors, the outputs of which are used as inputs for engine control logic. In addition engines are typically equipped with various sensors measuring many different parameters for health monitoring purposes including pressure and flow sensors for lubrication and fuel systems, accelerometers to detect lower frequency vibrations, and gas path instrumentation to monitor performance [28].

Current research efforts are making critical advances in sensing technology increasing accuracy, reliability, and robustness while decreasing size and cost. These and future advancements have enabled the measurement of previously un-measurable parameters for assessing the health of the propulsion system [28].

Sensors designed to monitor blades within a gas turbine would provide the ability to measure blade tip clearance and blade time arrival. These two parameters are directly related to the elongation and the deflection of the operating blade, as shown in Figure 14. This in turn could allow the detection of faults such as blade erosion, rubbing, cracking, high-cycle fatigue, and foreign object damage.

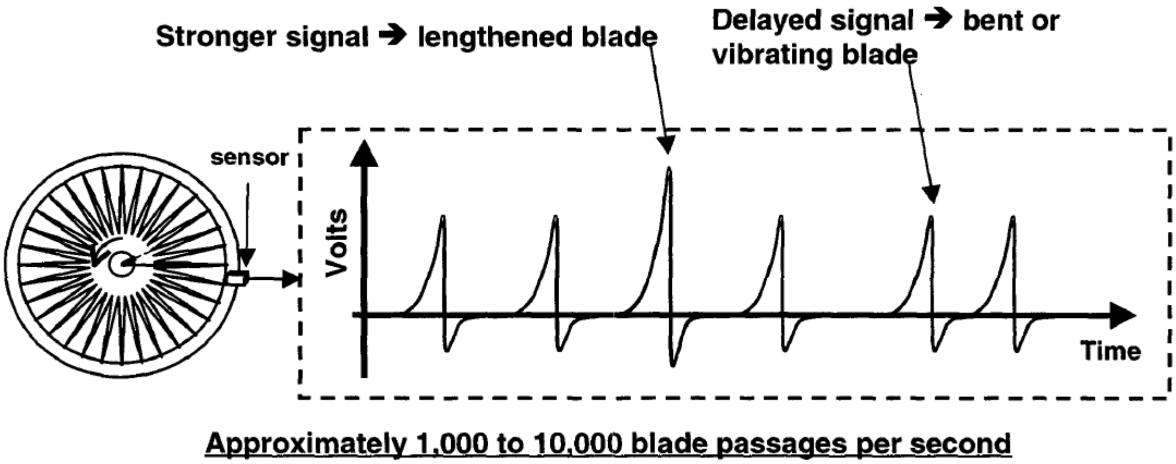

Figure 14: A typical blade tip sensor allows measurement of clearance and time of arrival of each blade [29]

Non-contact sensors are favoured for the monitoring of turbine blade parameters to avoid interference with aerodynamic and structural performance and thus mounting the sensor within the case over the blade is the logical choice. An analysis requirement for sensors capable of monitoring turbine blade performance yields the following general requirements.

- Standoff distance of 50-300 mils (1.27-7.62 mm).
- A resolution of 2 mils (0.0508 mm) for the circumferential position (tip arrival) and 1-5 mils (0.0254-0.127 mm) for clearance (blade elongation).
- Bandwidth of 100-500 kHz depending on blade tip speed.
- Operation within high compressor stages and within the turbine stages will demand a high temperature capability 1500-2500 F (815°C– 1370°C).
- The vibration is often severe up to 300 g peaks [30].

3.6.1 Types of Sensors

Many candidate non-contact sensor systems exist making use of a wide variety of technologies from embedded magnets in turbine tips to microwaves. Three main technologies have shown the most promise:

3.6.1.1 Eddy current sensors

The primary technology developed to date is a magnetic sensor relying for its operation on high-frequency eddy currents actively induced in passing fan or turbine blades. The passing of a blade in front of a sensor results in a magnetic field disturbance which is sensed, processed, and analysed to obtain blade status information. The resulting wave form is similar to Figure 14. A zero crossing corresponds to the instant the blade is centered under the sensor, providing a reference suitable for establishing the blade position. The amplitude of the negative and positive peaks corresponds to the distance from the blade to the sensor. Increasing amplitudes indicate the tip is growing closer to the sensor.

Engine tests on fan blades have shown that eddy current sensors are capable of detecting blade deflections as small as 0.254 mm [29] and a clearance resolution of 0.0254 mm [30] at a 500 kHz bandwidth. While these initial test are not conducted within the turbine stage, the results fulfill many of the established needs.

3.6.1.2 Capacitance Sensors

Capacitance sensors measure the capacitance between any two conductive surfaces within some reasonable proximity. A change in distance between the two surfaces leads to a change in capacitance which is related to the distance from the target [31].

Typical capacitance sensors have relatively poor spatial resolution, short measurement range, and need calibration. But they remain popular due to their low cost and durability [32, 33]. With improvements however, the tip clearance resolution has been improved to approximately 0.05 mm and blade arrival can be resolved with 0.5 µs difference in arrival time. At a blade speed of 350 m/s this equates to a resolution of 0.175 mm. This system would be capable of high resolution, real-time, individual blade measurements of vibration, radial vibration, blade tip clearance, and detection of fatigue cracking [32].

3.6.1.3 Optical sensors

In general optical sensors can obtain the best resolution using triangulation methods and also have the highest system bandwidth. However, compared to other sensors, they are often bulky, expensive, alignment sensitive, and are prone to contamination [33].

3.6.2 Sensing the Onset of TBC Failure

The increasing formation of TGO and the ensuing thermal stresses can cause the TBC to fail leading to thermal property changes that can be detected by thermographic imaging [34]. Thermography could be a good blade health monitoring alternative if it can be demonstrated to be consistently robust and cheap thermocouples could be embedded in the blade at the time of TBC application [35]. Real-time monitoring systems based on thermographic imaging are being studied and are only available as prototypes for now [17].

3.7 Damage Indicators /Measurable Parameters

3.7.1 Deflection

A turbine blade can be simply modeled as a cantilevered beam with distributed load (*q)* and its defection δ is given by:

$$\delta = \frac{qL^4}{8EI} \quad [36]$$

L is the length or span of the blade, *E* is the elastic modulus, and *I* is the blades moment of inertia.

As the blade is damaged through crack growth a section loss occurs reducing the effective moment of inertia of the blade. Also, stress concentration occurs at the crack tip as described in Section *3.4* (*Fracture Mechanics and Damage Tolerant Design*). Both these factors contribute to an increased deflection. Increased operating temperatures reduce the elastic modulus of the blade and thus increase the deflection. The deflection results from a combination of centrifugal and gas bending forces and varies with the rotation speed.

3.7.2 Vibrations

Vibration characteristics of a component have proven to be a good overall metric for measuring the health of a component [29, 37-48]. Damage in the form of a crack changes effective stiffness and energy dissipation properties of the blade. This in turn changes the measurable dynamic response of the system leading to a lower natural frequency of vibration and to an increase in the displacement amplitude of the blade [45].

This can be illustrated by simplifying an undamaged blade as a cantilevered beam of stiffness *k*:

$$k = \frac{Ewh^3}{4L^3} \quad [49]$$

E is the elastic modulus of the beam material, *w* is the width of the blade, *h* is the thickness and *L* is the length. The undamped natural frequency ω_n of a linear system is [49]:

$$\omega_n = \sqrt{k/m}$$

m is the mass of the system. Thus, as the blades effective stiffness decreases as a whole or locally due to the introduction of cracks the natural frequency lowers correspondingly [44, 50].

The vibration of the blade alone, particularly resonance vibration, can often lead to blade failure through fatigue and thus must be monitored accurately in order to calculate and predict changes in the loading conditions and assess the remaining fatigue life of the blades [51].

3.7.3 Temperature

The temperature of the blade would increase notably after TBC spallation. The localised heating created by TBC spallation would certainly be visible using thermo graphic or infrared photographic techniques[17], or could be detected using embedded thermocouples[35] However, these technologies have limitations as discussed in section 3.6 *(Sensors)*. The higher temperature experienced by the substrate material in the absence of a TBC would affect material properties such as elastic modulus (E) and yield strength (σ_{ys}). Modern superalloys are able to maintain structural strength up to incredibly high temperatures [52] above which material properties rapidly degrade [53]. Change in E or σ_{ys} may contribute to or cause a detectable change in deflection or vibration.

3.7.4 Blade Elongation

The blade elongation is already used as a metric for monitoring creep damage. Blades with accumulated creep damage elongate to the point where they “rub” [54] against the casing or strip designed for such contact. Measuring blade elongation through tip clearance can indicate accumulated early stage creep damage [29, 30].

3.8 Introduction to FEA

The finite element method (FEM) is a numerical technique for finding approximate solutions to partial differential and integral equations. FEM or more commonly FEA (finite element analysis) is particularly useful when applied to complicated, moving, or changing domains where analytic solutions are either impossible to achieve or lack accuracy. While initially developed for solid structural analysis, FEM has since been applied to many other applications including heat transfer, fluid, and electromagnetic applications.

Essentially physical problems, for example, a structure subjected to a certain load is reduced to a mathematical model and then solved. This mathematical model is generated through discretization whereby the domain of the problem is divided into smaller but finite sub-domains, called elements. The individual elements are connected through nodes which have individual degrees of freedom. Reducing the geometric domain of a problem into elements is commonly referred to as meshing. By providing elastic material data, the local elastic behaviour of each element can be defined in matrix form in terms of loading, displacement, and stiffness. The individual elements are bound together through their common nodes forming a global matrix to which global boundary conditions and loads can be applied, typically through the underlining geometry. With a global stiffness matrix and with loading and boundary conditions defined, the nodal displacements of the model can be calculated. From these displacements resulting stress, strains, elastic energy, etc, can be calculated.

3.8.1 Abaqus CAE

Abaqus/CAE is an interactive environment used to create finite element models, submit crafted models as jobs, and evaluate results with the post-processing capabilities of the viewer module[55]. The first step in creating and analysing an FEM model using Abaqus is to create a “model” file. The model file contains the following objects:

- Parts – Geometric data for individual or multiple parts. Parts can be partitioned and different materials and loads can be applied to individual partitions.
- Materials and Sections – The required physical and mechanical material data as well as specific section definitions. For example a material can be defined as a solid homogenous section or as a beam with a defined cross-section.
- Assembly – Where part instances are spatially arranged.
- Sets and Surfaces –Vertices, edges, surfaces, of note defined specifically for selection.

- Steps – Defined sequences which provide a convenient way to changes in the loading and boundary conditions of the model as well as different analysis procedures.
- Loads, boundary conditions, and fields – Step-dependent objects that define the loads, boundary-conditions, or field applied to the model.
- Interaction and their properties – Defines the nature of interactions between different parts.
- Meshes – generated meshes on parts or assemblies with a defined shape, size, element type, and required refinements.

Once the model file has been created it is submitted as a job and written to an input file containing the basic code and algorithms needed to calculate a solution. The input file once processed by Abaqus's standard or explicit solver produces an output data base file which can then be opened and studied in a post processing module [56]. Information from output database files can also be imported or read by CAE and compiled in another input file. This allows data from earlier solutions to be exported and incorporated in new models.

4 Method

Without accurate and specific geometric data and operating conditions loading on the blade can only be theorised. It is important however to have approximately the right magnitude in order to be able to confidently draw conclusions from observed trends. The basic assumptions used for loading are based on previous work analysing the stresses within the Pratt and Whitney PW-100 turbo prop, a commonly used engine for aircraft flying shorter routes (*Appendix I: Reverse Analysis on PW-100 Turboprop)****.*** This should prove to be a good choice from which to base assumptions for several reasons: 1) operational data are relatively available compared to many other engines; 2) the power turbine stage does not require internal cooling thus simplifying the blade geometry for three-dimensional models.

4.1 Centrifugal Loading

To define a centrifugal loading in Abaqus an angular velocity about a defined axis is needed. From [57-59] the maximum propeller shaft rpm for a PW-100 turboprop is given as 1200 rpm and at cruise conditions corresponds to 85% of maximum rpm. The reduction value of the gearbox on PW-100 is taken as 17:1 (*Appendix I: Known Data).* The power turbine rotational speed (ω) can then be calculated as 1815 rad/s. However this is for turbine blades that are clearly designed with a taper which would correspondingly reduce centrifugal loading on the blade by around 2/3 the value for an un-tapered blade [54]. For simplicity it has been decided to model turbine blades with no taper, thus the centrifugal load will be reduced to a *constant 1500 rad/s* for all models.

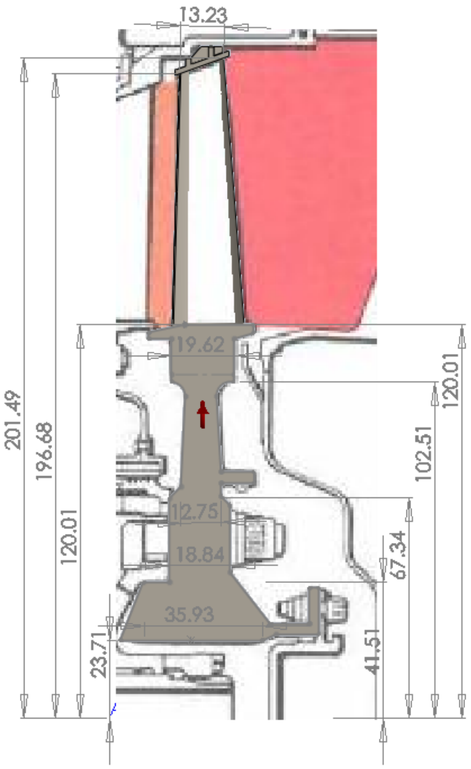

Figure 15: Drafted powers stage from the PW-100 turboprop superimposed on a scaled drawing (all dimensions are in mm)

The modeled blade rotates around an axis set at 0.12 m below the root of the blade. This is approximately the same distance away as the shaft in the PW-100 (see Figure 15). To ensure the centrifugal force does not induce any blade deflection the blade's center of mass is aligned with radial direction of this load which is denoted by a small arrow in Figure 15.

4.2 Pressure Loading

The gas bending force is established by approximating the difference in pressure between the pressure side and suction side of the blade. This is difficult as the pressure distribution is dependent on the blade's profile and little data are available on the pressure distribution across the blade span.

Assuming the pressure distribution is constant across the cord of the blade the pressure differential can be modeled as a distributed load with a value determined by through physical gas bending equations. The angular momentum of the gas changes as it moves across the turbine blade, the force arising from the change produces the usable torque and also produces a bending moment

(M_ϑ) in the rotor axial direction [54]. There is also a moment about the rotors tangential direction (M_a) created by the pressure drop across the turbine stage. The bending moment M_ϑ is by far the greater moment [54] and thus for the purpose of two-dimensional modeling, the moment in the tangential direction can be neglected. The bending moment about the rotor axial direction is given by [60]:

$$M_\theta = \left[\frac{c_m W_s \tan \beta_m}{2nU_m} \right] \quad (0.1)$$

From (*Appendix I: Calculations)* c_m = 21.8 mm is the cord length at mid-span; W_s = 1565 kW is the work done by the turbine stage; β_m = 80° is the change in angular direction; n = 74 is the number of blades in the turbine stage; and U_m = 341 m/s is the blade speed at midspan. Substituting all values in equation 0.1 and solving yields:

$$M_\theta = \left[\frac{21.8 \ mm \quad 1565 \ kW \quad \tan \ 80°}{2 \ 74 \quad 341 \ {}^{m}\!/\!{}_{s}} \right]$$

$$M_\theta = 3.98 \ \mathrm{N \cdot m}$$

Assuming the bending moment M_a is produced by a load distributed evenly along the span of the blade it is simply replicated in two dimensions reducing the model to a symmetric beam bending problem.

The bending moment produced in a cantilevered beam with a pressure load is given as:

$$[61] \; M = \frac{qwL^2}{2} \quad (0.2)$$

q is the force/area of the pressure load and L is the length of the cantilevered beam and w its width. Referring to Figure 15 a width of about 2 cm can be seen although this would depend on the angle of the blade on the hub as well as the blade profile. The cooled two-dimensional model to be constructed first has considerable thickness and height. To maintain proper proportions a width of 4 cm is assumed. Equating M_a to M and substituting in the length of the initial model the pressure load needed to produce the desired bending moment can be calculated.

$$3.98\ \text{N}\cdot\text{m} = \frac{q\ \ 0.04\ \text{m}\quad 0.1\ \text{m}\ ^{2}}{2}$$

$$q = 19900\left[\text{N}/\text{m}^2\right]$$

$$q \approx 19000\left[\text{N}/\text{m}^2\right]$$

This provides a reasonable pressure differentially to simulate gas bending.

4.3 Temperature Loading

The inter-turbine temperature before the power stage is given as approximately 785°C and the exhaust temperature is between 565-600°C. The temperature distribution that would be created on the surface of the blade is required. Gas velocities through the turbine stage vary across the annulus due to friction with the walls and of course different velocities exist around the profile of the turbine blade itself. The temperature distribution around the profile of a turbine blade is of little interest for two-dimensional modeling as the profile is neglected for the purpose of the study. The typical spanwise temperature distribution of a cooled turbine blade only varies slightly with the distance from the root of the blade [54]. This however is likely due, at least partially, to the change in efficiency of the cooling-gasses rising through the blade. The surface temperature distribution for an un-cooled blade is given in great detail in [62]. Visually sampling and recording the temperatures as a function of normalised blade span yields the temperature distribution shown in Figure 16 and shows good agreement with the span-wise temperature distribution given in [63].

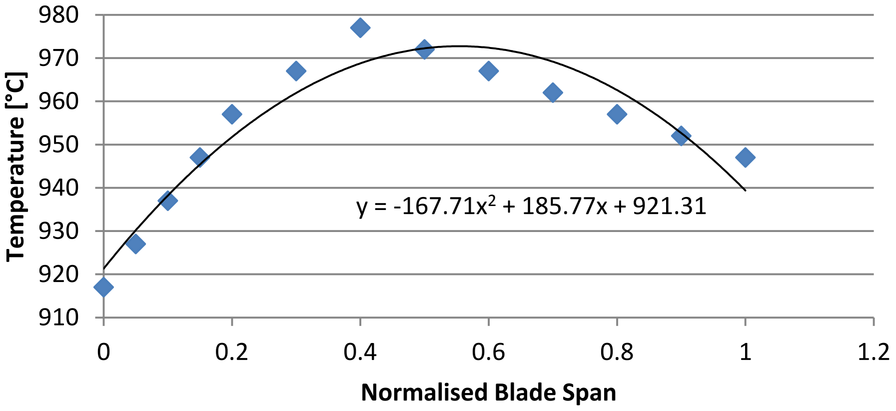

Figure 16: Blade temperature as a function of normalised span

Normalising for blade span, a 2nd order curve can be fitted, the equation for which can be inputted as temperature field within Abaqus. The resulting temperature distribution is applied as a surface temperature boundary condition at various magnitudes. The flexibility is important as models with a variety of sizes may be run and the range of temperatures studied must effectively bracket the temperature at which the modeled material begins to lose structural strength at an average temperature range of 755 K to 1155 K.

4.4 Material Data

4.4.1 Material Properties / Nickel Based Superalloys

The substrate or structural material used for modeling has been chosen as Waspaloy, an age hardening austenitic nickel-based superalloy. Historically, it is used for a large variety of high temperature applications including turbine blades [64-66]. With increasing turbine inlet temperatures, it is now typically used for disk and shroud materials. This material is suitable for modeling for three main reasons:

1. Waspaloy has been used and tested extensively and thus a wealth of mechanical and physical data needed to construct a model is readily available.
2. It exhibits a sudden loss of material strength above the safe operating temperature characteristic of many high-temperature super-alloys.
3. It is readily available and loses material strength at a relatively low temperature (700-800°C) meaning that experimental validation is easier as high-temperature testing is difficult and expensive, increasingly so the higher the temperature.

4.4.1.1 *Physical Properties*

The room temperature density of Waspaloy is 8.20 g/cm^3 [67]. For the sake of simplicity, the density is considered constant for the temperature range covered in this study. As the thermal conductivity is known to increase with temperature, temperature-dependent data are used as shown in Table 1.

Table 1: Extrapolated thermal conductivity [67]

Temp [C]	Temp [K]	*k* [W/m-K]
200	473	12.6
400	673	15.7
600	873	19.1
700	973	20.9
800	1073	22.7
900	1173	24.5

4.4.1.2 *Mechanical Properties*

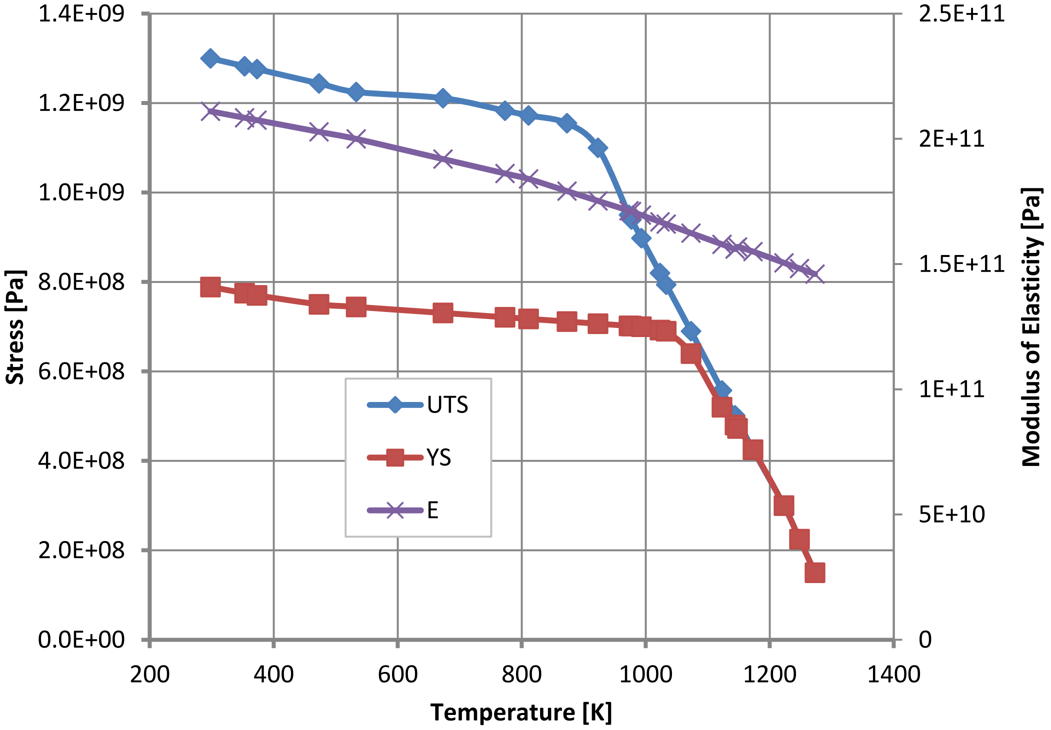

Figure 17: Mechanical properties of Waspaloy [65, 67, 68]

Waspaloy exhibits a linear lowering in elastic modulus with an increase of temperature which is likely to affect vibrational response and elastic deformation. Referring to Figure 17, the sudden loss of material strength is evident as both the yield strength and ultimate tensile strength of the material decrease rapidly at approximately 900 K. The Poisson's ratio has been taken as a constant 0.3 [66, 69]. The strain at fracture also varies with temperature and is summarised in Figure 18. Data are obtained by sampling points from a figure in [67, 68].

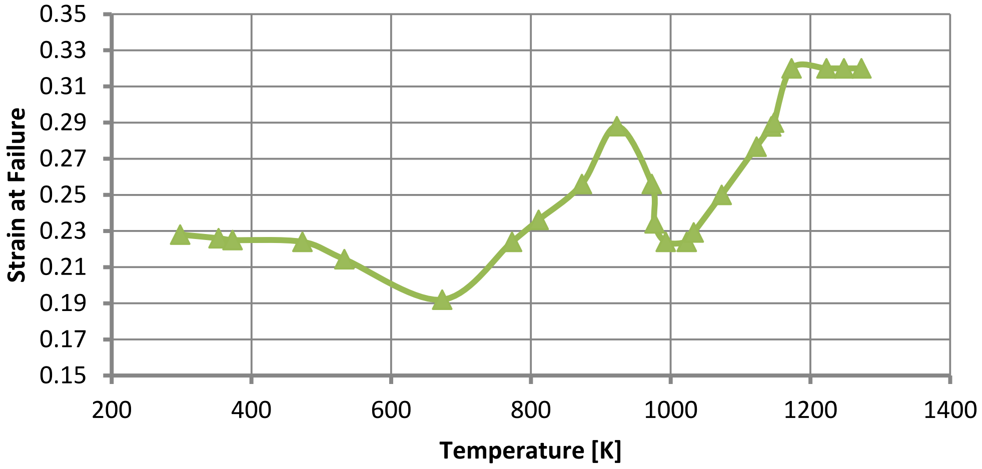

Figure 18: Elongation at failure for Waspaloy

Using the data from Figure 17 and Figure 18 temperature dependent stress-strain data can be approximated in Figure 19.

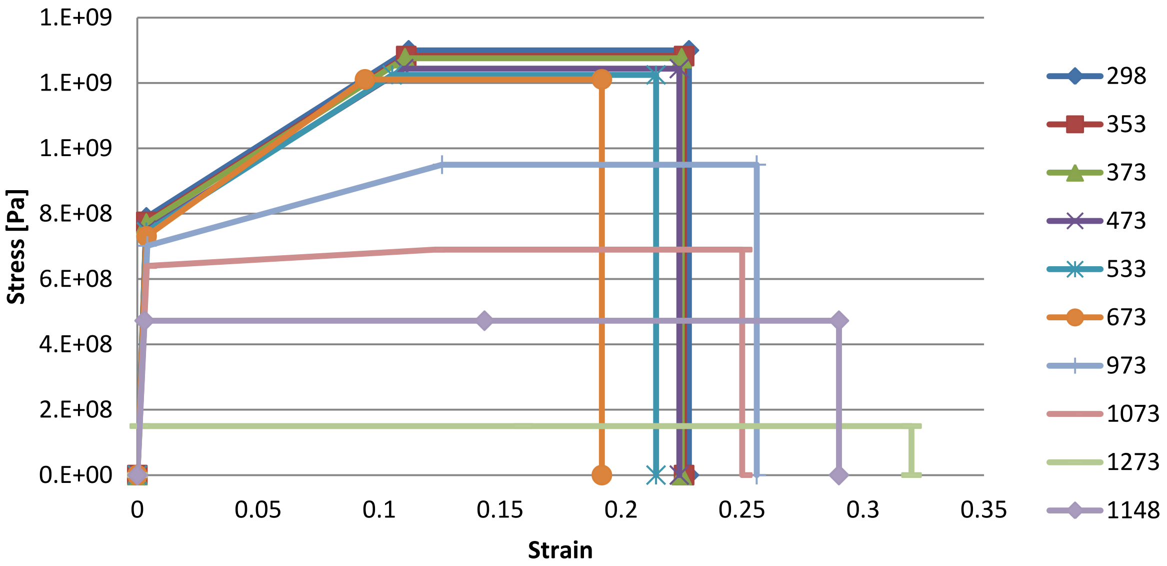

Figure 19: Approximated stress vs strain data at different temperatures [K]

The elastic region in Figure 19 was constructed by plotting the elastic behaviour to yield from the known elastic modulus data. The Ultimate Tensile Strength (UTS) is assumed to be reached midway between the yield-strain and the strain at failure. The UTS is then used until the strain at failure is reached after which the strength of the material is assumed to have vanished. This creates a crude failure criterion within the model elements. The elements that reach the failure strain no longer support any load.

4.4.2 Thermal Barrier Coating

For the purpose of this study, the investigation of the thermal barrier coating was limited to the assumption of perfectly coated and uncoated blades, as well as coated blades with local coating defects. For simplicity, the relatively thin thermally grown oxide (TGO) is neglected as well as the bond coat as it has similar physical properties to the substrate and is so thin that its effects are negligible. Thus only the Y_2O_3-stabilized ZrO_2 (YSZ) is considered

Section *3.5.1.5 (Structure of a Thermal Barrier Coating)* gives general properties for the ceramic top coat. The thermal conductivity (*k*) for a fully dense Y_2O_3-stabilized ZrO_2 (YSZ) is given as 2.3 W/mK but due to cracks and pores perpendicular to the direction of heat transfer (particularly true in Air Plasma Sprayed TBC's) the effective thermal conductivity is reduced to 0.8-1.7 W/mK. Thus, a value of 1.6 W/mK was chosen for the thermal conductivity of all modeled TBC's. [18] The density of a fully dense (YSZ) is given as 6400 kg/m^3 [18] with an elastic modulus between 10 and 50 GPa [18, 26].

4.5 Two-Dimensional Coated Blade with Cooling

While most turbine blades make use of TBC's or other coating technologies to protect the blade, only blades with some form of internal cooling really benefit from the thermal protection. Blades with no internal cooling would generally rise to their environment temperature under stationary conditions whether or not a thermal barrier coating is present. Thus a cooling heat flux is needed to create a temperature differential from the outside of the blade to the inside. If the blades are subjected to surface temperature conditions of 755 K- 1155 K this would require a heat flux of -$1x10^9$ W/m^{2}K to maintain a reasonable operating temperature for the substrate(*Appendix IV*).

4.5.1 Model Construction

First a heat transfer model is created where the temperature distribution outlined in section *4.3 (Temperature Loading)* is increased by 200 K over three successive steps from 755 K to 1155 K. At each step the temperature of the modeled blade is allowed to reach steady state. This essentially creates three different temperature distributions. This procedure has been used for all models. The resulting nodal temperature distributions are exported to the structural model. The structural models then run a static steady-state analysis step and a linear perturbation frequency extraction step at the three different temperature distributions. The solution to the structural model is then analysed. Meshes must remain identical between heat transfer and structural models to insure accurate transfer of nodal temperature data. From experience, the heat transfer solution is relatively insensitive to mesh size, thus the mesh size optimization and the convergence study were done for the structural models only.

4.6 Experimental Procedure

Across all models similar experimental procedure was followed. First an undamaged model was created and analysed to provide a baseline mechanical response. Next, damage in the form of small TBC defects and circular cracks were introduced and the difference in response to loading conditions studied. While the resulting temperature, stress, and strain distributions are viewed and analysed briefly to ensure the models are solved correctly, only two main parameters are studied as possible indicators of structural health: *Tip Displacement and change in natural frequency.*

The tip displacement refers to the static displacement of the blade tip under load. This can be measured by tracking the nodal-displacement at selected nodes located at the tip of the modeled blade. The nodal displacement is outputted as a magnitude (U), the total absolute distance the node has moved, as well as the vector components (U1=x-direction, U2=y-direction, U3=z-direction). The nodal displacement in the x-direction in the 2-dimensional models or z-direction in three-dimensional models is equivalent to the blade deflection. Displacement in the y-direction is equivalent to the elongation of the blade for all models.

The natural frequency of the model is calculated within Abaqus using its inbuilt Lanczos eigensolver**.** The analysis is limited to the first 6 modes of vibration. The frequencies for the first six modes are written to an output data base file and extracting the frequency is done by simply requesting the output.

To study the effects of damage severity, the size of TBC defects and the depth of crack damage is increased. To study the effect that damage location would have, damage was modeled at multiple locations. Each change in size, depth, or location, requires the generation of two separate models; one heat transfer model; and one structural model. After solutions for the different models are obtained the tip-displacement and natural frequencies are extracted and stored in excel. Direct comparisons can then be made to extract the effect the specific damage has on tracked parameters.

4.7 Two Dimensional Models

4.7.1 Geometry

The blade is approximated as a two-dimensional solid with a height of 10 cm and a thickness of 1 cm. The TBC is modeled as 300 µm thick, which is among the thickest recorded in literature [18]. The TBC is created by partitioning 300 µm thick sections off both sides of the initial 1 cm thickness. The geometry is not selected from any specific turbine blade, however it is suitable for initial investigation into the effects coating and substrate damages can have on a loaded turbine blade with a thermal barrier coating.

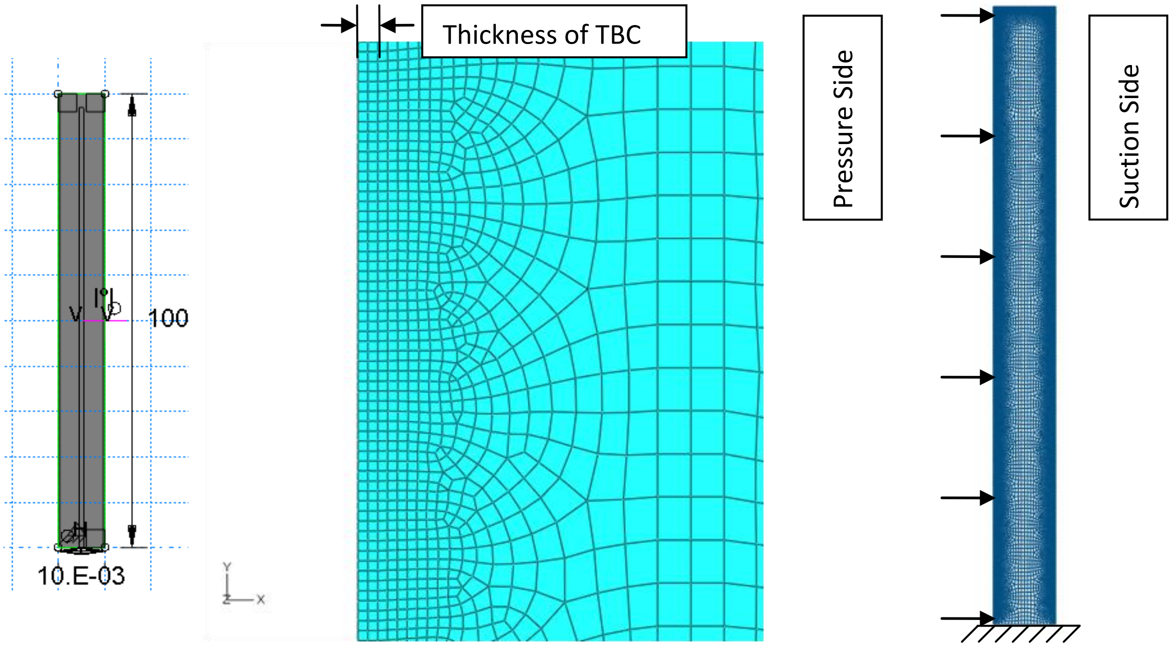

Figure 20: Geometry, mesh, loading and boundary conditions, for the cooled turbine blade model

4.7.2 Meshing

The memory demands for two-dimensional models are relatively low, so a very fine mesh can be used without stressing computer resources. The element size increases from 1.5x10^{-4} m at the surface to 51.5x10^{-4} m at the center. This ensures two elements will be present across the thickness of the thermal coating for accuracy.

The undamaged model contains 19401 nodes forming 18819 elements. 18558 elements are linear quadrilateral elements of type CPE4R for structural analysis and DC2D4 for heat transfer analysis. An additional 261 linear triangular elements are present in the model. CPE elements are bilinear plane strain elements with reduced integration hourglass control. DC2 elements are simple linear heat transfer elements. A structured meshing algorithm was used for both the TBC layer and the blade center where the body heat flux has been applied. A free meshing algorithm was used everywhere else to provide an even transition from the small elements at the surface to large elements at the center.

For the heat transfer analysis, the surface temperature boundary condition was applied to both the pressure side and suction side of the model. The tip and root of the blade are assumed to be insulated q_x = 0 W. The calculated cooling body heat flux of -1x10^9 W/m^3 was applied to the slim (1 mm x 97 mm) rectangular partition seen in Figure 20. The loads described in sections *4.1 (Centrifugal Loading)* and *4.2 (Pressure Loading)* are applied to the model in the first analysis step and propagated through each of the following steps. The distributed load is applied to the pressure side of the blade and the centrifugal load affects the whole geometry of the model. The blade is assumed to be fixed at the root $u_x = 0$ m; $u_y = 0$ m; $u_{rz} = 0$ m.

4.7.3 Modeling a Thermal Barrier Coating Failure or Crack

The steps described above were also taken to model a damaged blade and featured two changes with respect to the undamaged model:

The geometry and the meshing were altered. A coating failure was modeled by simply removing a portion of the geometry denoted as the TBC material. This was typically done by applying a "cut-extrude" feature to a portion of the undamaged model. This allowed different sizes and locations of the TBC defect to be quickly modeled and meshed by simply changing the parameters of this feature. Similarly, steps were taken to introduce a crack with a 3 mm circular tip and varying depth. The element size was reduced around the crack tip and surrounding area to ensure accuracy of the resulting stress concentrations. The mesh and geometry of a 3 mm TBC defect as well as a 3 mm crack are shown in Figure 21. The mesh refinement does increase the element count somewhat, but the modelling duration was still acceptable.

> The tip of the modeled crack does not necessarily resemble the shape or size usually sharp seam cracks found in damaged turbine blades. However, this is not expected to cause extreme errors in expected overall deformation, elongation and deflection of the blade due to the localised effect of crack stress concentration and due to natural blunting of even sharp cracks during plastic deformation of ductile materials. It shall be noted that, in contrast to the overall deformation of the entire blade, cack propagation and fracture mechanism heavily depend on crack geometry and crack tip radius. However, this is in no way the focus of the current study.

At the TBC coating defect or crack, the surface temperature condition is applied directly to the exposed substrate. The distributed load is not applied to the surface of the crack tip as the complex interaction of gas flow is unknown and the area being neglected is small compared to the span of the blade which renders the effect on measurable parameters negligible.

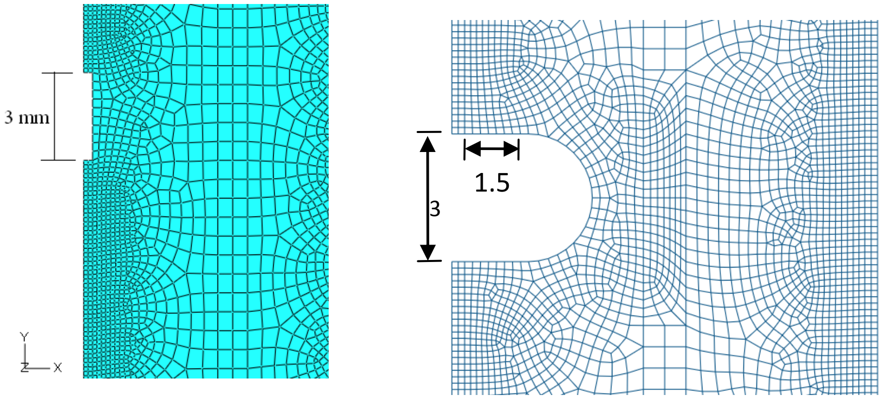

Figure 21 Blade with TBC failure (left) and a circular crack with 3 mm depth (right)

4.7.4 Convergence Study

The sizes of the elements are limited to the size of the partitioned regions. Thus it is not possible to create a TBC element larger than the TBC itself. Nor is it possible to create internal elements larger than the area cooling heat flux is applied. Initially an undamaged model was created with the largest possible element size: 3 µm x 3 µm at the surface of the model and 1 mm x 1 mm at the center. This results in a model with 5771 nodes. Refining the mesh to a node count of 19401 used for the study produces no noticeable increase in processing time. Elements can also be generated with mid-side nodes called quadratic elements. By using the same mesh with quadratic elements, the number of nodes increases from 19401 to 57620, but increases processing time to several minutes. The effect the refined mesh and quadratic mesh have on the solution is summarised in Table 2. It can be seen that changes in the solution are negligible with the exception of the results obtained for the blade deflection. This value is very sensitive because the deflection of an undamaged blade is extremely small (x10^{-7}) thus even the slightest change in the generated stiffness matrix can yield a large percentage change in the result. The error in solution for natural frequency is a negligible 0.03%.

The extremely small deflection values modelled for the undamaged blade remain below 1 micrometer independent of the number of elements/nodes used. This range of change is of no practical use. Therefore, no further efforts were made to further optimise the model, and 18819 nodes with a processing duration of just 2 minutes were preferred over larger node numbers that required calculation times above 2 hours.

Table 2: Convergence study undamaged model

# of nodes	Magnitude of Nodal Displacement [m]	Deflection [m]	Elongation [m]	Frequency at Mode 1 [Hz]	
5771	1.05E-04	7.00E-07	1.05E-04	685.194	
18819	1.05E-04	6.31E-07	1.05E-04	685.885	(used for study)
57620	1.05E-04	6.88E-07	1.05E-04	686.118	
94857	1.05E-04	6.34E-07	1.05E-04	686.116	
283858	1.05E-04	6.34E-07	1.05E-04	686.116	
289341	1.05E-04	6.35E-07	1.05E-04	685.885	

With increasing tip deflection the % difference decreases, thus models with TBC or crack damage are less sensitive to the number of element/nodes as can be seen in Table 3.

Table 3: Convergence study 3 mm cracked model

# of nodes	Magnitude of Nodal Displacement [m]	Deflection [m]	Elongation [m]	Frequency at Mode 1 [Hz]	
21909	3.23E-04	3.00E-04	1.18E-04	669.604	(used for study)
65016	3.25E-04	3.02E-04	1.18E-04	669.796	
92349	3.24E-04	3.01E-04	1.18E-04	669.745	
275627	3.25E-04	3.02E-04	1.18E-04	669.789	

.

4.8 Three-Dimensional Model

4.8.1 Geometry

The geometry for the three-dimensional model follows the inferred geometry of the PW-100 more closely; however it neglects the inclusion of a shroud, taper to the blade, and does not replicate the geometry needed to create a change in gas-path velocity. The profile of the blade was created by loading a stock Sokolov profile in *Airfoil Design Workshop*, a simple program capable of interactively generating, modifying, and exporting a variety of airfoils. The airfoil was modified until it subjectively resembled a generic profile for a turbine blade and then exported to *Solidworks*. Once in *Solidworks,* the profile was scaled to Figure 15 and then extruded to create a three-dimensional blade. To further increase accuracy, the blade was modeled with a simple fir tree design. The complete geometry of the blade can be found in *Appendix I (Reverse Analysis on PW-100 Turboprop)*. The final blade model was approximately 80 mm in height (not including the root), 21 mm wide (leading edge to trailing edge), and 3.2 mm thick at its thickest point.

Circular crack damage was introduced within *Abaqus* with a cut revolve feature. A sketch of the crack to be introduced is created on a plane offset from the primary X-Y plane and has symmetry about a plane offset from the root of the blade. The result is a circular crack for which location and depth can be easily changed by simply varying the values of the plane offsets (see Figure 22).

4.8.2 Meshing

Creating a mesh for a complex three-dimensional geometry is considerably more challenging than two-dimensional models especially when small and complex features, such as a small circular crack, are to be introduced. For this work, the mesh generation for an undamaged blade was done using 120497 nodes and 26908 elements. 25082 elements are hexahedral elements of type C3D20R for structural analysis and DC3D20 for heat transfer analysis. Additional 1826 linear tetra elements were used; C3D15 for structural and DC3D15 for heat transfer modelling. C3D#R denotes a general stress/displacement element with hour-glass control. DC3 denotes general 3D heat transfer/mass diffusion elements.

The meshing of models with cracks is considerably more complicated. The circular path the crack makes with the curved surface of the blade creates some very complex geometry requiring heavy partitioning and fine mesh control. The fine mesh desired at the crack tip is not easily refined to a coarser mesh at other locations leading to a higher element count for the entire model. A balance is sought between accuracy, computing resources, and time. This was done by initially starting with fine a mesh that proved unusable due to limited computer resources. The element size was then gradually reduced until a memory demands were sufficiently low that a solution could be calculated.

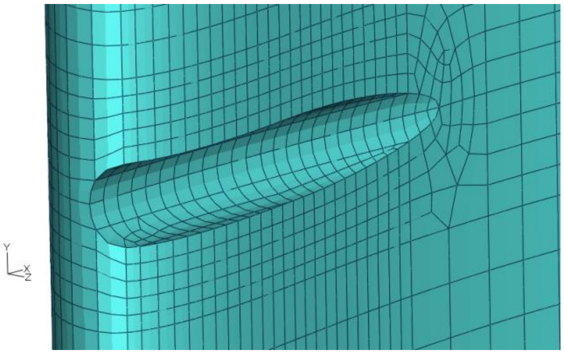

Figure 22: Meshing of a circular crack with a depth of 0.9 mm (measured at greatest depth)

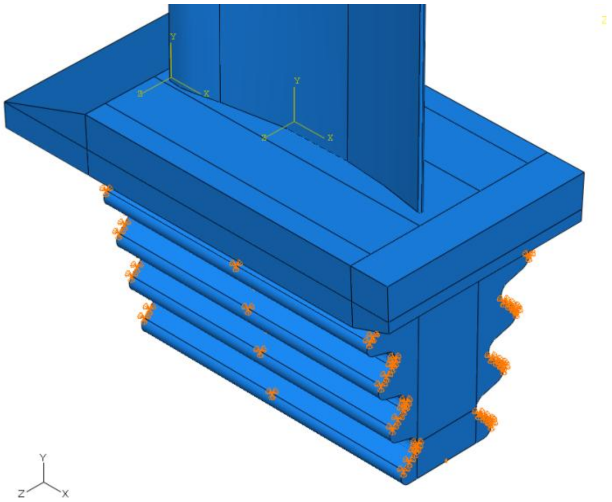

Figure 23: Fixed condition on blade root

4.8.3 Loading

The pressure load was applied to the pressure side of the blade. The cord of the blade was assumed to be aligned in the axial direction, which although not completely reflecting real application, was needed to reduce the bending moment in the axial direction to practically zero. A centrifugal load is created by rotation at an angular rotation of 1500 rad/s about the X-axis which is located 0.12 m below the root of the blade. A fixed boundary condition has been applied to the upper surfaces of the fir tree as seen in Figure 23. The temperature distribution determined in section *4.3 (Temperature Loading*) has been applied to all surfaces of the blade and the upper surface of the root as it would also be in direct contact with the gas path. All surfaces of the blade root below the upper surface are assumed to be insulated (heat flux $q_x = 0$ W).

4.8.4 Convergence Study

Limited convergence studies were conducted with three dimensional models as the general mesh optimization procedure was to increase the element size until an input file was successfully submitted for analysis with a solution achieved within several hours. Comparisons were conducted on an undamaged blade between linear meshes and quadrilateral meshes. Initially, linear elements with 31836 nodes were used which is less than the 122736 nodes for a quadratic model. A substantial difference in processing time was observed, 2-3 hours for a linear model compared to 5-6 hours for a quadratic model. While the change in most results is negligible, the substantial change in calculated tip deflection, of critical interest to this study, was enough to rationalise using only quadratic elements. See Table 4 -Table 6 the model used in the study are shaded.

Table 4: Percentage change in solution for undamaged model with different meshes

Number of Nodes	Magnitude of Nodal Displacement [m]	Deflection [m]	Elongation [m]	Frequency at Mode 1 [Hz]
31836	$7.53x10^{-05}$	$5.86x10^{-06}$	$7.36x10^{-05}$	338
122736	$7.55x10^{-05}$	$6.89x10^{-06}$	$7.37x10^{-05}$	345
% Difference	0.31%	16.28%	0.08%	2.05%

Table 5: Change in solution for model a 1.1 mm elastic-plastic crack with different meshes at 1155 K

Number of Nodes	Magnitude of Nodal Displacement [m]	Deflection [m]	Elongation [m]	Frequency at Mode 1 [Hz]
40386	$1.07x10^{-04}$	-7.13E^{-05}	$7.64x10^{-05}$	340
156966	$1.08x10^{-04}$	$-7.27x10^{-05}$	$7.65x10^{-05}$	344
% Difference	3.29%	7.64%	-0.76%	1.46%

Table 6: Change in solution for a 1.1 mm elastic-plastic crack with different meshes at 955 K

Number of Nodes	Magnitude of Nodal Displacement [m]	Deflection [m]	Elongation [m]	Frequency at Mode 1 [Hz]
40386	8.33E-05	-4.50E-05	6.80E-05	358
156966	8.35E-05	-4.60E-05	6.75E-05	362
% Difference	0.22%	2.33%	-0.75%	1.11%

As seen in the two-dimensional models small deflections (Table 4) are very sensitive to mesh size, but as the deflections grow larger (Table 5 and Table 6) the percent difference in solutions reduces substantially. The percent difference reduces further at lower temperature distributions. Convergence has not been achieved but this error is deemed acceptable as any increase in element count leads to unacceptably long processing times, assuming a solution can even be achieved. Again, the study is only concerned with the change in tracked parameters and thus should remain relatively unaffected by model accuracy.

5 Results

5.1 Undamaged Internally Air Cooled Blade

The resulting temperature distributions for an undamaged internally cooled turbine blade are shown in Figure 24.

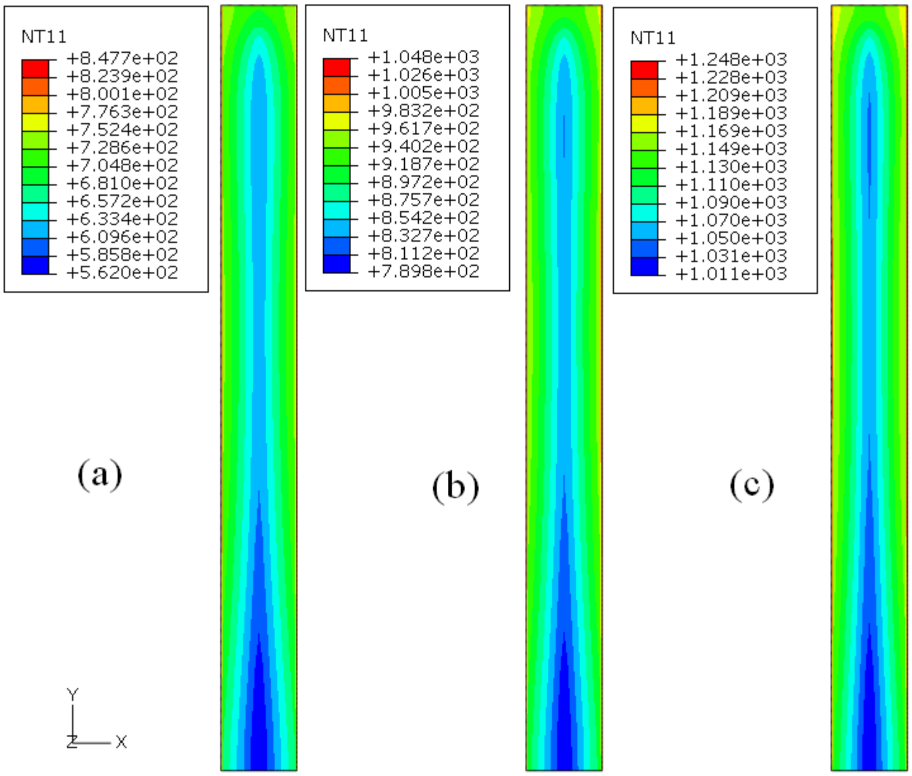

Figure 24: Temperature distribution within the cross-section of an undamaged coated turbine blade for median temperatures of 755K (a); 955K (b); and 1155K (c)

Examining Figure 25, it is readily apparent that while the applied surface temperatures from (a) to (c) have increased by 200 K, the resulting relative temperature distribution remains practically unchanged. It can also be seen that the applied heat flux has created a temperature gradient of approximately 200 K between the surface and the cooling channels at the centre of the blade.

Figure 24 shows the nodal temperature distribution across the blade thickness at midspan for a surface temperature of 1248 K. The sharp drop in temperature across the TBC can be clearly seen. The TBC effectively reduces the temperature by approximately 100 K. The temperature is further reduced across the substrate to eventually reach a low of 1055 K at the center of the blade. The total difference of temperature from the surface to the cooled center of the blade is 195 K at midspan; this results in an average substrate temperature of approximately 1100 K. The two lower surface temperature conditions follow a similar distribution except that all temperatures are correspondingly reduced by 200 K and 400 K respectively.

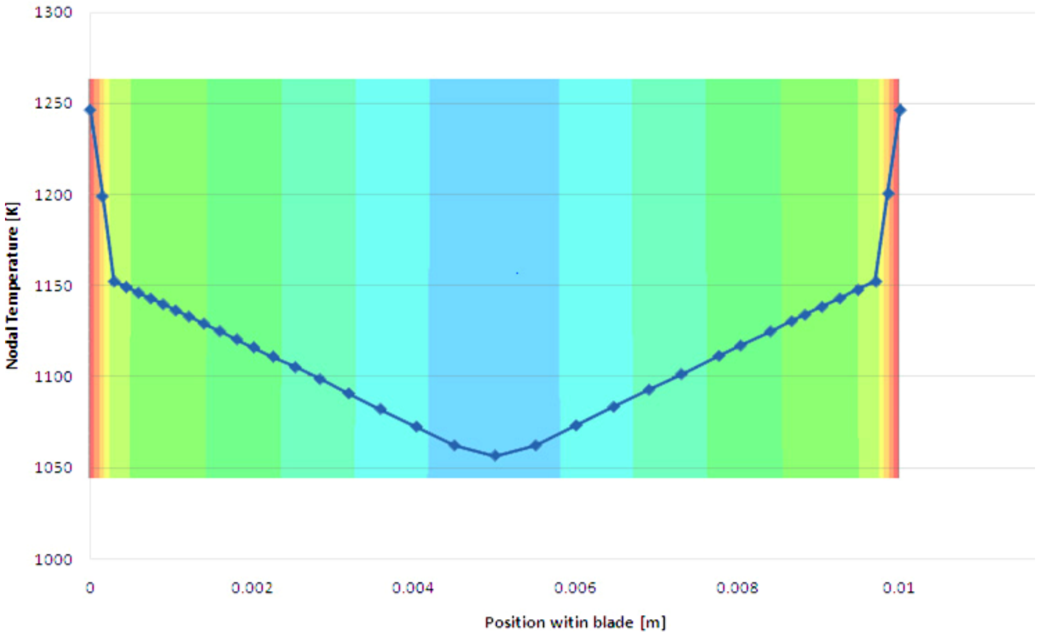

Figure 25: Nodal temperature distribution across the blade thickness at midspan

The von Mises stress distribution is shown in Figure 26. The stress averages approximately 273 MPa and increases in magnitude towards the root of the blade where a maximum value of 329 MPa occurs at the lower corners of the substrate. Stresses within the TBC are much smaller only 100 MPa. The stress within the substrate decreases only slightly with temperature.

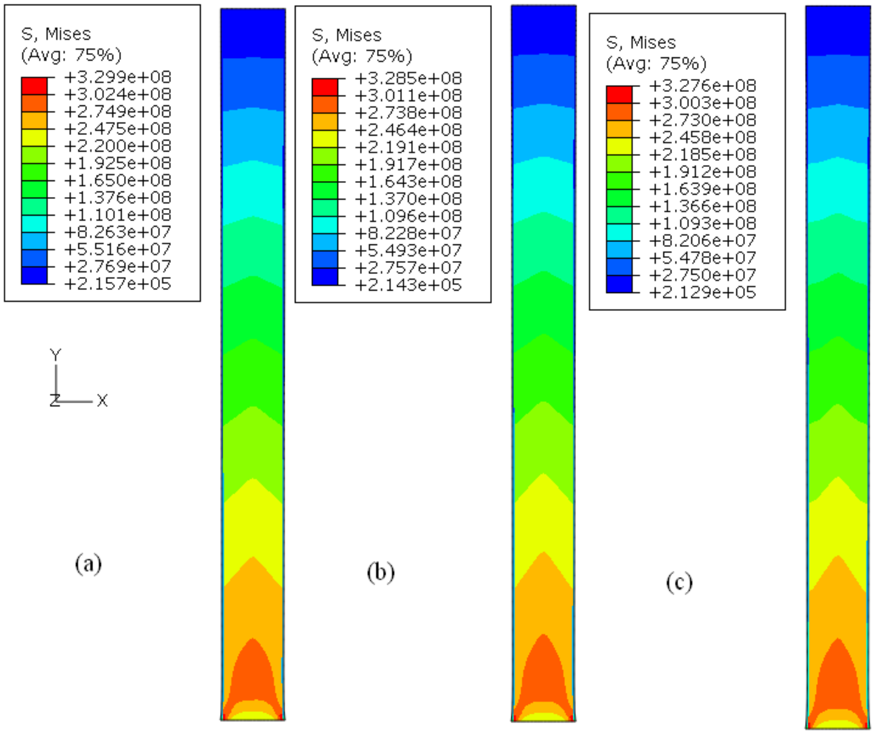

Figure 26: von Misess stress distribution in an undamaged coated blade under a centrifugal force at 1500 rpm and different median temperatures: 755K (a); 955 K (b); and 1155 K (c)

The resulting deflection of the blade was measured by analysing the nodal displacement. Nodal displacements in Figure 27 show that: the magnitude of the nodal displacement is greatest at the tip of the blade, and the nodal displacements in the x-direction, representing the deflection of the blade, are relatively small compared to the nodal displacements in the y-direction, representing the elongation of the blade. Sampling the nodal displacement across the top of the cross-section and averaging the values result in an average tip nodal displacement, or deflection of $1.88\text{x}10^{-5}$m. In contrast, blade elongation is nearly an order of magnitude larger ($1.03\text{x}10^{-4}$ m). This highlights the much larger impact of centrifugal forces compared to the pressure difference across the blade.

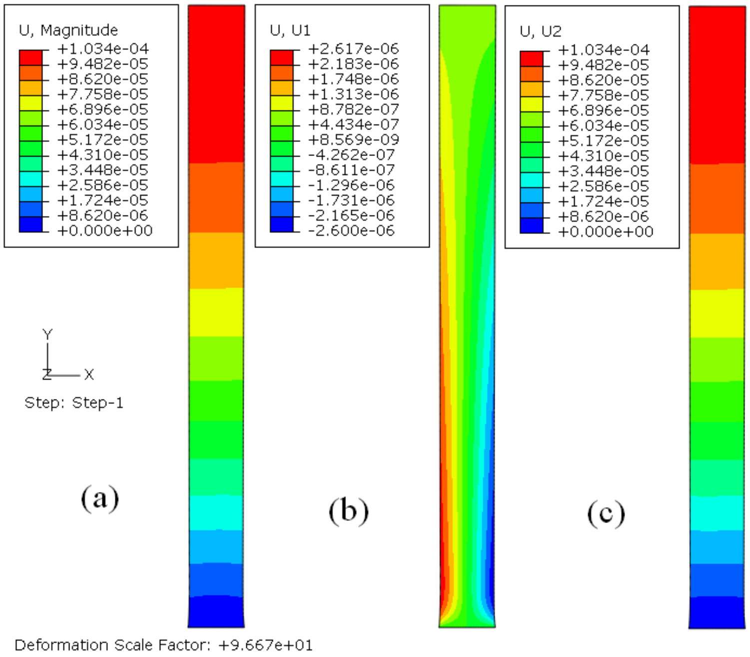

Figure 27: Magnitude of nodal displacement (a), nodal displacement in the x-direction (deflection) (b), nodal displacement in the y-direction (elongation) (c), at the highest temperature state

The magnitude of all displacements, in both x and y directions, increase with applied surface temperature. The tip displacement as a function of mean applied surface temperature is displayed in Figure 28. The relationship is nearly linear in the investigated temperature range.

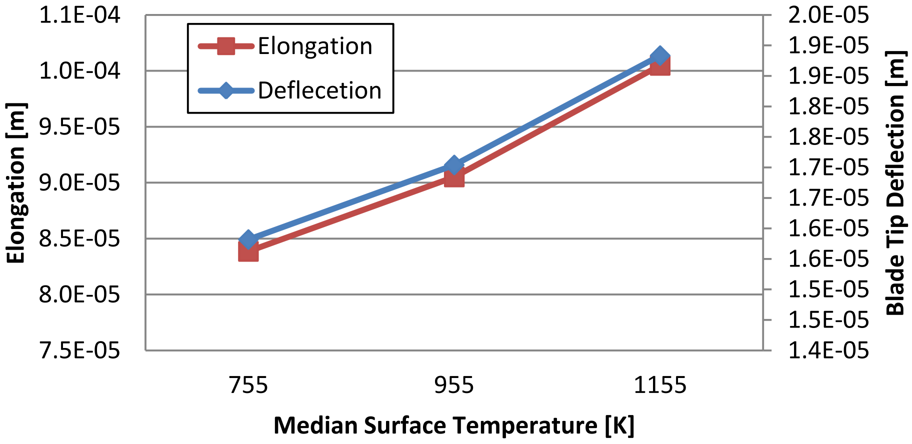

Figure 28: Static displacement of the blade tip at various surface temperatures

The base state (a) and the first six two-dimensional modes of vibration (b)-(g) for the considered blade are illustrated in Figure 29.

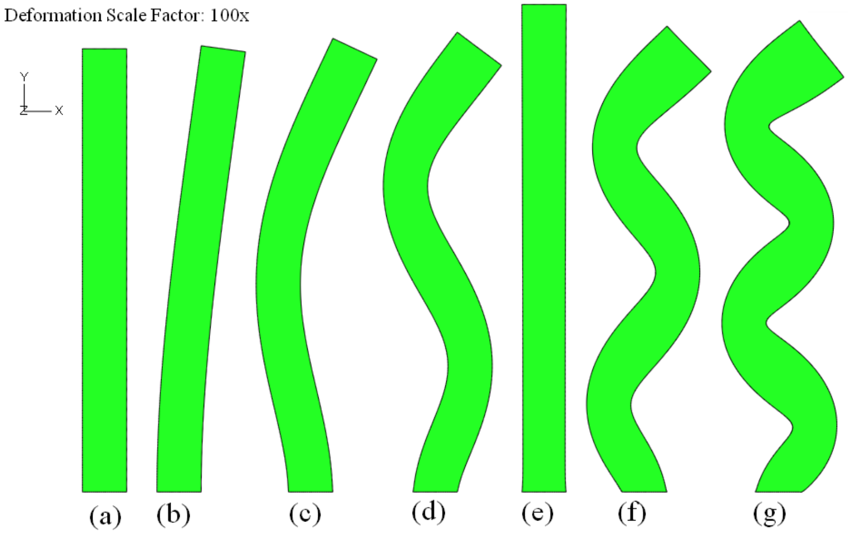

Figure 29: Base state and first six 2D modes of vibration for an undamaged blade: Base state (a); Mode 1 (b); Mode 2 (c); Mode 3 (d); Mode 4 (e); Mode 5 (f); Mode 6 (g)

The calculated frequencies are summarized in Table 7 for the first six modes at different surface temperature conditions.

Table 7: Natural frequencies for the first six modes of vibration

Mode	Natural Frequency (Hz)		
	755[K]	955[K]	1155[K]
1	748	721	686
2	4497	4329	4119
3	11899	11456	10897
4	12242	11785	11186
5	21730	20921	19896
6	33287	32048	30472

Inspecting frequencies allows assessing how close they are to the excitation frequency (rpm) during use and thus the probability of a blade falling into resonance vibration seems to indicate that no shift exists at any mode to cause this. For each mode, the natural frequency of vibration decrease with temperature. Higher vibrational modes have higher natural frequencies.

5.2 Blade With a TBC Defect

A TBC defect changes the steady state temperature distribution as seen in Figure 30. The surface temperature boundary condition is applied at the TBC defect location directly to the substrate and creates a visible hotspot allowing a much higher temperature to occur within the substrate, particularly around the surface. The temperature is also raised at the interior of the blade, increasing the median temperature of the substrate at midspan by 52 K.

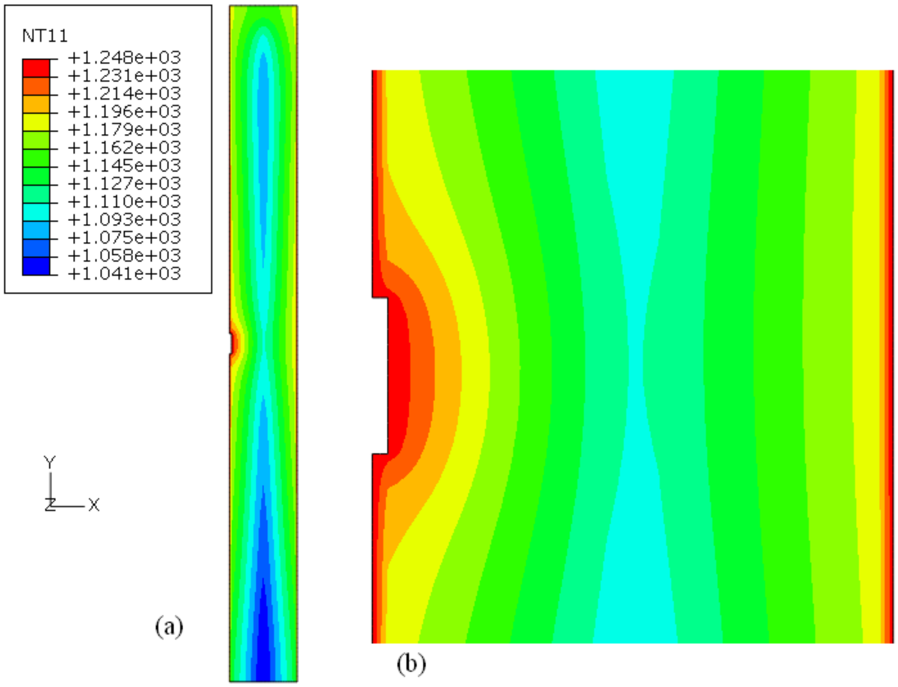

Figure 30: Temperature distribution on a blade with simulated TBC defect

The TBC defect results in only a small change in total nodal displacement as summarised in Table 8. The overall blade deflection decreases slightly to 1.85x10^{-5}m. The defect can result in a small difference as can be seen between the deflections of the undamaged model and those of the blade with 3 mm defect.

Table 8: Deformation change in a blade with a small (3 mm) TBC defect, reference to the undamaged state

Temp [K]	Magnitude of Nodal Displacement (U)			Tip Deflection			Elongation		
	Damaged [m]	Un-Damaged [m]	% difference	Damaged [m]	Un-Damaged [m]	% difference	Damaged [m]	Un-Damaged [m]	% difference
755	8.522E-05	8.533E-05	0.13%	1.503E-05	1.582E-05	5.14%	8.388E-05	8.385E-05	-0.04%
955	9.210E-05	9.210E-05	0.01%	1.658E-05	1.704E-05	2.76%	9.059E-05	9.051E-05	-0.09%
1155	1.023E-04	1.022E-04	-0.04%	1.845E-05	1.883E-05	2.04%	1.006E-04	1.005E-04	-0.11%

The localised temperature increase due to a small TBC coating defect has only a small effect on natural vibrational frequencies. Natural frequencies for the first six modes along with the percent differences from the undamaged model are shown in Table 9. It can be seen that the natural frequency of the 3mm TBC defect model has been lowered slightly for all modes and at all temperature distributions relative to the undamaged model.

Table 9: Natural frequencies for a blade with a 3 mm long TBC defect at midspan

Mode	Frequency [Hz]								
	755[K]			955[K]			1155[K]		
	Un-Damaged	Damaged	% Difference	Un-Damaged	Damaged	% Difference	Un-Damaged	Damaged	% Difference
1	748	748	0.02%	720	720	0.04%	685	685	0.04%
2	4496	4492	0.10%	4329	4323.	0.15%	4119	4112	0.16%
3	11899	11898	0.01%	11456	11454	0.02%	10897	10895	0.02%
4	12242	12239	0.02%	11785	11779	0.05%	11185	11179	0.05%
5	21730	21713	0.08%	20921	20897	0.11%	19896	19871	0.13%
6	33286	33283	0.01%	32048	32039	0.03%	30471	30462	0.03%

Figure 31 illustrates the change in temperature distribution as the TBC defect size increases. The hot spot grows noticeably at each step until the entire pressure side of the blade is exposed to the surface temperature. This results in a large portion of the substrate experiencing peak temperatures of 1248 K at the hottest investigated surface temperature condition. Temperature distributions for 755 K and 955 K surface temperature appear identical but with a reduction of 400 K and 200 K respectively.

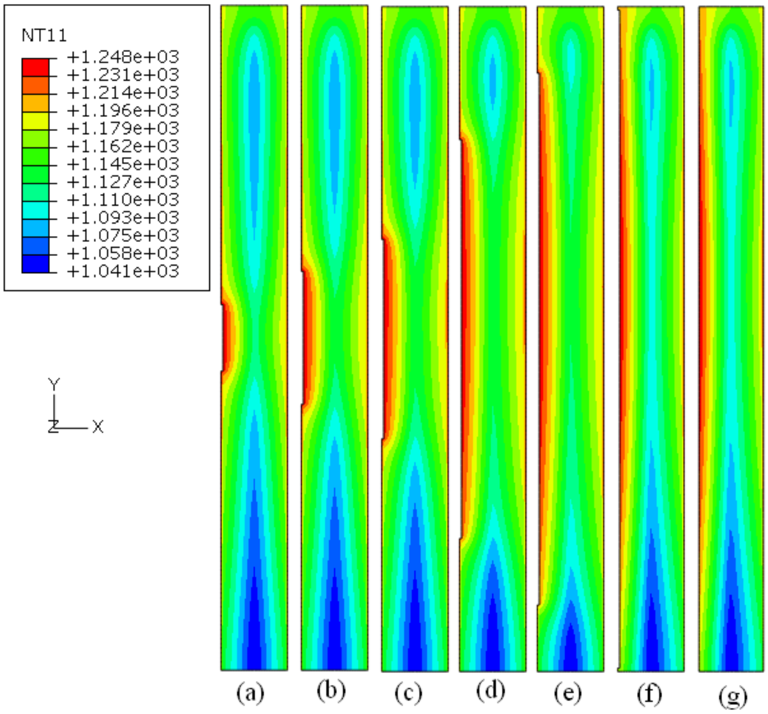

Figure 31: Change in temperature distribution with increasing TBC defect size: 10 mm (a); 20 mm (b) 30 mm (c); 60 mm (d); 80 mm (e); 99 mm (f); and no TBC present (g)

The resulting change in static deflection for the respective temperature profiles is summarised in Figure 32. The deflection is seen to decrease and switch to negative values as the size of the TBC defect grows meaning that the blade deflects against the pressure load for TBC defects greater than 60 mm (Figure 33). The elongation of the blade is seen to increase with temperature but the change is very slight (Figure 33). The elongation is as much as 185% larger than the tip deflection. However, the tip deflection exhibits a much larger percent change and is thus considered more sensitive to TBC damage and therefore seems more appropriate for monitoring the blade health.

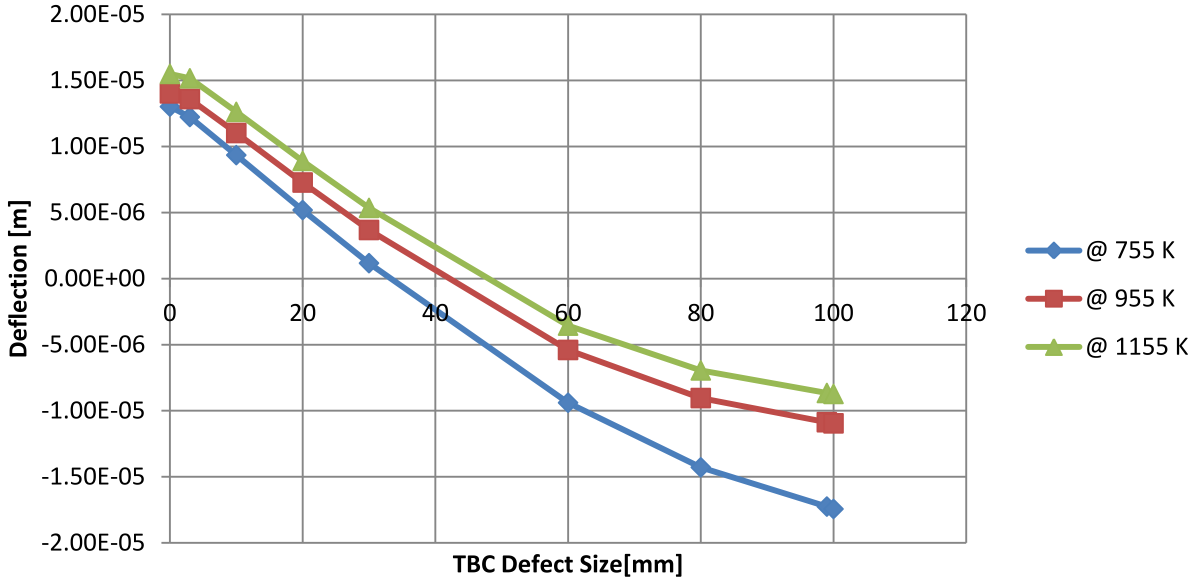

Figure 32: Effect of TBC defect size on blade tip deflection

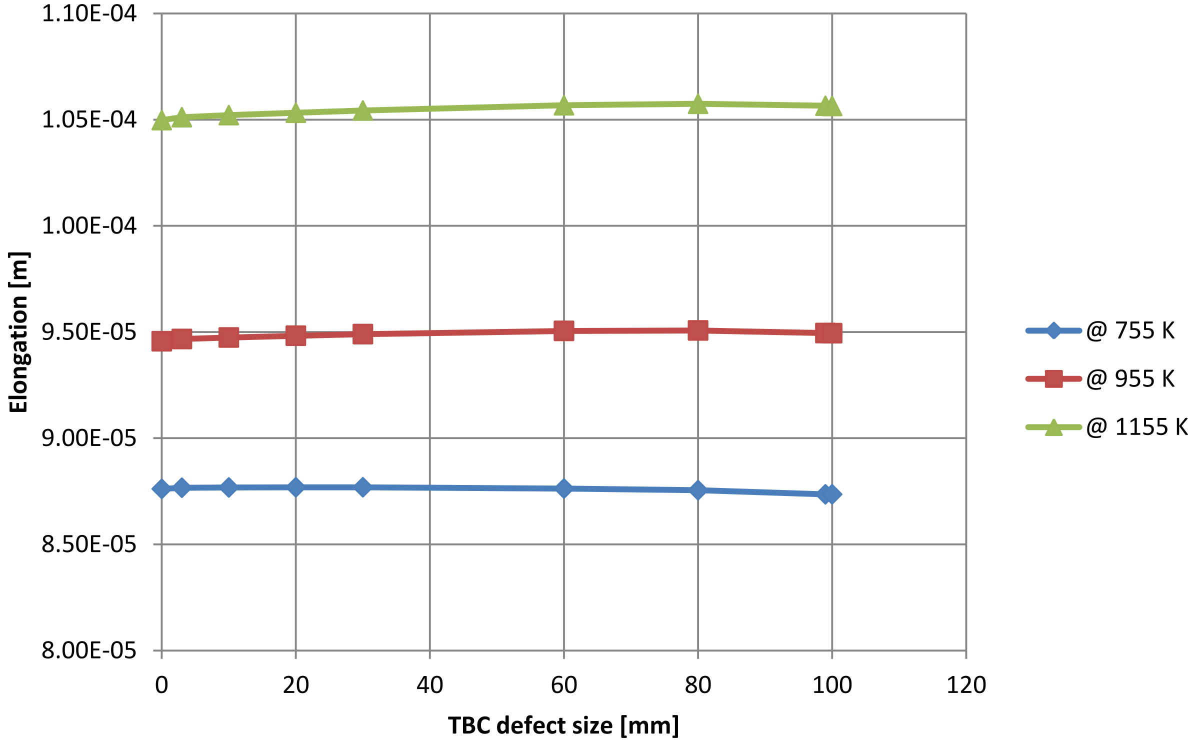

Figure 33: Effect of TBC defect size on blade elongation

Coating defects result in hotter and less stiff substrates leading to lower natural frequencies as summarised in Figure 34. Natural frequencies decrease with increasing TBC defect size. By inspection of the collected data it is noted that very little change occurs to the natural frequency of the model in relation to a growing TBC defect. The change in natural frequency from a completely undamaged cross-section to one with no TBC coating on the pressure side is greatest for the first mode of vibration. This occurs at the highest temperature and creates a percent difference of 1.76%. The smallest change exists within the 4th mode of vibration at the coolest temperature distribution and is 0.32%.

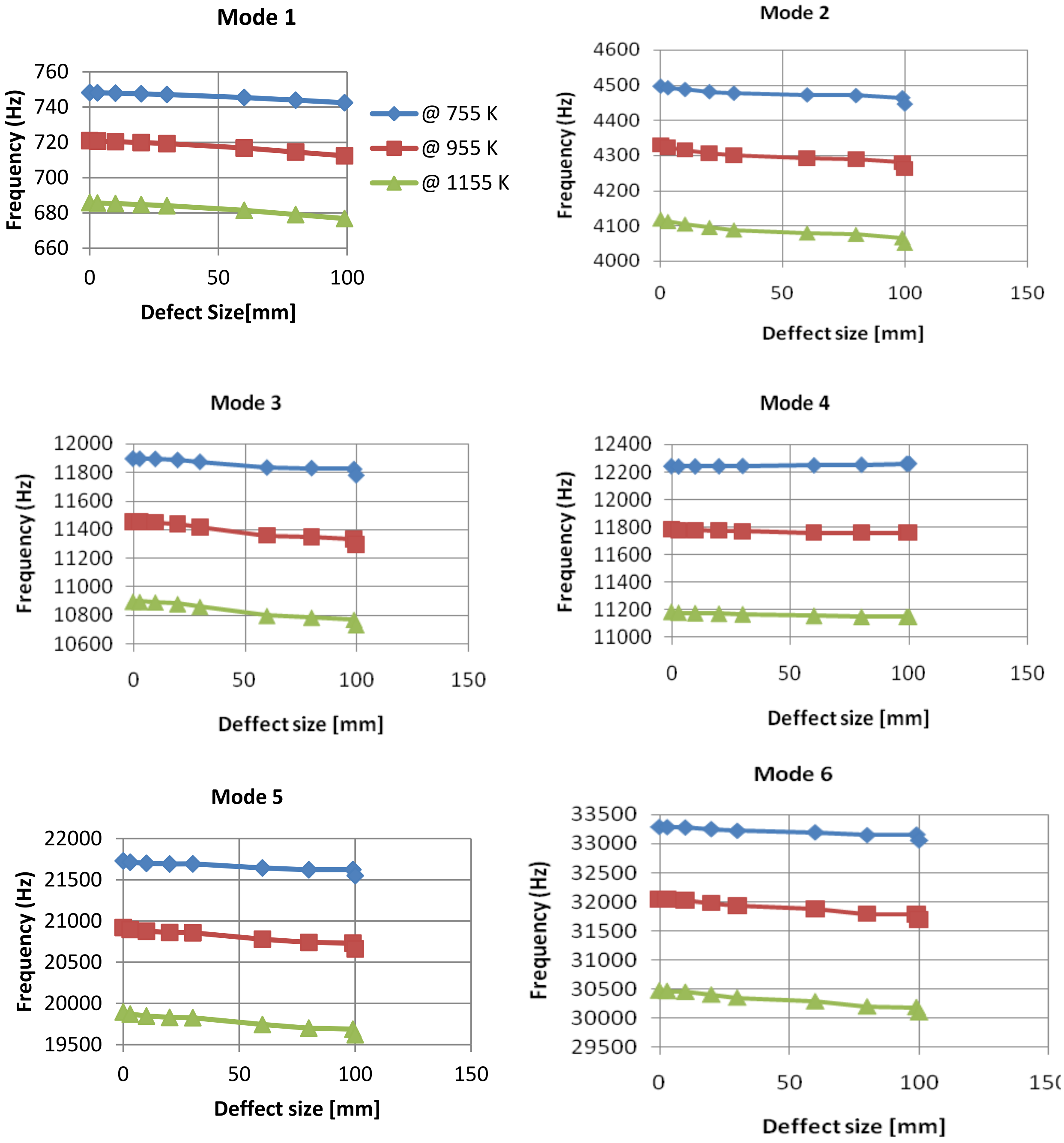

Figure 34: Frequency shifts as a function of defect size for the first six modes of vibration

5.2.1 TBC Defect Location

The effect of the location of the TBC defect was studied. Overall, the effect of a 10 mm long defect was found to have a small but measurable effect on both the static deflection and the natural frequency as its location changes from the root to the tip of the blade. Figure 35 illustrates the temperature distribution resulting from the introduction of a defect at various locations. The temperature of the substrate is notably raised around the defect and remains slightly lower at the root of the blade.

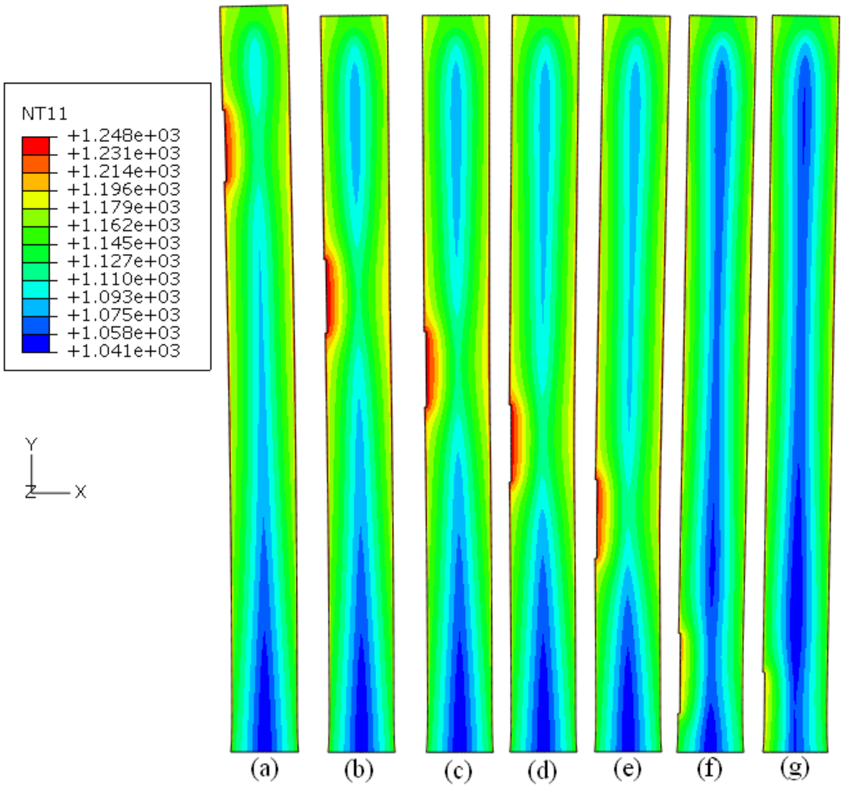

Figure 35: Temperature profile of a blade for different locations of a 1 cm TBC defect; distance from the blade root: 8 cm (a); 6 cm (b); 5 cm (c) 4 cm (d) 3 cm (e); 1 cm (f); 5 mm (g)

The effects of TBC-defect location on static tip deflection and blade elongation are illustrated in Figure 36 and 38 respectively.

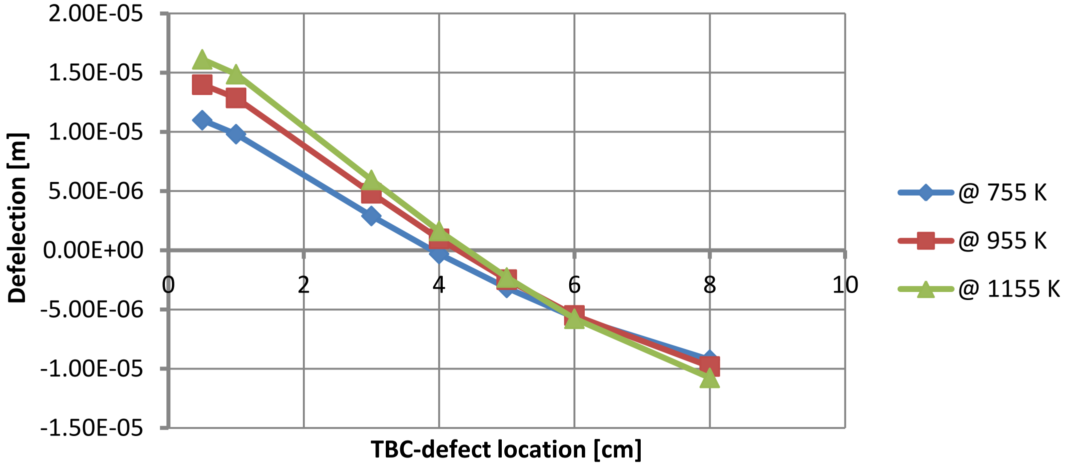

Figure 36: Tip deflection for different TBC defect locations

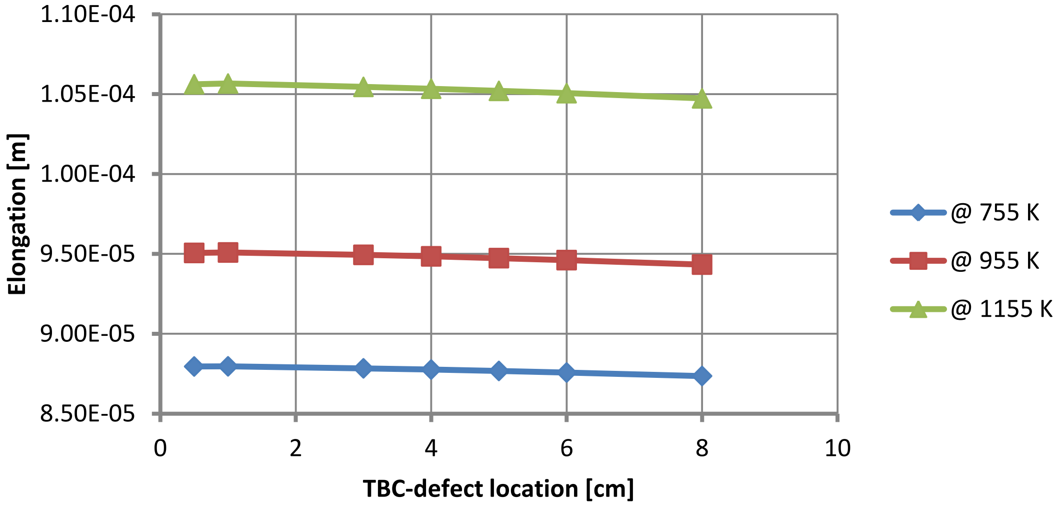

Figure 37: Blade elongation for different TBC defect locations

Comparing Figure 36 to Figure 37, it can be seen that the tip deflection is nearly an order of magnitude smaller compared to the elongation of the model. The blade elongation is consistently reduced when the defect moves from the root to the tip of the blade, however the change is very small. The tip deflection, although smaller in amplitude, shows a stronger dependence on the defect location. The tip deflection changes from positive (away from the higher pressure side) to negative (towards the pressure side) as the TBC defect moves towards the blade tip and has a value zero when modeled at 4 cm from the blade root.

The effect of the TBC defect location on natural vibrational frequencies is illustrated in Figure 38.

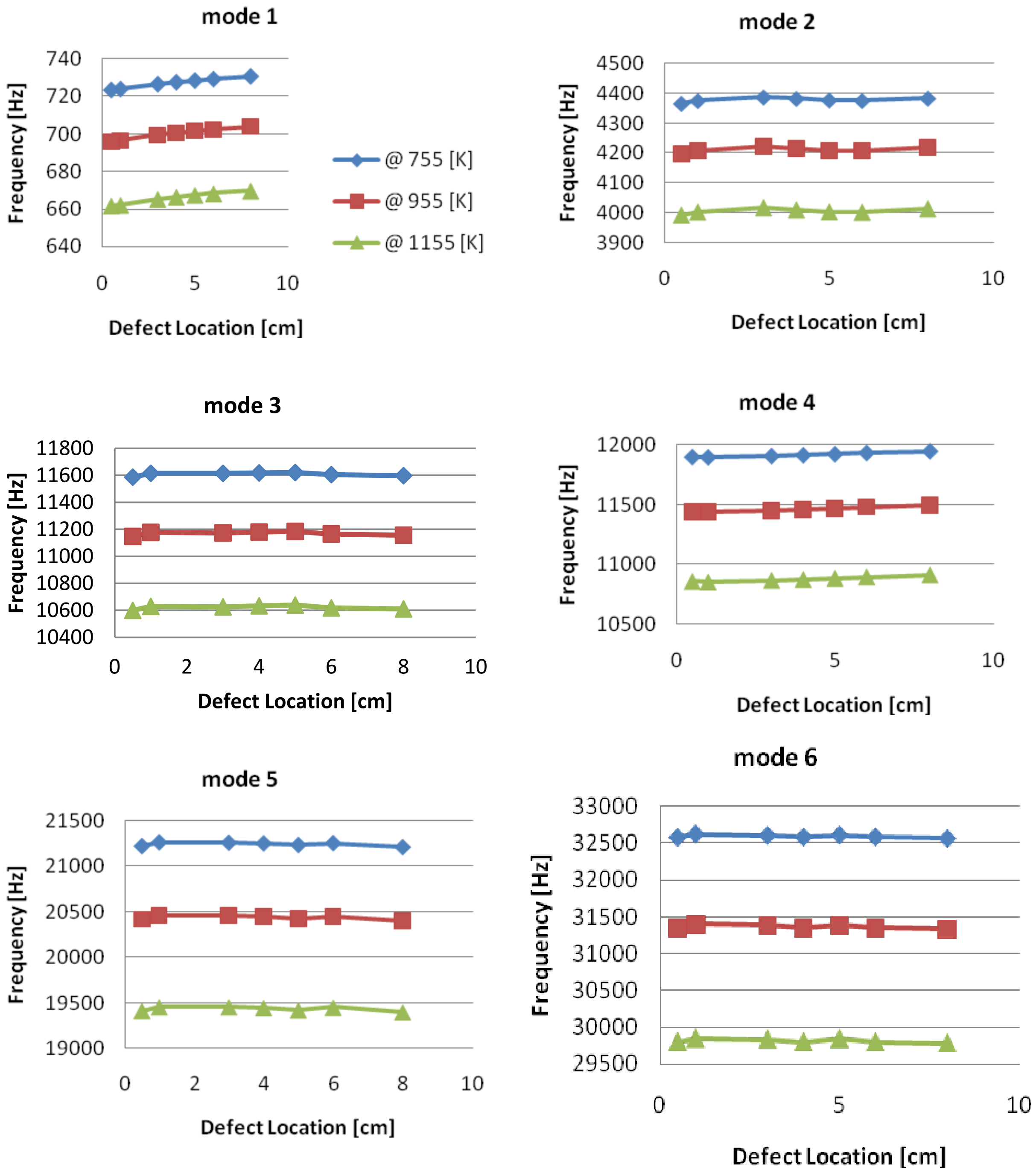

Figure 38: Effect of TBC-defect location on natural frequencies

Overall, the dependence of natural frequencies on TBC defect location is small. The greatest change occurs within the first mode of vibration at the median surface temperature of 1155 K. In this case, the percent difference between a TBC defect at the root (0.5 cm) and near the tip (8 cm) of the blade is only 1.23%, a shift of 7.5 Hz.

5.3 Effect of Cracks

Cracks of varying depths were simulated at several locations on the blade. Resulting temperature distributions are similar to what has been shown previously for TBC coating defects with higher temperatures around the crack tip where the substrate is exposed directly to the applied surface temperature. Figure 39 shows the heat distribution around a crack with a depth of 3 mm at the hottest applied temperature condition and is illustrative of all modeled crack depths. The temperature distributions for 755 K and 955 K surface temperature conditions appear identical but with a reduction of 400 K and 200 K respectively to the distribution created by the 1155 K surface temperature condition.

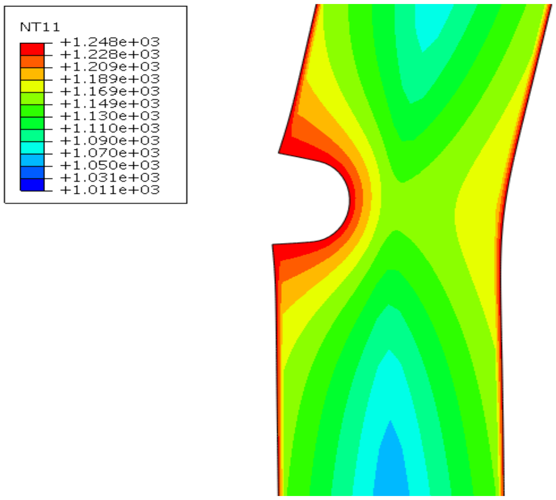

Figure 39: Temperature distribution near a 3 mm deep crack at 1155 K surface temperature

The introduction of a crack has a very strong effect on stress distribution as shown in Figure 40. The introduction of a circular crack creates a stress concentration at the crack tip 3-4 times greater than would be present in an undamaged model. The stress present at the crack tip increases by this same factor in addition to an increase in nominal stress as the crack approaches the root of the blade. Therefore, the stress at the crack tip is highest at the blade root.

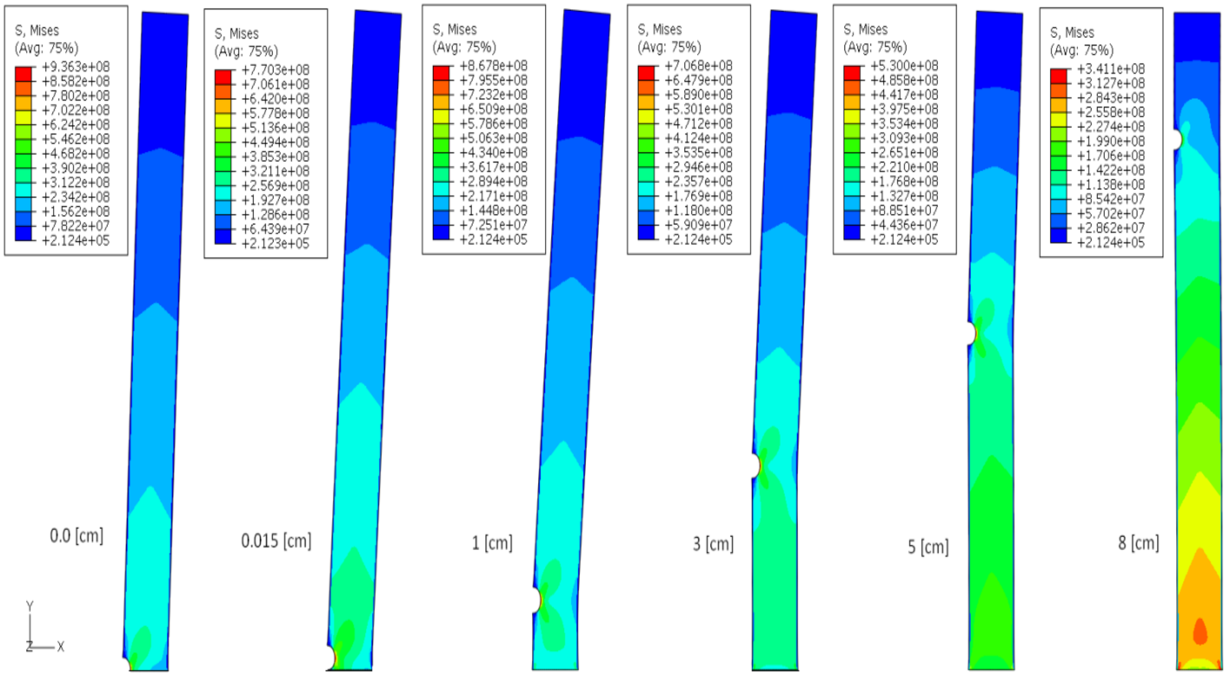

Figure 40: Stress distribution for a 1.5 mm deep crack at various locations and 1155 K blade median temperature

Figure 41 (a)-(b) shows that tip deflection and elongation increase as a 3 mm crack approaches the blade root. The introduction of a circular crack into the model can greatly increase the static deflection of the blade. A 1.5 mm crack introduced at 5 cm from the blade root produces a deflection of $5.20\text{x}10^{-05}$ m at a median temperature of 1155 K, a change of 93**%** from the undamaged model. A 1.5 mm crack introduced at 0.5 cm from the blade root at the same temperature produces a deflection of $1.53\text{x}10^{-04}$ m, a change of 156% from the undamaged model. The blade elongation also increases as the crack is modeled closer to the root of the blade. However the percent change is smaller compared to the change in blade deflection. A 1.5 mm long crack at 5 cm and 0.5 cm from the root only produces an increase of 0.22% and 1.61% respectively in blade elongation at the same operating conditions. Inspecting Figure 41 also yields some unexpected results. As the crack is modeled below a distance of 0.5 cm from the root, the deflection begins to decrease. Also the tip deflection becomes negative when the crack is modeled above the blade midspan. These effects can be seen at all temperatures.

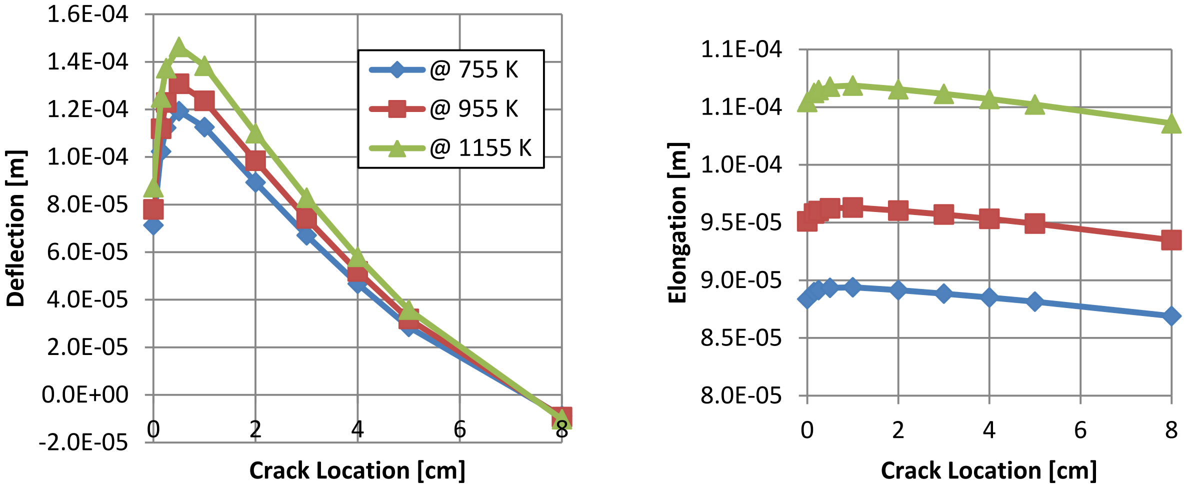

(a) (b)

Figure 41: Nodal displacement as a function of crack location from the blade root: deflection (a); elongation (b)

To study the effect of crack size on the blade, the crack depth was increased by 0.5 mm in successive steps as shown in Figure 42. The stress concentration nearly doubles, increasing from 530 MPa to 902 MPa as the crack size increases from 1.5 mm to 3 mm.

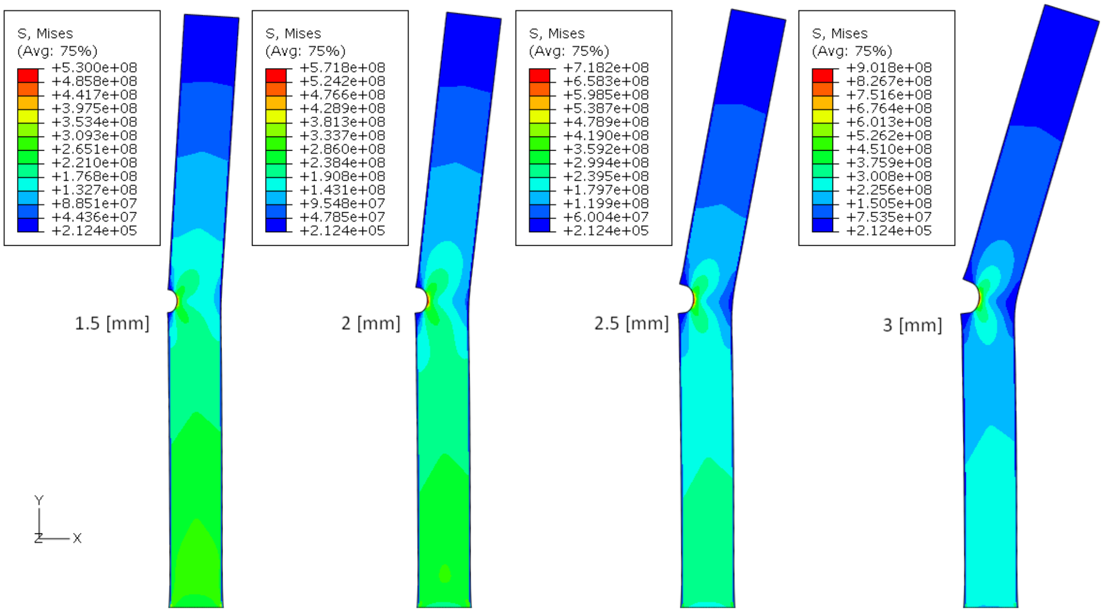

Figure 42: Stress distribution and blade deflection for varying crack depths located at 5 cm from the blade root at 1155 K

The effect of crack depth on static tip deflection and elongation for a crack located at midspan is plotted in Figure 43.

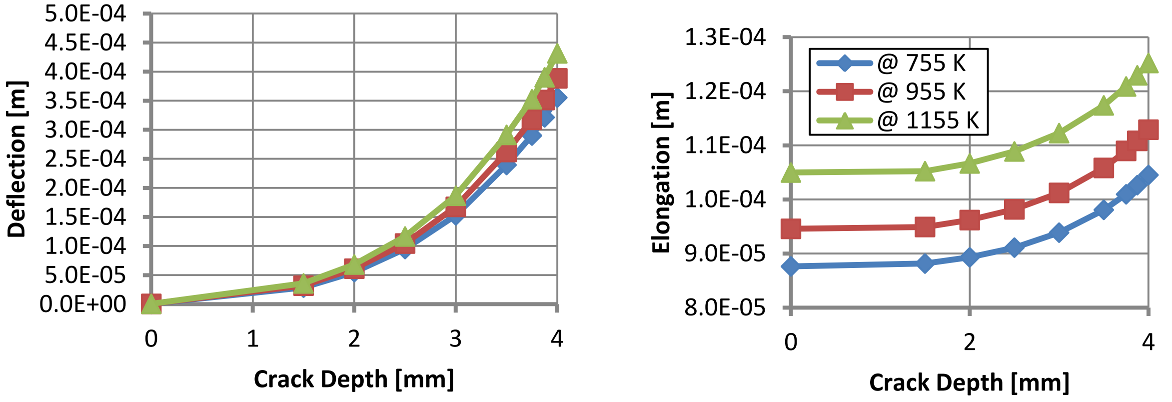

(a) (b)

Figure 43: Nodal displacement as a function of crack depth at midspan: deflection (a); elongation (b).

The crack depth has a strong effect on the blade deflection. As the crack size increases, the tip deflection increases at an accelerating rate. The change of tip deflection from 1.88x10^{-05} m for an undamaged blade to 2.94x10^{-04} m for a blade with a 3.5 mm deep crack at mid-span is large and corresponds to a percent change of 176%. By studying the stress distribution at cracks sizes greater than 3 mm it can be noted that peak stresses greater than 900 MPa occur.

The blade elongation also shows a response to a propagating crack and while the magnitude of the elongation relative to that of the tip deflection seems large, the percent change in elongation from a healthy blade to a damaged blade is relatively small with only an 11.2% change is exhibited for a crack propagating to a depth of 3.5 mm.

Natural frequencies steadily decrease as the crack propagates into the blade. The rate at which this occurs, as well as the overall change, depends on each specific vibrational mode. The percent changes with reference to an un-damaged blade for the first 6 vibrational modes are listed in

Table 10 and are illustrated in Figure 44.

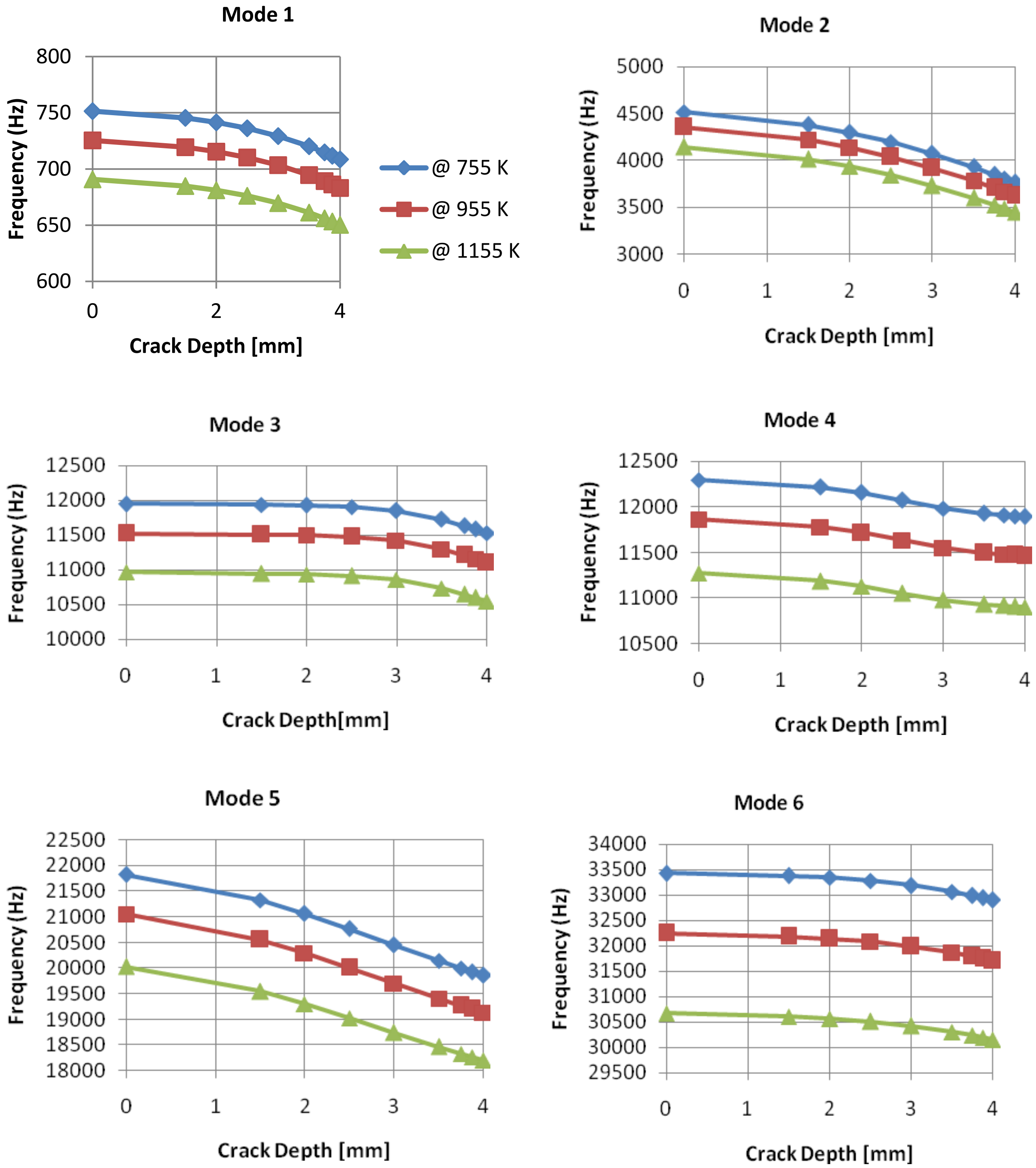

Figure 44: Effect of crack depth on natural frequency at mid-span

Mode 2, mode 5, and mode 1 (in increasing order) exhibit the largest change and thus sensitivity to crack propagation. Of greatest interest is the change in mode 1 and mode 2 as the motions resulting from these vibrations are likely to have the greatest measurable amplitude.

Table 10: Percent change in natural frequency due to a 4 mm surface crack

Median Temp [K]	Mode 1	Mode 2	Mode 3	Mode 4	Mode 5	Mode 6
755	5.7%	16.6%	3.5%	3.3%	9.0%	1.6%
955	5.8%	16.8%	3.7%	3.4%	9.1%	1.7%
1155	5.9%	16.8%	3.8%	3.3%	9.1%	1.7%

5.4 Modelling With Elastic-Plastic Material Behaviour

The modelling result for the undamaged blade and blades with TBC defects show only a moderate change of about 1% when the material behaviour is changed from purely elastic to elastic-plastic behaviour. This is due to the relatively low stress level below the material yield strength.

5.4.1 Two-Dimensional Cooled Blade With TBC and Crack Damage

Little change can be seen between elastic and elastic-plastic models at low blade temperature. At high temperature however, the decrease in yield strength leads to plastic deformation around the crack as can be seen in Figure 45 for a 3 mm deep crack (denoted in red).

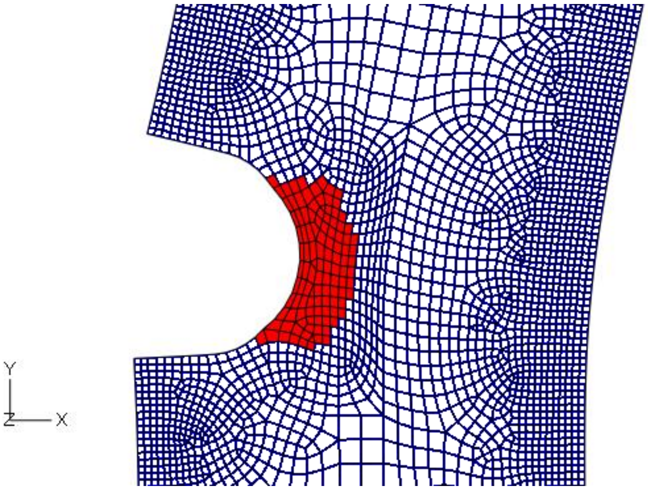

Figure 45: Local yielding around a 3 mm crack under elastic-plastic material behaviour consideration at 1155 K surface temperature condition

The effect of yielding is clearly illustrated in Figure 46 (a) and (b) in the difference between stress distributions at the median temperature of 955 K, just before the drop in yield strength, and 1155 K after the drop. At 1155 K, the tip deflection increases exponentially starting at 3 mm crack-depth and reaches a value of 4 mm at a crack depth of 4 mm. This exponential increase suggests infinite tip deflection and thus blade failure for cracks deeper than 4 mm. As with elastic models, the elongation of the blade remains relatively constant at shallow crack depths but with elastic-plastic data increases drastically at greater crack depths and higher temperatures (Figure 46 b).

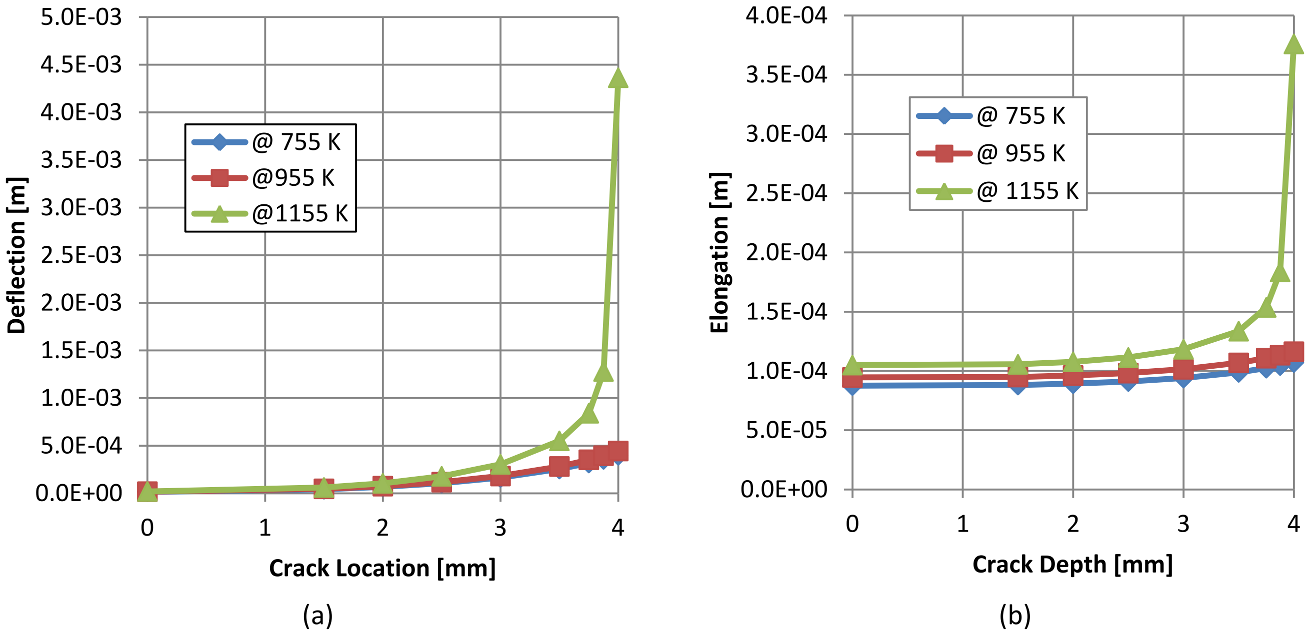

(a) (b)

Figure 46: Nodal displacement as it relates to crack depth at midspan: tip deflection (a); blade elongation (b)

As the crack depth is increased or located closer to the root of the blade, warnings or errors concerning overly large strain values are indicated by *Abaqus* solver and no solution can be achieved. At the point labelled “erroneously low” in Figure 47 (a), no solution is achieved and the result of the last successfully solved time step is used instead. Comparing Figure 46 (a) and Figure 47 (a) it can be seen that the relationship of crack depth to tip deflection is consistent but the critical crack depth decreases as the crack location approaches the blade root.

Figure 47 (b) displays the relationship between crack depth and tip deflection for a crack located at 8 cm above the blade root. At shallow crack depths (< 2.5 mm) the deflection remains negative as observed in the elastic models. At larger crack depths of 3 to 3.5 mm however, the deflection becomes positive. For both positive and negative deflections, the magnitude remains relatively small (-1.0×10^{-5} to 2×10^{-5} m) compared to values obtained for cracks close to the blade root.

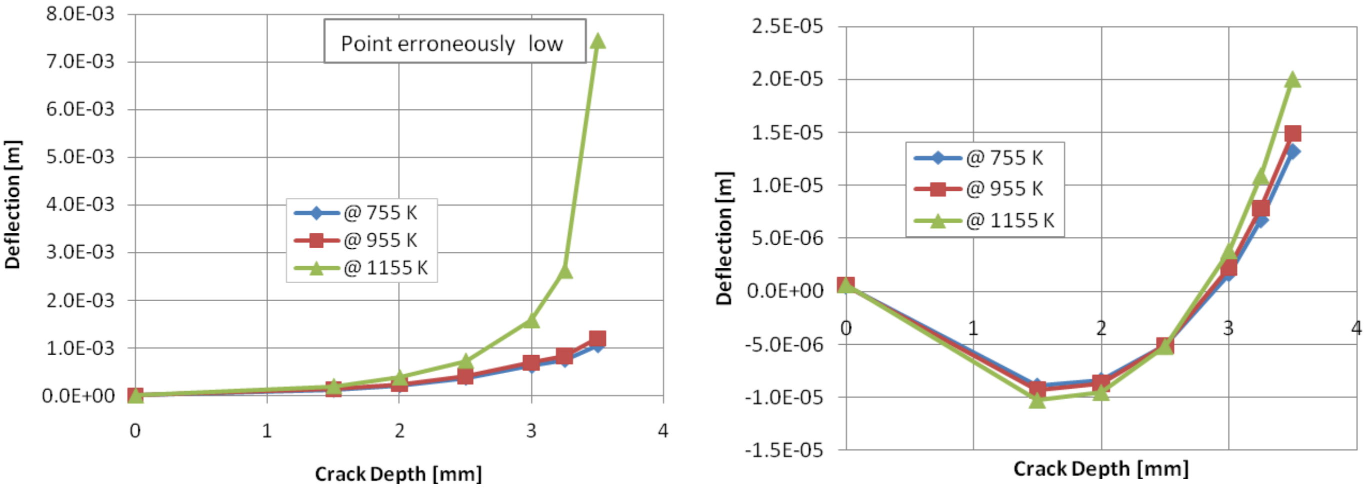

(a) (b)

Figure 47: Tip deflection in relation to crack depth: crack located at 0.5 cm (a); crack located at 8 cm (b)

The effect of crack location on blade tip deflection under elastic-plastic material behaviour consideration is summarised in Figure 48.

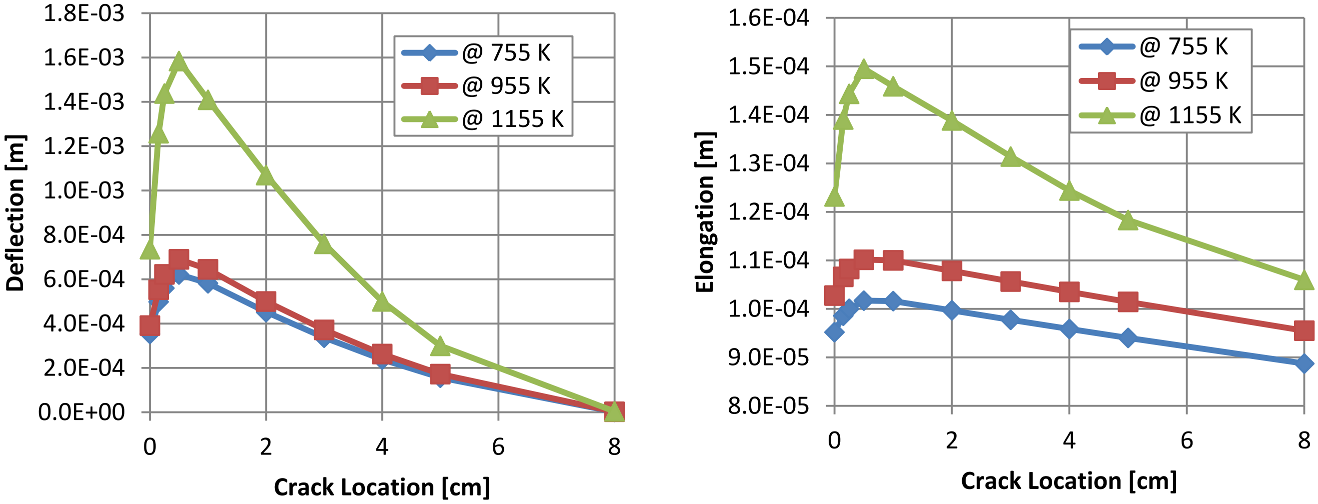

(a) (b)

Figure 48: Nodal displacement as a function of crack location for a crack depth of 3 mm: deflection (a); elongation (b)

It is surprising that the deflection seems to first increase as the crack moves towards the blade root, but then decreases again close to the root. At greater crack depths and critical crack locations close to the blade root, large blade deflections (≈$1.6\text{x}10^{-03}$-$3.96\ \text{x}10^{-03}$ m) can be seen but only at the hottest temperature states. The blade elongation at hotter temperatures also shows a stronger response but the change is still small compared to the change in deflection.

5.5 Three-Dimensional Model Based on Elastic-Plastic Material Behaviour

Three-dimensional models exhibit similar trends to two-dimensional models. As a crack grows into the blade the effective stiffness is reduced and a change is seen in the static deflection (Figure 49). Again, the inclusion of plastic data creates larger deflections than those obtained using purely elastic behaviour at the highest temperature. In reference to the deflection of an undamaged model, the percent change is 21.33% with purely elastic data, and 29.65% with elastic-plastic data. The overall deflection is at the lower detectable limit, only $4.34\text{x}10^{-4}$ m. As in the two-dimensional models, the elongation of the blade remains relatively unaffected by the introduction of a crack changing by only 8.99% to a peak of $9.40\text{x}10^{-05}$m. Little change in elongation is seen in Figure 50 for all surface temperature conditions even with the addition of elastic-plastic data. Unlike the two-dimensional models the three-dimensional models exhibit a larger initial deflection with a magnitude greater than that of blade's elongation, $3.22\text{x}10^{-04}$ m deflection vs $8.59\text{x}10^{-5}$ m elongation. This allows the sum vector of the two tip displacement components, the total nodal displacement, to exhibit a much stronger relation to crack depth and location. As crack depth varies along the width of the blade the crack depth has been measured at its greatest depth which occurs just behind the leading edge of the blade where the profile is the thickest.

As the crack is modeled closer to the blade root the deflection is also seen to increase although no critical point can be conclusively identified. A crack depth of 0.6 mm at 0.7 cm from the blade root increases the magnitude of tip-deflection from $3.22\text{x}10^{-04}$ m to $3.83\text{x}10^{-04}$ m with respect to the undamaged blade. An increase of 9.64% compared to the deflection of an equal sized crack at midspan.

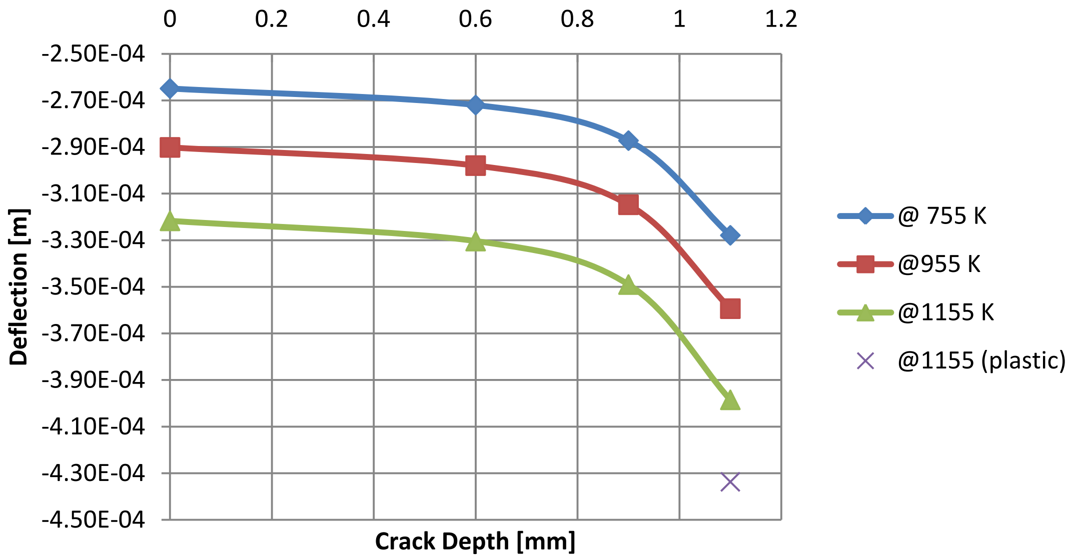

Figure 49: Relation of tip deflection to crack depth, three-dimensional model, measured from the leading edge

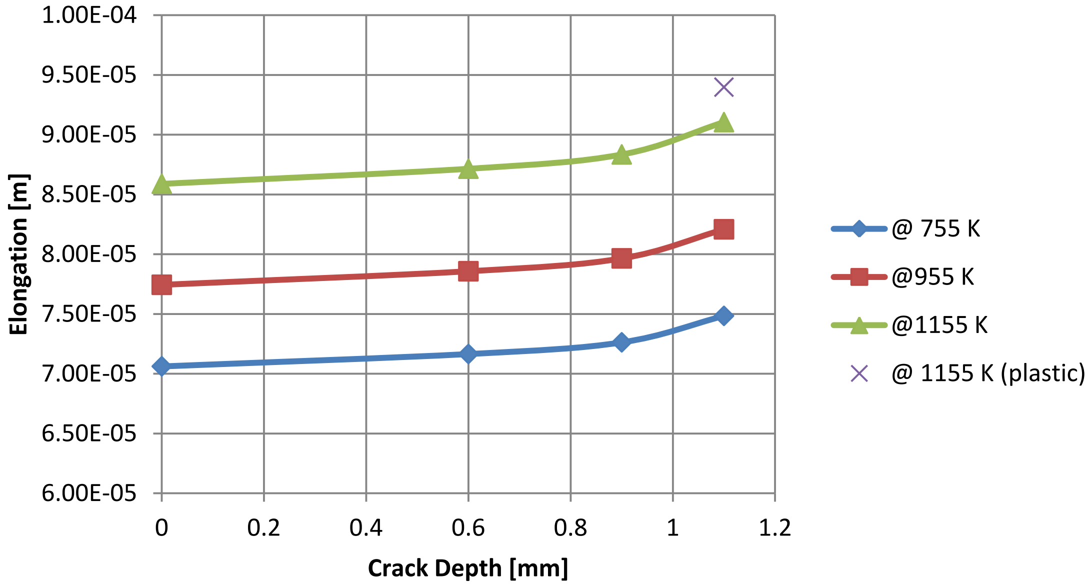

Figure 50: Relation of blade elongation to crack depth, 3-D model, measured from the trailing edge

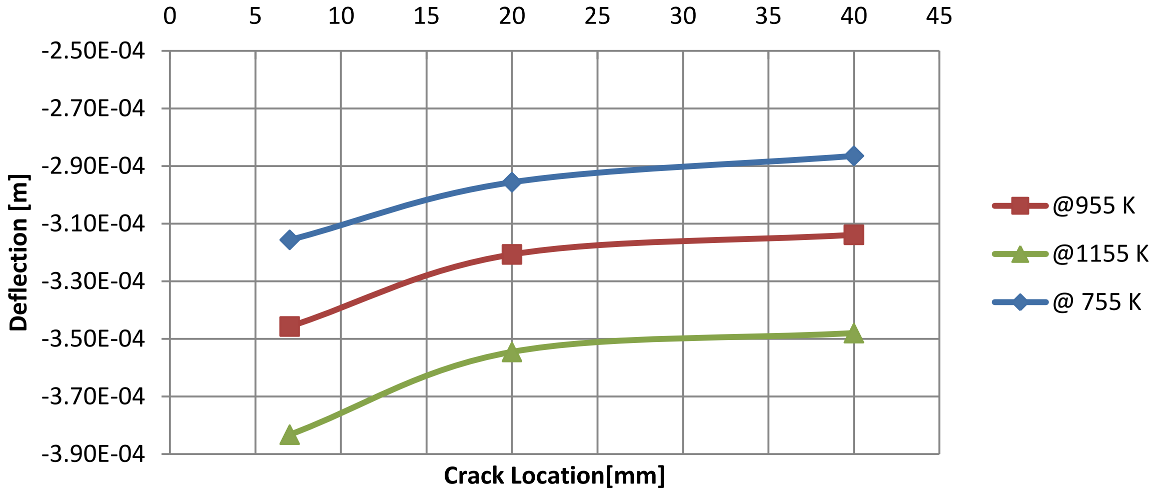

Figure 51: Relation of blade deflection to crack location for a 0.6 mm crack, elastic only

A small decrease in natural frequency is seen at all modes of vibration and the values at 1155 K are summarised in Table 11. A similar shift is seen at all other temperature distributions. The largest decrease exits at mode 3. This is the equivalent mode shape to mode 2 in the two-dimensional model.

Table 11: Natural frequency [Hz] shift caused by a circular crack at mid-span and 1115 K

Crack Depth	Mode					
	1	2	3	4	5	6
1.1	344.004	1728.54	2053.14	2501.02	5653.5	7166.67
0.9	344.589	1727.44	2070.55	2504.27	5651.72	7168.89
0.6	345.543	1730.7	2093.35	2510.28	5664.16	7188.07
0	345.894	1730.5	2104.25	2509.25	5655.06	7175.58

6 Discussion and Validation

6.1 Undamaged Blade

The simulated temperature drop across the TBC is less than the peak literature value of about 200 K [18] but does follow physical formulas closely (summarised in Table 12). The slight deviation from expectation may be due to the assumption of ideal interfaces between the coating and the substrate. A standard TBC coating is composed of many layers including: the bond coat, the thermally grown oxide, and the top coat between which interfacial defects may develop. These additional layers and possible defects are not considered in this study.

The cooling body heat flux further reduces the temperature experienced by another 100 K from the surface to the cooling channels. Again, this is in agreement with the one-dimensional heat transfer analysis conducted in *Appendix IV*. This reduction in temperature is sufficient to raise the operational temperature of the healthy blade.

Table 12: Heat transfer solution comparison to 1-D Fourier's law - validation

	Nodal temperature @ TBC/substrate interface [K]	Nodal temperature @ Center of blade [K]
Model	1152	1056
Physical Formula	1138	1040
Percentage Difference	1.22%	1.53%

The stress distribution is what is expected of a centrifugally loaded blade with a superimposed pressure load in that the stress can be seen to increase from essentially zero at the tip of the blade to its maximum at the root [54].

Table 13: Centrifugal stress at blade root - validation

	2D [MPa]		3D [MPa]	
	Average	Maximum	Average	Maximum
Model	324	409	233	371
Physical Equation	314		237	
Percentage Difference	3.1%	26.3%	1.7%	44%

As expected, the maximum stress within the cross-section occurs at the outside corners of the blade root and is within the elastic region of the material at all calculated temperatures. This raised stress is caused by the constraint imposed by the fixed condition at the blade root as well as the superimposed stresses from gas bending [36, 54, 70]. The theoretical safety factor [stress/yield stress] is only 2-3 depending on temperature. This may be a somewhat high stress state for a blade under high frequency loading, but as the blade has been modeled without the typical stress reducing taper, it is considered reasonable. While the stress distribution at all applied surface temperature conditions are similar, a slight decrease in magnitude is seen with an increase in temperature due to the corresponding decrease of the material elastic modulus.

The decrease in elastic modulus caused by rising temperatures also leads to an increase in both blade deflection and blade elongation. The blade elongation is relatively large and could be detectable by appropriate sensors. The blade deflection however, is extremely small, approximately only 15-20 µm, which may not be detectable. Removing the centrifugal load and analysing just the tip deflection compared to physical beam bending equations show that the model agrees with the beam theory in *Appendix III* (see Table 14). Deviations from theoretical values are likely due to rounding errors in calculating the average tip deflection of the model as well as a difference in the elastic modulus which was taken at the average temperature present in the model.

Table 14: Blade deflection - validation

	2D [m]	3D [m]
Model (average)	$1.88\text{x}10^{-05}$	$3.27\text{x}10^{-04}$
Physical Formula	$1.83\text{x}10^{-05}$	$3.41\text{x}10^{-04}$
Percentage Difference	2.22%	3.92%

Vibrational frequencies of the blades are lowered with increasing temperatures. This is in keeping with theory in section *3.7.2 (Vibrations)* and is the result of the decrease in elastic modulus and corresponding decrease in stiffness.

6.2 Impact of TBC Defects

A TBC defect results in a localised hot spot on the blade. This elevated substrate temperature lowers the elastic modulus of the material. As the TBC defect grows in size, the deflection is reduced until eventually it becomes negative, indicating that the deflection is against the gas pressure load. This highlights the much larger impact of the centrifugal load as compared to the gas pressure. In fact, the centrifugal loading on a turbine blade is an order of magnitude larger than the pressure loading [54]. As the TBC is removed from the pressure side of the blade, so is its corresponding mass. The radial direction for the applied centrifugal force aligns with the undamaged blade's center of mass. Thus if mass is removed from the pressure side of the blade the location of the blades center of mass will change slightly causing a larger centrifugal force on the suction side. This small mass imbalance is sufficient to create a bending moment which overpowers the opposing moment created by the pressure load. As the TBC defect increases in size the unbalanced centrifugal force also grows resulting in larger negative tip deflections. The negative deflection is reduced at increased temperatures. As the blade becomes exposed to hotter surface temperature, the resulting decrease in elastic modulus allows for greater elastic deformation on the pressure side of the blade, thus reducing the net negative deflection (Figure 11).

A small increase in blade elongation is also observed with increasing TBC defect size. However, the relative change from an undamaged blade is small; less than 0.7% for all sizes. While it is beyond the scope of this project, the high temperatures considered in this study are likely to increase the creep rate of the substrate material which would lead to much larger blade elongations as predicted here**.**

The deflection of the blade increases as the location of the TBC defect gets closer to the root of the blade. This is due to the higher stress state towards the root of the blade (Figure 26). Correspondingly this creates larger strains compared to locations closer to the tip of the blade. As expected, the blade root is clearly the most critical defect location. For these same reasons, defects located at the blade root create positive deflections (in the pressure direction away from the defect at the front side) that are sufficiently large to overcome the negative deflections created by the loss of mass. The fact that the blade deflection changes from positive to negative as the TBC defect moves from the root to the tip of the blade offers an opportunity to assess the location of potential defects during blade health monitoring.

In contrast to the relatively large percent change in tip deflection, the blade elongation is comparatively insensitive to the location of the TBC defect. This relative lack of sensitivity to both TBC defect size and location implies that the blade elongation is not a useful parameter to monitor the health of TBC coating. Extreme local temperatures due to a TBC defect however, may cause substantial creep deformation leading to larger blade elongations, particularly if the defect is close to the blade root where mechanical stresses are higher.

The change in natural frequency from a completely undamaged blade to one with no TBC coating on the pressure side is greatest for the first mode of vibration. This occurs at the highest temperature and creates a percent difference of 1.76%. The smallest change exists within the fourth mode of vibration at the coolest temperature distribution and is 0.32%. Simulation data indicate little change at cooler temperatures which can be attributed to the relatively small change in modulus of elasticity which dictates the blades natural frequency *3.7.2 (Vibrations).* Although the overall frequency change of the second mode of vibration is less than that of the first mode with a total shift of 1.1%, the second mode shows the higher change at smaller TBC defect sizes. This indicates that measuring the vibrational characteristics of the second vibrational mode may be of greater use for early detection of damage. It can be seen that the natural frequency of the blade in mode 1 decreases as the TBC defect and the ensuing local hotspot approaches the root of the blade (Figure 36). The second vibration mode is also sensitive to TBC defect location but does not change in a consistent manner. Analysing other modes of vibration for useful relationships proves similarly difficult. The change in natural frequency does not always correlate with the change in TBC defect location. For example, it can be seen that a stronger drop in natural frequency occurs in the 2nd mode at two TBC defect locations: 0.5 cm and 6 cm from the blade root. Similarly, for mode 5, minimum natural frequencies occur at 0.5 cm, 5 cm, and 8 cm from the blade root. As the natural frequency is seen to decrease as TBC defects grow in size, this implies that some modes are more sensitive to the defects at certain locations. This further implies that tracking natural frequency shifts may help monitor the health of TBC coatings and assess locations of potential defects. However, these shifts are small, often less than 1 %, which may be extremely difficult to detect reliably in an operating turbine due to vibration noises.

6.3 Impact of Cracks

The maximum stress occurs at the crack tip. The stress distribution is in good agreement with the fracture mechanics theory and is characteristic of the purely elastic material behaviour (Figure 52). The stress intensity factor or the ratio of the stress at the crack tip to the nominal stress is 3, which again complies with linear elastic calculations for a circular crack[71]:

$$k_t = 1 + 2\frac{a}{b}$$

$$k_t = 1 + 2\frac{1.5\ \text{mm}}{1.5\ \text{mm}}$$

$$k_t = 3$$

$$k_t = \frac{\sigma_{peak}}{\sigma_{nominal}}$$

Assuming purely elastic behaviour, the stress at the crack tip exceeds the yield strength for higher temperatures and deeper cracks critically located near the blade root. This shows the limitations of linear elastic fracture mechanics and the necessity of considering plastic deformation at the crack tip. This was done by using elastic-plastic data for subsequent models.

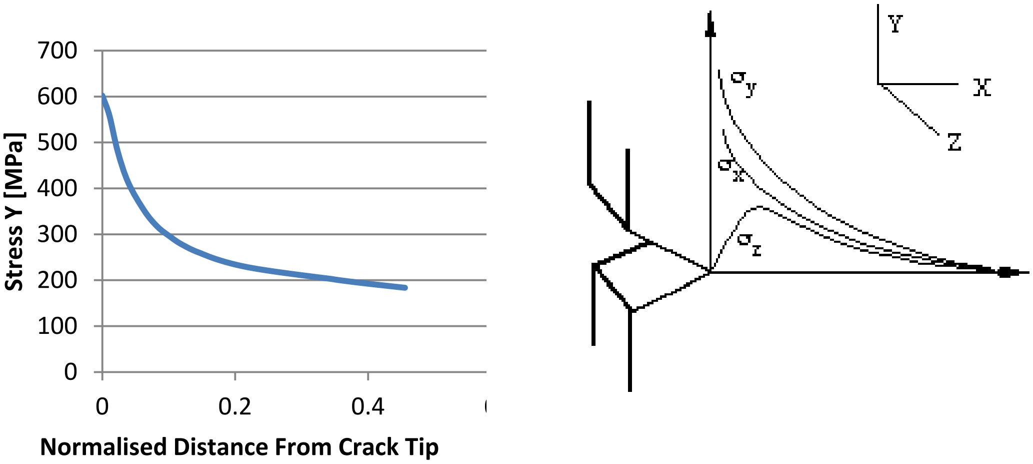

(a) (b)

Figure 52: Stress intensity factor of 3 for a half-circular crack located at 5 cm from the blade root (a); Theoretical stress distribution at a crack tip for purely elastic deformation [72] (b)

The deflection also increases as the crack is modeled closer to the blade root where the nominal stress is approximately 2x greater than at midspan. This, added to the stress concentration at the crack tip, produces local stresses in the range of 1 GPa well above the material yield strength. It can therefore be concluded that the combination of large stresses at the blade root, high stress concentration at the crack tip and high blade temperature produce very critical conditions that can lead to large blade deflections, deformation and potentially sudden blade failure.

The blade deflection increases at an accelerated rate with the crack size. The tip deflections of up to 0.3 mm, though relatively small and possibly difficult to detect by current sensors, does indicate the tip deflection to be a promising parameter for monitoring the evolution of crack damage in turbine blades. In contrast, the blade elongation is less sensitive to crack growth, although in reality creep deformation of the blade could lead to much larger elongations as compared to that estimated in our quasi-static loading case. Creep deformation could further make the effect of potential cracks on the blade elongation difficult to isolate.

The percentage change in natural frequency as a function of crack depth at midspan is summarised in Figure 53. The frequencies of all modes of vibration are reduced as the crack depth increases. Of greatest interest are mode 1 and mode 2 with the largest change of 5-17%.

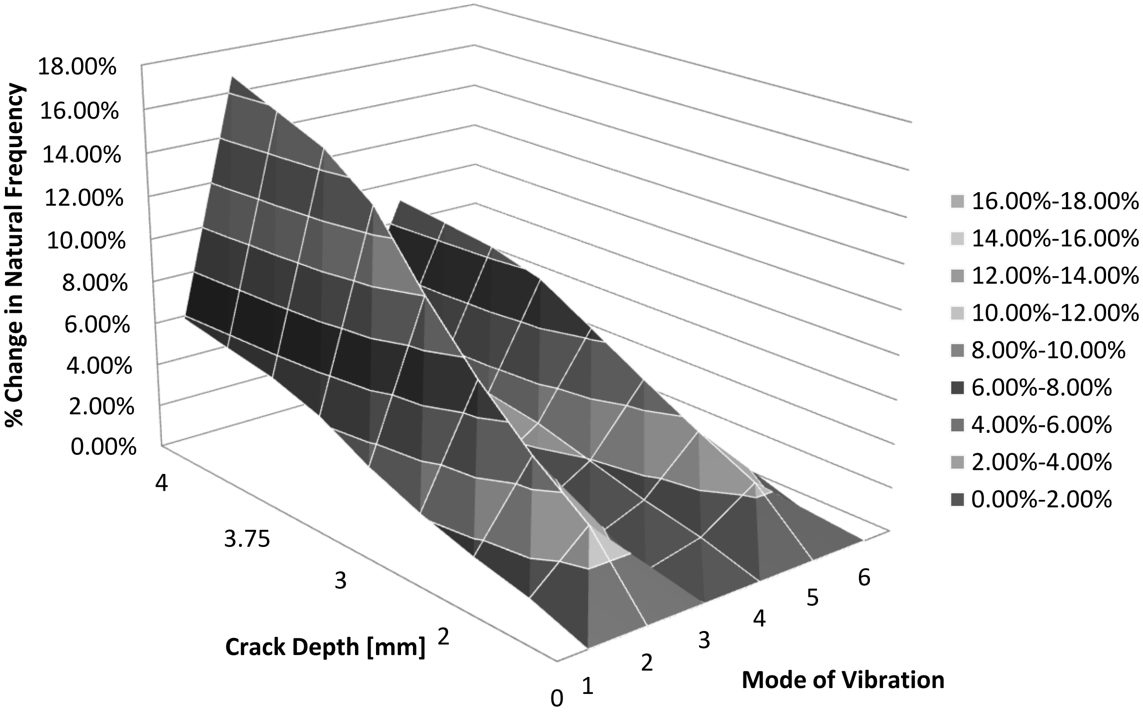

Figure 53: Natural frequency change summary at mid-span

The location of the crack has a similar effect on the natural frequency as the crack depth at mode 1. The natural frequency decreases as the crack is moved closer to blade root. However other modes exhibit only occasional strong drops depending on crack location. While all modes exhibit a change in natural frequency with crack depth, the magnitude of this shift is dependent on crack location. The modes at which the peaks and valleys of Figure 53 occur would change depending on the crack location. This sensitivity is likely caused when cracks are located at critical areas of mode shapes, specifically at nodes and anti-nodes.

The excitation of a turbine blade is largely due to the cyclic variation of gas moving across the blade’s surface. This occurs at frequencies equal to the rate at which turbine blades pass behind the guide vanes. The turbine stage has 74 blades [57] and rotates at 1500 rad/s (238 rev/s). The excitation frequency can then be assumed to be 238x74 = 16950 Hz. All extracted natural frequencies do not approach this value, the closest occurring at mode 5. As the crack progresses, the natural frequency of mode 5 decreases by approximately 1800 [Hz] to 18440 Hz, a shift of 10%. This may indicate that crack growth into the blade would not change the natural frequency sufficiently to cause any resonance vibration of the blade. However, additional and more exact information about the operation of the turbine is needed as well as other possible excitation frequencies to fully comment on this possibility.

6.4 Model Improvement Through Consideration of the Material Plasticity

Plastic data was neglected initially from models, because the focus of the work is to detect the onset of damage while the turbine blade is still able to operate safely and thus no substantial plastic deformation can be expected. The analysis of the results based on purely elastic material behaviour shows that this assumption has some substantial flaws. In fact, localised yielding occurs at larger crack depths, critical locations close to the blade root, and higher surface temperature under normal application conditions. Superalloys are quite tough and may be able to operate for considerable service duration with such damage. Thus, modelling was also conducted using elastic-plastic material data. The results remained practically identical to those of purely elastic models for the blades with no crack damage due to the lower stress level below the material yield strength.

As can be seen in Figure 54 including material plasticity leads to reduced stress concentration and reduction in local stress at the crack tip since plastic deformation leads to broader load distribution within the material. Correspondingly, the overall strain increases as the material yields and flows above the yield strength, particularly at temperatures above 1000 K where the material strength drops strongly with increasing temperature. At such temperature, thermally activated processes such as creep and diffusion dominate, reducing the material resistance to deformation and increasing its ductility.

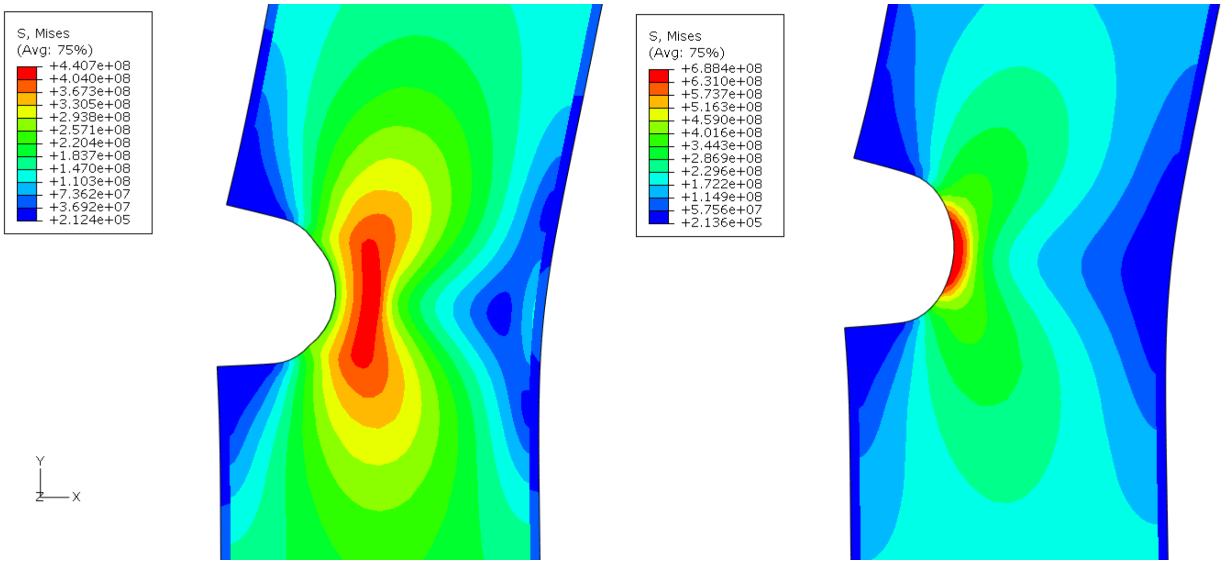

(a) **(b)**

Figure 54: Stress distribution at 1155 K (a) and 955 K (b) as determined using elastic-plastic material behaviour

The stress increases towards the crack tip and then drops immediately ahead of the crack tip where the highest plastic strains occur. This agrees very well with theoretical stress distributions as shown in Figure 55.

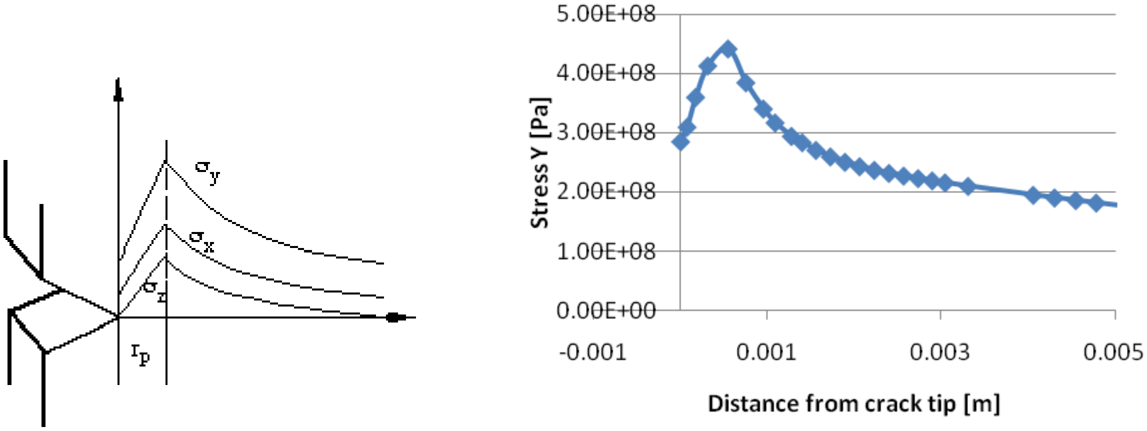

(a) (b)

Figure 55: Theoretical stress distribution (a) and stress distribution as simulated for a 1.5 mm deep crack located at 5 cm from the blade root

For a crack depth less than 3 mm located at midspan, the magnitude and rate of change of deflection are similar to the results from purely elastic models. For crack depths of 3 mm or more and temperatures above the transition temperature, the deflection deviates from the results under purely elastic consideration and the deviation increases with temperature. Mesh deformation, stress and strain distributions clearly show that the change in deflection are the result of localised deformation around the crack tip. The deflection of the blade appears analog to that of a system made of two beams connected by a torsional spring as described in [44] and [73]. The localised decrease in stiffness and the plastic deformation are the main causes of increased deflection. At crack depths larger than 4 mm at mid-span or 3.5 mm near the blade root, the blade deflection increase exponentially and *Abaqus* is unable to calculate a solution because of extremely large deformation within the model indicating potential blade fracture.

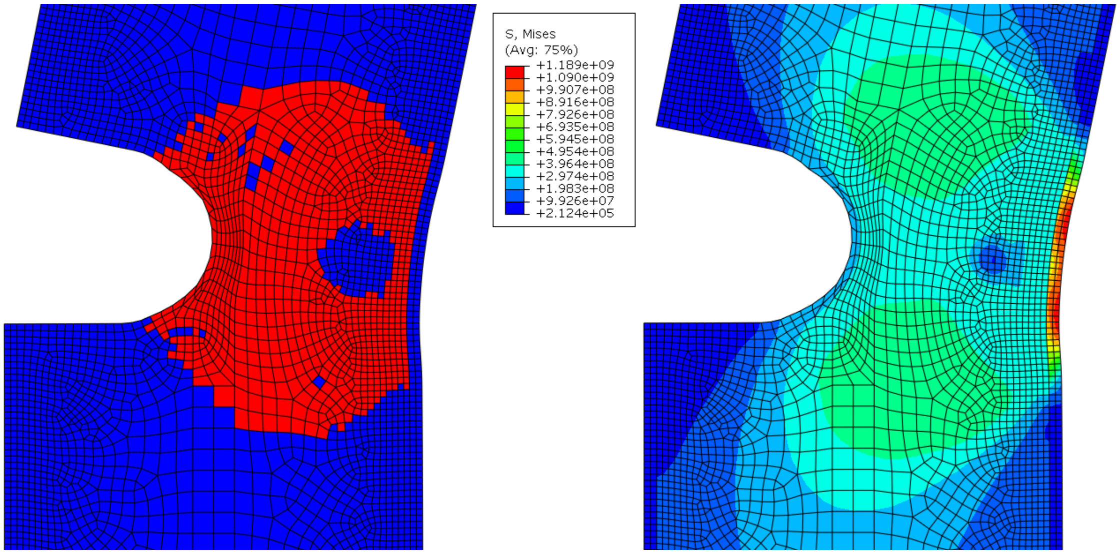

Figure 56: Elements around the crack tip with active yielding (left), and stress distribution at 1155 K

At crack depths just below the critical crack depths for fracture, for example 3.85 mm at midspan or 3.25 mm at 0.5 cm from the blade root (location of peak deflection), the tip-deflection is 1.3 and 2.5 mm respectively. This is a substantial change several orders of magnitude ($>10^3$) larger than the deflection of an undamaged blade. Such large deflections are detectable suggesting that the blade tip deflection may be a reliable parameter for crack detection and health monitoring. However, it is questionable whether detecting a crack of this size provides sufficient time for corrective measures to be taken, or whether such deep cracks have already exceeded the permissible crack size and thus the blade would have already been replaced or may have already failed. In fact, a crack of 2 mm at midspan (half of the critical value) only causes a deflection of 0.1 mm. At the root of the blade a crack of 2 mm crack produces a deflection of 0.38 mm and at a crack length of 1.75 mm (half the length of the critical crack length) produces a deflection of 0.289 mm. These values are at the lower limit of current sensors resolution and thus the early onset of such damage would remain undetected. A simultaneous increase of both blade elongation and deflection would probably be a stronger indicator of near critical blade damage. Still, it is difficult to conclude at this point whether the changes modelled here can reliably be detected using available sensors since the blade excitation and the loading conditions can statistically vary over time producing noise at comparable levels. Therefore, future work could concentrate on assessing vibration noise level in turbine in order to determine allowable blade deflection and elongation ranges beyond which warning could be given for excessive accumulated damage from deformation, cracks, TBC failure and the need for checks, maintenance or corrective measures.

The maximum deflection occurs when the crack is located at 5 mm from the root of the blade. This is the closest a crack with a complete circular tip can be to the blade root (Figure 57) while keeping the entire plastic zone bounded by the model. For cracks with distance to the blade root smaller than 5 mm, the plastic zone within the model becomes smaller, leading to reduced blade deflection. It is currently unknown if this effect would be confirmed in real application, but it can be effectively compared to the case of a shorter sample exhibiting a smaller elongation than longer samples at equivalent or even higher strains. It can still be expected that cracks at distances smaller than 5 mm from the blade root could be more critical regarding fracture as the local nominal stress is expected to further increase towards the blade root.

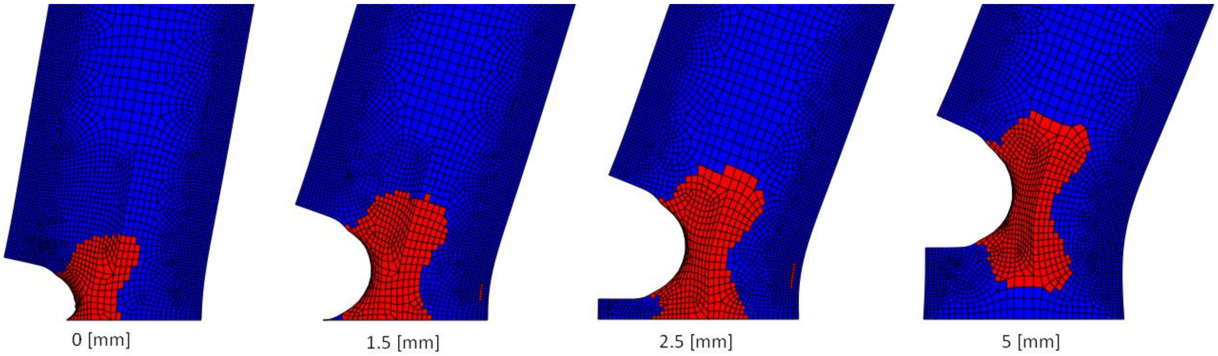

Figure 57: Active plastic yielding zone for a 3 mm crack near the blade root

The plastic yielding zone (Figure 57) follows the elastic-plastic crack theory. The theoretical deformation around the crack tip is illustrated in Figure 58; note similarities in the half-zone shape for the plane strain assumption.

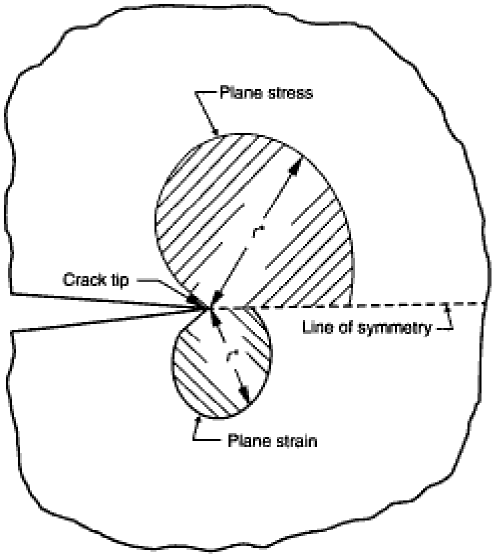

Figure 58: Comparison of plastic zone sizes for plane stress and plain strain assumptions [74]

6.5 Three-Dimensional Models

Overall, the three-dimensional models yield results similar to those of two-dimensional models but currently lack the entire range of damage progression. As a crack grows into the blade, the effective stiffness is reduced resulting in larger tip deflections. Moving the crack location towards the root of the blade leads to identical blade deflection trends as established using two-dimensional models; as the crack moves towards the root of the blade, the tip-deflection shows a corresponding increase.

However, the overall changes in deflection values are considerably smaller than two-dimensional models. This significant difference is largely due to the difference in blade geometry (span and thickness) as well as the difference in crack geometry. The 2-D plain-strain assumption models a crack of uniform depth along the entire width of the blade. In the case of the three-dimensional model however, the crack depth had to be changed along the width because of varying thickness and the knowledge that blade damage would most likely start from the leading edge of the blade (see Figure 59). Due to these geometry limitations and specificities of real three-dimensional blades, it seems likely that cracks causing detectable changes in blade deflection and elongation as currently modeled would be considerably more difficult.

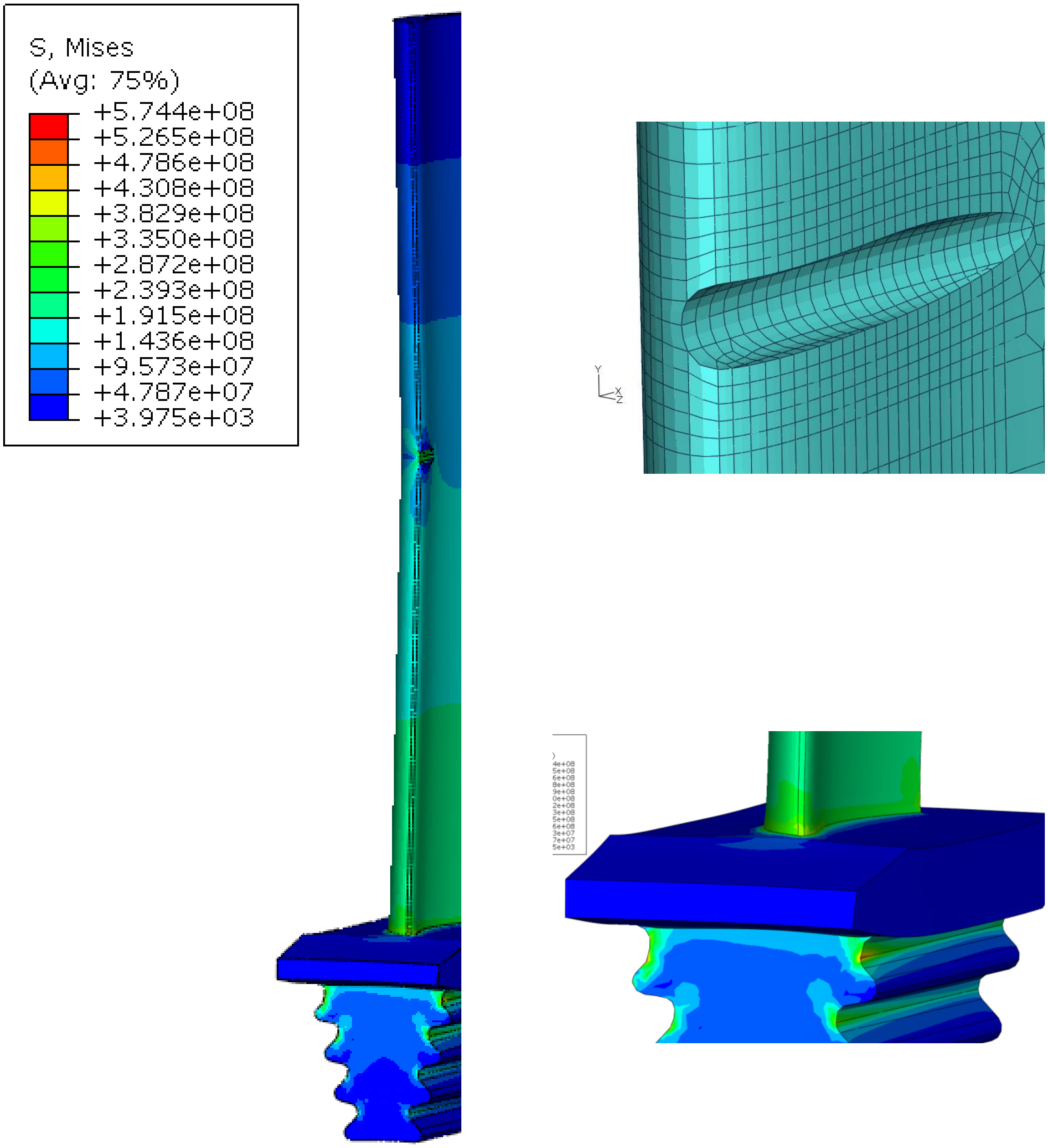

Figure 59: Stress distribution in 3-D blade with a crack under elastic-plastic material behaviour

7 Conclusion

TBC defects affect the mechanical response of turbine blades during operation. The lack of TBC in a localised area creates a hotspot on the substrate changing the mechanical properties of the substrate, particularly the elastic modulus and the yield strength, which both decrease with temperature. The reduced elastic modulus increases the flexibility of the blade, decreasing the natural frequency and increasing the blade deflection. However, the changes are relatively small and may be impossible to measure using current sensors, particularly when considering potential vibration noise of the blade during engine operation. In addition, the dramatic collapse in chemical and corrosion resistance of the blade material potentially following TBC failure [75] is not reflected in our study nor is creep. Crack damages also affect the tip deflection of the blade. As crack damage progresses, the tip deflection increases nearly proportionally, which can be useful for both diagnostic and prognostic monitoring of blades. At larger crack depths the tip deflection rises above the lower limit of detectable deflections using currently available sensors (0.25-0.5 mm) [29]. Cracks also lower the natural frequency of the blade and at greater crack depths this change can be significant (10-14%). It is unlikely that such shifts would bring a blade dangerously close to a resonance frequency. The largest shifts occur at the first two modes of vibration although higher modes exhibit sensitivity to the location of the crack. Limitations to the elastic model were found; when the cracks are modeled at greater depths, or at the blade root, the stress at the crack tip exceeds the yield stress of the material. Assuming purely elastic behaviour has the effect of reducing the actual deflection the blade would experience. Much larger deflections are found when the more realistic elastic-plastic material behaviour is considered

The elastic-plastic material behaviour assumption yields deflections similar to those obtained using the purely elastic models at lower temperatures. However at higher temperatures, plastic strains occur at greater crack depths and locations close to the blade root leading to stronger deflection as compared to results from purely elastic simulations. Simulations using elastic-plastic data suggest blade fracture for crack depths larger than 4 mm at midspan or 3.5 mm at the blade root.

Three-dimensional models support the findings of the two-dimensional models, as a crack grows into the blade, the tip deflection increases at an accelerated rate. The consideration of plastic deformation leads to larger changes in deflection with increasing crack depth particularly at high temperature. While the tip deflection is larger in the three-dimensional models, the overall change in behaviour from that of an undamaged blade remains smaller. Similar to two-dimensional models, the blade elongation is relatively unaffected by crack damage. The natural frequencies of the three dimensional models are also reduced with the introduction and progression of crack damage but the shifts are extremely small at all modes of vibration.

Overall, TBC-defects cause only small changes in deflection and natural frequency. It is unlikely that localised TBC spallation would be immediately detectable by monitoring the mechanical behaviour of an operating blade. Two-Dimensional and three-dimensional models indicate that crack damage can cause changes in the mechanical behaviour of blades, especially when plastic data are included in the analysis. These changes are large enough to make detection during operation a possibility. As new advances in sensor technology emerge and resolution increases, tracking the entire evolution of accumulated damage may become possible.

8 Outlook

The use of simplified geometry and loading conditions is sufficient to observe trends and obtain approximate magnitudes in deflection and vibration, but it is impossible to comment on the actual magnitude of the response for a specific turbine blade within a specific engine. Two-dimensional models cannot fully describe the complex response of actual turbine blades, and three-dimensional models employed in an effort to emulate general characteristics may deviate too far from real blades. Accurate numerical modeling of three dimensional blades often requires a coupled fluid/heat transfer analysis. Assuming an accurate solution from this analysis, the resulting reaction forces from fluid flow across the blade surface can be used to model the bending forces acting upon the blade realistically while the convective heat transfer solution provides an accurate surface temperature for the blade. Consideration of a more realistic geometry could allow modelling of tapered turbine blades.

Dynamic and transient loading conditions have not been considered in this study. By including the dynamic loading, the exact response of the blade can be studied and any relationship with crack size, particularly changes in amplitude and frequency, can be established. By including transient engine conditions, non-stationary critical operating conditions could be established. For example, the blades may pass through resonance frequencies during start-ups, shut-downs, acceleration, or deceleration phases increasing the load, the deformation and the deflection of the blade.

Cracks with a circular tip have been used to model crack damage in the present models, but these are not the typical crack shapes occurring in turbine blades. With proper element control to prevent singularity at the crack tip, seam or sharp cracks with high stress concentration factors could be used to represent a more realistic fatigue crack and may even be easier to model parametrically with proper re-meshing controls. Making use of advanced mesh refinement techniques, specifically around the crack tip, may increase the accuracy and reduce the processing time of crafted models.

If two dimensional models continue to be used, memory demands would be sufficiently low to allow crack growth simulation. Incorporating fracture mechanics would allow correlating sensor reading with simulated crack growth which would assist in recognising changes related to blade damages. Also, this could allow estimating the remaining life of the blade in addition to just recognising the existence of cracks, thereby increasing the potential of monitoring and warning. Suggestions such as immediate engine shut-down or emergency landing at nearest or destination airport would be possible depending on estimated remaining blade life and actual monitoring result.

This study finds the effect of TBC defects on the mechanical behaviour of turbine blades to be negligible. This is contrary to reality as turbine blades are known to often fail shortly after TBC spallation. A reasonable heat distribution has been created, but the cross-section of the model is greatly simplified. In reality, cooled turbine blades typically contain multiple cooling channels creating in some cases a nearly hollow structure. The effect of localised heating maybe considerably more pronounced if applied to a three–dimensional model where the structural thickness of the wall is thinner. Modeling a three dimensional structure, including realistic internal cooling channels, would allow this to be investigated. Additionally, this study only considers the immediate effects experienced by the loss of a TBC but no secondary effects. By including creep, oxidation, corrosion, and time dependent temperature degradations, the evolving behaviour of a turbine blade after TBC spallation can be studied.

Accurate modeling for the purpose of an operational diagnostic/prognostic system requires detailed material data, operational data, and exact geometries. As such, information is largely proprietary which requires cooperation with engine manufactures. Additionally, any modeling work completed must be validated and refined with empirical testing. Any measurable parameters used for diagnostics and prognostics for structural health must be proven to be measurable above the noise of an operational engine. This requires the use of test rigs and eventual field data.

References

[1] E. L. Suarez, M. J. Duffy, R. N. Gamache, R. Morris, A. J. Hess, "Jet engine life prediction systems integrated with prognostics health management", presented at *Aerospace Conference, 2004. Proceedings. 2004 IEEE*, **2004**.

[2] A. D. Boyd-Lee, G. F. Harrison, M. B. Henderson, *International Journal of Fatigue* **2001**, *23*, 11.

[3] M. J. Roemer, G. J. Kacprzynski, "Advanced diagnostics and prognostics for gas turbine engine risk assessment", presented at *Aerospace Conference Proceedings, 2000 IEEE*, **2000**.

[4] S. Ogaji, R. Singh, *Computational Intelligence in Fault Diagnosis* **2006**, 179.

[5] N. A. Kumar A, El-Masri R, Wieslaw Beres, Xijia Wu, Prakash C. Patnaik,, in *IEEE 2007 Canadian Conference on Electrical and Computer Engineering*, Vancouver **2007**, 4.

[6] M. J. Roemer, E. O. Nwadiogbu, G. Bloor, "Development of diagnostic and prognostic technologies for aerospace health management applications", presented at *Aerospace Conference, 2001, IEEE Proceedings.*, **2001**.

[7] A. Mathur, aQualtech Systems, Inc., Wethersfield **2002**.

[8] R. I. Stephens, H. O. Fuchs, *Metal fatigue in engineering*, Wiley, **2001**.

[9] D. Broek, *The practical use of fracture mechanics*, Kluwer Academic Publishers, **1989**.

[10] J. P. Gallagher, Giessler, F.J., Berens, A.P., Engle, Jr.,, H. A. R.M. and Wood, **1984**.

[11] T.L. Anderson, *Fracture Mechanics Fundamentals and Applications*, Taylor & Francis, **2005**.

[12] T. J. Carter, *Engineering Failure Analysis* **2005**, *12*, 237.

[13] N. X. Hou, Z. X. Wen, Q. M. Yu, Z. F. Yue, *International Journal of Fatigue* **2007**, *In Press, Corrected Proof*.

[14] E. E. Gdoutos, *Fracture mechanics: an introduction*, Springer, **2005**.

[15] N. Eliaz, G. Shemesh, R. M. Latanision, *Engineering Failure Analysis* **2002**, *9*, 31.

[16] R. G. Wellman, J. R. Nicholls, *Tribology International* **2008**, *41*, 657.

[17] D. H. LeMieux, U.S Department of Energy National Energy Technology Laboratory, Pittsburgh **2003**.

[18] N. P. Padture, M. Gell, E. H. Jordan, *Science* **2002**, *296*, 280(5).

[19] Z. Xu, L. He, R. Mu, X. Zhong, X. Cao, *Vacuum* **2008**, *82*, 1251.

[20] V. K. Tolpygo, D. R. Clarke, K. S. Murphy, *Surface and Coatings Technology* **2001**, *146-147*, 124.

[21] R. Miller, *Journal of Thermal Spray Technology* **1997**, *6*, 35.

[22] D. R. Mumm, A. G. Evans, *Acta Materialia* **2000**, *48*, 1815.

[23] A. G. Evans, D. R. Mumm, J. W. Hutchinson, G. H. Meier, F. S. Pettit, *Progress in Materials Science* **2001**, *46*, 505.

[24] K. W. Schlichting, N. P. Padture, E. H. Jordan, M. Gell, *Materials Science and Engineering A* **2003**, *342*, 120.

[25] E. Schumann, C. Sarioglu, J. R. Blachere, F. S. Pettit, G. H. Meier, *Oxidation of Metals* **2000**, *53*, 259.

[26] T. Xu, S. Faulhaber, C. Mercer, M. Maloney, A. Evans, *Acta Materialia* **2004**, *52*, 1439.

[27] X.-Y. Gong, D. R. Clarke, *Oxidation of Metals* **1998**, *50*, 355.

[28] S. G. DL Simon, GW Hunter, T Guo, KJ Semega, "Sensor Needs for Control and Health Management of Intelligent Aircraft Engines", presented at *ASME Turbo Expo*, **2004**.

[29] A. von Flotow, M. Mercadal, P. Tappert, "Health monitoring and prognostics of blades and disks with blade tip sensors", presented at *Aerospace Conference Proceedings, 2000 IEEE*, 2000, **2000**.

[30] M. Dowell, G. Sylvester, "Turbomachinery prognostics and health management via eddy current sensing: current developments", presented at *Aerospace Conference, 1999. Proceedings. 1999 IEEE*, 1999, **1999**.

[31] L. PRECISION, Vol. 2011, **2010**.

[32] M. Drumm, W. C. Hause, "High performance rotor monitoring", presented at *Digital Avionics Systems Conferences, 2000. Proceedings. DASC. The 19th*, 2000, **2000**.

[33] T. Fabian, F. B. Prinz, G. Brasseur, *Instrumentation and Measurement, IEEE Transactions on* **2005**, *54*, 1133.

[34] M. Bartsch, B. Baufeld, S. Dalkiliç, L. Chernova, M. Heinzelmann, *International Journal of Fatigue* **2008**, *30*, 211.

[35] J. Gutleber, J. Brogan, R. J. Gambino, C. Gouldstone, R. Greenlaw, S. Sampath, J. Longtin, Z. Dongming, "Embedded temperature and heat flux sensors for advanced health monitoring of turbine engine components", presented at *Aerospace Conference, 2006 IEEE*, 0-0 0, **2006**.

[36] J. M. Gere, *Mechanics of materials*, Brooks/Cole, **2004**.

[37] J. Hou, B. J. Wicks, R. A. Antoniou, *Engineering Failure Analysis* **2002**, *9*, 201.

[38] D. Afolabi, *Journal of Sound and Vibration* **1988**, *122*, 535.

[39] B. O. Al-Bedoor, *The Shock and Vibration Digest* **2002**, *34* 455

[40] L. G. Al-Bedoor B.O., S.A. Adewusi, Y. Al-Nassar, M. Abdlsamad, *Journal of Quality in Maintenance Engineering* **2003**, *9*, 144

[41] B. O. Al-Bedoor, S. Aedwesi, Y. Al-Nassar, *Journal of Quality in Maintenance Engineering* **2006**, *12*, 275.

[42] A. Roitman, A. Pylov, N. Aleksandrova, *Strength of Materials* **1999**, *31*, 486.

[43] K. P. Maynard, "On the Feasibility of Blade Crack Detection Through Torsional Vibration Measurements", presented at *Proceedings of the 53rd Meeting of the Society for Machinery Failure Prevention*

Technology,, **1999**.

[44] W. M. Ostachowicz, M. Krawczuk, *Journal of Sound and Vibration* **1991**, *150*, 191.

[45] S. W. D. D. A. N. Charles R. Farrar, *Philosophical Transactions of the Royal Society A: Mathematical, Physical and Engineering Sciences* **2001**, *359*, 131.

[46] M. Sunar, B. O. Al-Bedoor, *Shock and Vibration* **2008**, *15*.

[47] A. D. Dimarogonas, *Engineering Fracture Mechanics* **1996**, *55*, 831.

[48] S. Kumar, N. Roy, R. Ganguli, *Mechanical Systems and Signal Processing* **2007**, *21*, 480.

[49] W. J. Palm, *Mechanical vibration*, John Wiley, **2007**.

[50] B. Huang, J. Kuang, *Proceedings of the Institution of Mechanical Engineers, Part C: Journal of Mechanical Engineering Science* **2001**, *216*, 447.

[51] D. Afolabi, *Journal of Sound and Vibration* **1988**, *122*, 535.

[52] M. American Society for, *Metals handbook volume 1: Properties and selection : Irons and steels*, American Society for Metals, **1978**.

[53] J. R. Davis, A. S. M. I. H. Committee, *Heat-resistant materials*, ASM International, **1997**.

[54] H. I. H. Saravanamuttoo, G. F. C. Rogers, H. Cohen, *Gas turbine theory*, Prentice Hall, **2009**.

[55] ABAQUS, *Abaqus/CAE User's Manual*, Dassault Systèmes, **2007**.

[56] A. INC, Dassault Systèmes, **2007**.

[57] *Large PW100 Series Training Manual*, Pratt & Whitney Canada, **2000**.

[58] D. P. K. E. Hosking, R. I. McCormick, P. S. S. H. Moustapha, A. A. Smailys, in *Presented at the RTO AVT Symposium on "Design Principles and Methods for Aircraft Gas Turbine Engines"*, RTO MP-8, Toulouse France **1998**.

[59] O. Majeed, in *17th Canadian Aeronautics and Space Institute Propulsion Symposium* Kanata, Ontario, Canada **2009**.

[60] J. W. Sawyer, *Sawyer's Gas Turbine Engineering Handbook*, Business Journals, **1993**.

[61] J. M. Gere, S. P. Timoshenko, *Mechanics of materials*, PWS Pub Co., **1997**.

[62] L. Li, Z. Lu, J. Wang, Z. Yue, *Computer-Aided Design* **2007**, *39*, 494.

[63] G. C. Giovanni Cerri, Giovanni Cerri, Giovanni Cerri, *International Journal of Gas Turbine, Propulsion and Power Systems* **2008**, *2*.

[64] M. J. Donachie, S. J. Donachie, *Superalloys: a technical guide*, ASM International, **2002**.

[65] SpecialMetals, Vol. 2010, Special Metals Corporation,, **2004**.

[66] R. A. Smith, Y. Liu, L. Grabowski, *Fatigue & Fracture of Engineering Materials & Structures* **1996**, *19*, 1505.

[67] HAYNES_International, Vol. 2010, HAYNES International, **2008**.

[68] ATI_Allvac, Vol. 2010, **2009**.

[69] M. Götting, J. Rösler, *Computers & Structures* **2007**, *85*, 225.

[70] E. P. Popov, T. A. Balan, *Engineering mechanics of solids*, Prentice Hall, **1998**.

[71] H. P. Rossmanith, *Teaching and education in fracture and fatigue*, E & FN Spon, **1996**.

[72] P. Rusmee, Vol. 2011, **1998-2005**.

[73] S. P. Lele, S. K. Maiti, *Journal of Sound and Vibration* **2002**, *257*, 559.

[74] A. F. Liu, *Mechanics and mechanisms of fracture: an introduction*, ASM International, **2005**.

[75] S. Bose, J. DeMasi-Marcin, *Journal of Thermal Spray Technology* **1997**, *6*, 99.

[76] SRS, Specific Range Solutions Ltd., **2009**.

[77] H. I. H. Saravanamuttoo, *Progress in Aerospace Sciences* **1987**, *24*, 225.

[78] J. H. Horlock, *Axial flow turbines: fluid mechanics and themodynamics*, Butterworths, London **1966**.

[79] C. Saravanamuttoo, *Gas Turbine Theory*, **1972**.

[80] F. P. Incropera, D. P. Dewitt, T. L. Bergman, A. S. Lavine, *Fundamentals of Heat and Mass Transfer*, John Wiley & Sons Inc.

Appendix I. Reverse Analysis on PW-100 Turboprop

AI.1 Introduction

This section details a brief stress analysis on the 2nd stage of the Pratt & Whitney Canada PW-100 turbo prop engine from known operational data and several cross-sections compiled from [57-59, 76, 77]. During this analysis, (1) the second stage of the power turbine is “reverse engineered", and (2) the stress distribution in both the blades and disk is estimated analytically.

AI.2 Known Data

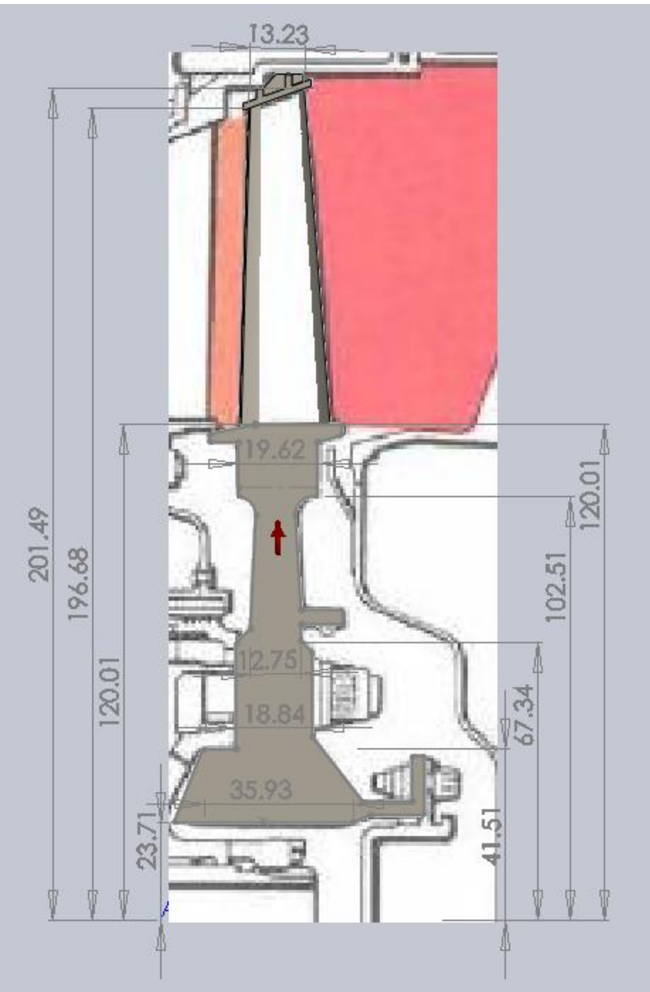

Figure 60: Blade and disk dimensions

From the know geometric data of the entire engine are: Length 2134 mm, Width 660 mm, Height 838 mm, the cross-section can be scaled using drafting software (see Figure 64) and then detailed information on the second stage blades and disk can be obtained and recreated from the scaled drawing.

Other known data:

- The gear ratio form the power turbine to the propeller is 15.4:1 to 17.2:1
- Take-Off Rating (Maximum): 2100 eshp, 2000 shp at 1200 propeller rpm
- Take-Off Rating (Normal): 1892 eshp, 1800 shp at 1200 propeller rpm
- Maximum Cruise: 1738 esph, 1651 shp at 1200 propeller rpm
- Normal Cruise: 1105 shp + 34 lb thrust (25,000 ft, 350 mph, 85% power turbine rpm)
- Blades and disk are manufactured from Waspaloy forgings of IN713LC casting.

Converting power and RPM:

$$\begin{aligned} &P_{\max} = 1565\ kW \\ &P_{\max(typical)} = 1410\ kW && \omega_{@1200} = 2161\ {}^{rad}\!/_{s} \\ &\underbrace{P_{\max(cruise)} = 1296\ kW}_{@1200\ rpm} && \omega_{@1320} = 2378\ {}^{rad}\!/_{s} \\ & && \omega_{@1440} = 2594\ {}^{rad}\!/_{s} \\ &\underbrace{P_{(crusie)} = 850\ kW}_{@85\%\ 1020\ rpm} && \omega_{@cruise} = 1837\ {}^{rad}\!/_{s} \end{aligned}$$

The temperatures at various engine stages are also know along with the pressure ratios. They are displayed graphically in Figure 61.

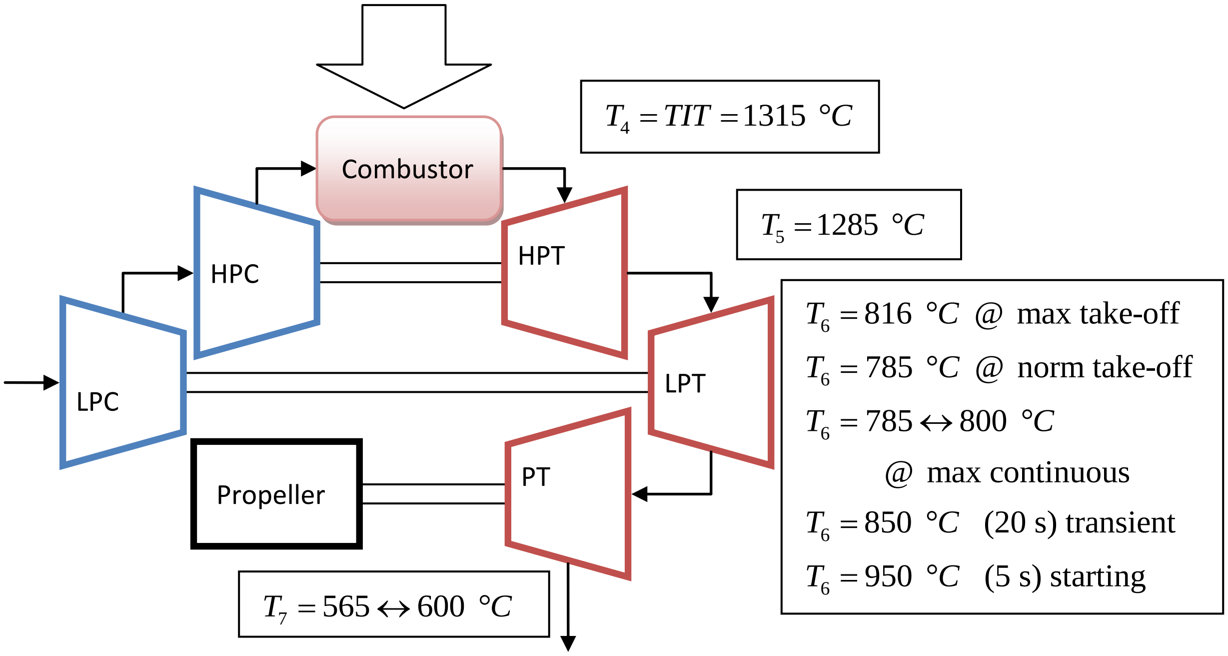

Figure 61: Thermodynamic cycle

AI.3 Calculations

Thermodynamic Analysis

Referring to Figure 61 and assuming a simple ideal cycle:

Isentropic compression and expansion

1) $\Delta KE = 0$
2) No pressure losses
3) Perfect gas (air) constant specific heat
4) Constant mass flow
5) Heat transfer in heat exchanger complete

The net work available for the prop from the power turbine is given by

$$\begin{aligned} W_{prop} &= W_{PT} \\ \dot{W}_{prop} &= \dot{m}C_P \;\; T_6 - T_7 \\ \therefore \dot{m} &= \frac{\dot{W}_{prop}}{C_P \;\; T_6 - T_7} \end{aligned} \tag{0.3}$$

Substituting values for T_6 and T_7 and taking the specific heat of the combusted gas as $C_P \approx 1.171\left[{}^{kJ}\!/\!{}_{kg\cdot K}\right]$ it is possible to determine the gas mass flow rate. By inspection it is clear that larger mass flows are required for smaller temperatures across the turbine thus it will be assumed that the gas exhaust temperature is the highest possible; $T_7 = 873\ \mathrm{K}$. For normal cruise conditions it is assumed that the inlet temperature is slightly lower ($T_6 = 750°C$). Using equation (0.3) and the known output shaft powers the required mass flows can be tabulated and shown in Table 15.

Table 15: Mass flow required power

Operating Condition	$T_6 \quad °K$	$\Delta T \quad °K$	$\dot{W}_{prop} \quad kW$	$\dot{m}\ \left[{}^{kg}\!/\!{}_{s}\right]$
max-take off	1089	216	1565.97	6.769
norm take-off	1058	185	1410.864	7.121
max continuous	1073	200	1296.027	6.051
Norm Continuous	1023	200	850	5.152

Gas Velocity

Some reasonable assumptions must be made about the nature of this 2 stage design. As the last stage exhausts to atmosphere (through a final set of guide vanes/diffuser) it would be reasonable to assume that absolute velocity of this gas is purely axial, especially as at cruise operating conditions this gas is responsible for producing a small amount of thrust (35lb). For design simplicity multiple turbine stages are often designed with the same profile and velocity triangles, it can reasonably be assumed that this is the case here. A simple mean line analysis which was used to calculate the blade stresses is shown here.

The work in terms of the rotor gas angle [78]:

$$W_S = UC_a \ \ \tan\beta_2 + \tan\beta_3 \qquad (0.4)$$

Where the blade speed at mid-span is known from:

$$\begin{aligned} &U = H_m\omega \\ &\text{for normal cruise} = 290 \ {}^{m}\!/_{s} \ \ \text{and at } 1200 \ \ rpm \ \text{(prop)} = 340 \ {}^{m}\!/_{s} \end{aligned} \qquad (0.5)$$

Referring to Figure 60 the outer radius of the annulus area can clearly be seen to vary axially in a linear relationship. At the exit from the 2nd stage the annulus has an area of $A = 0.0807 \ \ m$.

Referring to Figure 60 the outlet exhaust path maintains a constant area implying that little expansion or compression of exhaust gases occurs (from continuity), thus it is reasonable to assume that the pressure at the exit from the power turbine is close to atmospheric. Rearranging the perfect gas law assuming operation conditions at both sea level (take-off) and cruise altitude (25 000 ft) the density can be determined: $\rho_{exit(TO)} = 0.3991\left[{}^{kg}\!/_{m^2}\right]\rho_{exit(cruise)} = 0.2394\left[{}^{kg}\!/_{m^2}\right]$ (0.6)

From continuity the axial velocity of the gas can be determined:

$$C_a = \frac{m}{A\rho} \qquad (0.7)$$

Substituting (0.6) into (0.7) the axial speed can be determined, the results for a range of mass flows are displayed in Figure 63. The axial velocity from which to re-construct the velocity triangles can then be chosen as $225\ {}^{m}\!/_{s}$.

To ensure efficient aerodynamic design it would be reasonable to assume that the gas angles and blade profile would be designed to operate primarily at cruise conditions. Assuming the leaving velocity from the turbine to be purely axial ($\alpha_3 = 0$) the velocity triangle can be solved:

$$\frac{U_m}{C_a} = \frac{290}{225} = \tan\beta_3 - \tan\ 0 \ \rightarrow \angle\beta_3 = 52° \qquad (0.8)$$

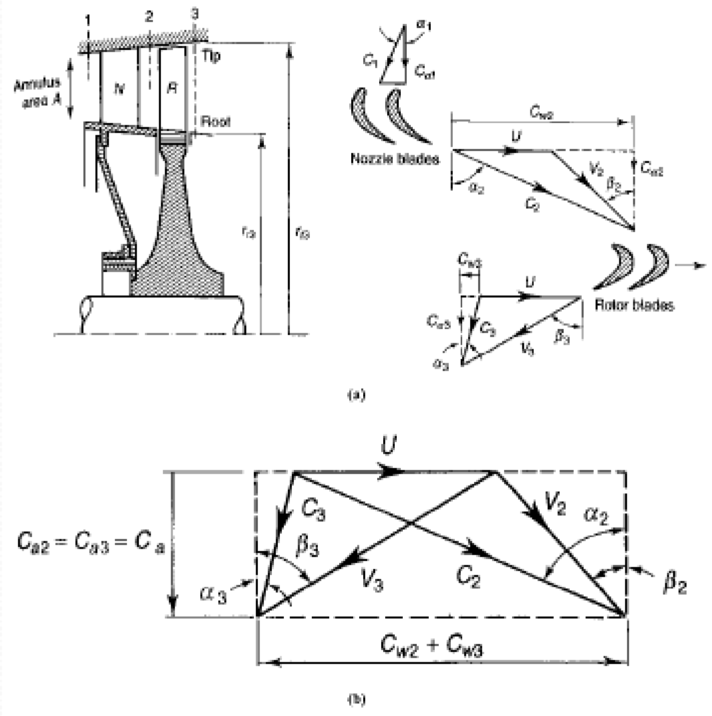

Figure 16: (a) Axial flow turbine stage (b) velocity diagram [Saravanamuttoo]

Figure 62: (a) Axial flow turbine stage, (b) velocity triangles [79]

From Figure 63 the geometry gives:

$$[78]\ \frac{U}{C_A} = \tan\alpha_2 - \tan\beta_2 = \tan\beta_3 - \tan\alpha_3 \qquad (0.9)$$

And applying principle of angular momentum the work done by the stage is:

$$W_S = U \;\; C_{w2} + C_{w3} \;\; = UC_{a2} \;\; \tan\alpha_2 + \tan\alpha_3 \qquad (0.10)$$

Combining with (0.9) the work in terms of the rotor gas angle is:

$$W_S = UC_a \;\; \tan\beta_2 + \tan\beta_3 \qquad (0.11)$$

Where the blade speed at mid-span is known from:

$$\begin{aligned} &U = H_m\omega \\ &\text{for normal cruise} = 290 \ {}^{m}\!/_{s} \\ &\text{at } 1200 \ \ rpm \ \text{(prop)} = 340 \ {}^{m}\!/_{s} \\ &\text{at } 1320 \ \ rpm \ \text{(prop)} = 375 \ {}^{m}\!/_{s} \\ &\text{at } 1320 \ \ rpm \ \text{(prop)} = 375 \ {}^{m}\!/_{s} \\ &\text{at } 1420 \ \ rpm \ \text{(prop)} = 410 \ {}^{m}\!/_{s} \end{aligned} \qquad (0.12)$$

Referring to Figure 60the outer radius of the annulus area can clearly be seen to vary axially in a linear relationship. At the exit from the 2nd stage the annulus has an area of

$$\begin{aligned} A = & \;\; H_6{}^2 - H_{hub}{}^2 \;\; \pi \\ & = \;\; 201 \ mm \;\; {}^2 - 121 \ mm \;\; {}^2 \;\; \pi \\ & = 0.0807 \ \ m \end{aligned}$$

This leaves two unknowns. Analysing mass flow through the power turbine gives:

$$\begin{aligned} &\dot{m} = \rho\dot{\mathrm{V}} \\ &\dot{m} = \rho A C_a \\ &C_a = \frac{m}{A\rho} \end{aligned} \qquad (0.13)$$

Where: ρ is the density of the gas, and A is the area of the anulus. Referring to Figure 64 the outlet exhaust path maintains a constant area implying that little expansion or compression of exhaust gases occurs (from continuity equation), thus it is reasonable to assume that the pressure at the exit from the power turbine is close to atmospheric. Rearranging the perfect gas law and assuming operation at low altitude (as in take off conditions) the density ρ at the turbine exit can be determined:

$$\rho = {}^{P}\!\big/_{RT}$$

$$\rho_{exit} = {}^{100\ \ kPa}\!\Big/_{287.05\left[{}^{J}\!/_{kg\cdot K}\right]\ \ 873\ \ {}^{\circ}K}$$

$$\rho_{exit} = 0.3991\left[{}^{kg}\!/_{m^2}\right] \tag{0.14}$$

$$\text{or at cruise alltitude} \quad P = 60\ \ kPa$$

$$\rho_{exit} = 0.2394\left[{}^{kg}\!/_{m^2}\right]$$

Substituting (0.6) into (0.7) the axial speed can be determined, the results for a range of mass flows are displayed in Figure 63. The axial velocity from which to re-construct the velocity triangles can be estimated as $C_A \approx 210 \leftrightarrow 300\ \ {}^{m}\!/_{s}$ at cruise altitude and $C_A \approx 200\ \ {}^{m}\!/_{s}$ during take-off. Therefore, a C_A value of $225\ \ {}^{m}\!/_{s}$ is chosen in this study. These values seem reasonable.

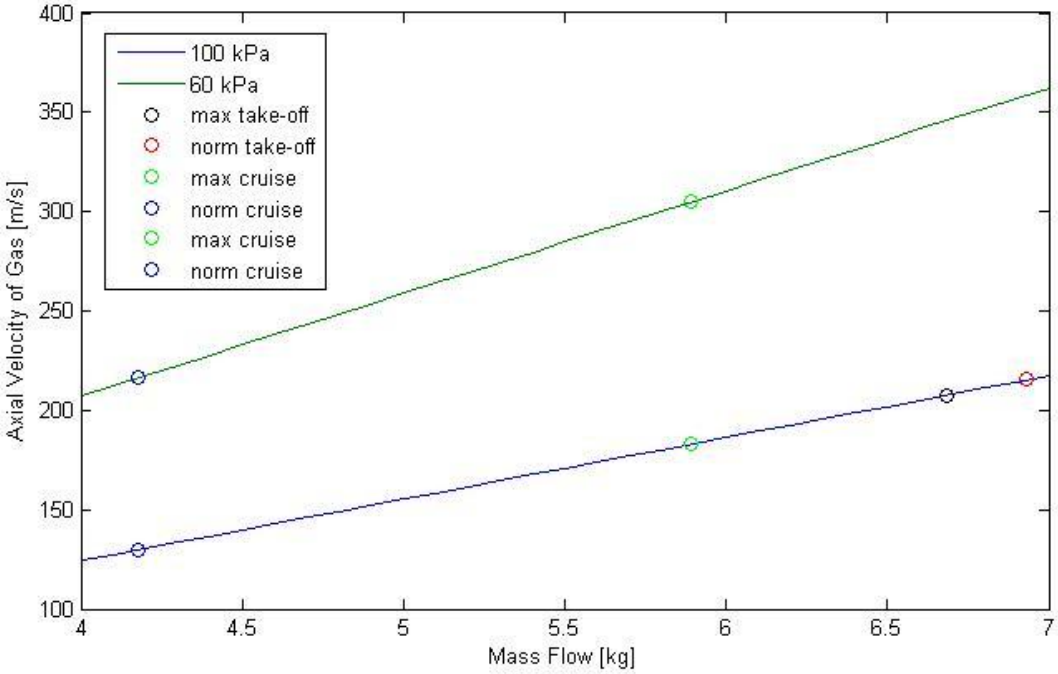

Figure 63: Axial velocity of gas for a corresponding mass flow

Assuming the exit gas velocity from the turbine to be purely axial ($\alpha_3 = 0$) equation (0.9) at normal cruise conditions can be solved:

$$\frac{290}{225} = \tan\beta_3 - \tan\ 0$$
$$\angle\beta_3 = \arctan\ {}^{290}\!/_{225}$$
$$\angle\beta_3 = 52°$$

At take-off conditions: $\angle\beta_3 = 58°$

It is reasonable to assume that the designed exit angle from the rotor blade is 54°. As no data on temperature is available in-between the power turbine stages and assuming that both stages have the same mean line geometry (with respect to gas velocity) the work is evenly divided between both stages. Rearranging (0.4) and applying assumptions yield (@cruise conditions):

$$\tan\beta_2 = \frac{W_S}{UC_a} - \tan\beta_3$$
$$\beta_2 = \arctan\left(\frac{425\ kW}{290\quad 214} - \tan\ 54° \right)$$
$$\beta_2 = 25° \text{@ norm cruise conditions}$$
$$\beta_2 = 28° \text{@ max take-off conditions}$$

Averaging and weighting to normal operating conditions the designed angle will be taken as $\beta_2 = 26°$. Solving for the rest of the velocity triangle yields:

$$\left.\begin{aligned} V_3 &= 353\ {}^{m}\!/_{s} \\ \alpha_2 &= 63° \end{aligned}\right\}\text{@ at norm cruise}$$
$$\left.\begin{aligned} V_3 &= 392\ {}^{m}\!/_{s} \\ \alpha_2 &= 66° \end{aligned}\right\}\text{@ at max take-off}$$

Analysing Figure 60 and calculating the hub tip ratio yield a value of approximately 0.6. At hub-tip ratios greater than 0.4, particularly in lower pressure turbines, the mean flow analysis is not considered accurate and 3d flow analysis must be used [54]. A twist can be added to the blade to create a radial variation in gas density to maintain a condition of radial equilibrium. At a radius *r* the gas angles are:

$$\begin{aligned}\tan\beta_2 &= \left(\frac{r_m}{r}\right)_2 \tan\alpha_{2m} - \left(\frac{r}{r_m}\right)_2 \frac{U_m}{C_a}\\ \tan\beta_3 &= \left(\frac{r_m}{r}\right)_3 \tan\alpha_{3m} - \left(\frac{r}{r_m}\right)_3 \frac{U_m}{C_a}\end{aligned} \tag{0.15}$$

This yields:

$$\begin{aligned}\beta_2(tip) &= -8^\circ\\ \beta_2(root) &= 58^\circ\\ \beta_3(tip) &= 61^\circ\\ \beta_3(root) &= 47^\circ\end{aligned}$$

This is a substantial twist to apply, particularly to the leading edge (60° twist tip-to-root) to be considered. This can be mitigated with the knowledge that the entrance gas velocity can vary within 15° without increasing the profile loss coefficient. However, this twist will also complicate blade bending force calculations as the primary axis of inertia as well as gas velocities will change over the entire length of the blade. For the purposes of this report no twist will be applied as the analysis would become unreasonably complicated.

Blade Profile Choice

With known gas angles and velocities a reasonable blade profile can be constructed. Due to the limited information available on actual blade geometry a basic T6 blade profile is chosen and adapted. Modifications may occur once the stress analysis begins. Using the chosen design inlet/exit angles and figure 7.14 from [79] an optimum pitch/cord ratio (*s/c)* of 0.825 can be determined. It is also known that the 2nd turbine stage contains a total of 74 blades. Using the circumference at mean blade radius, the pitch of the turbine can be determined as $s = 13.4\ \text{mm}$, and the cord length from the optimum ratio: $c = {}^{13.4}\!/_{0.8} = 16.8\ \text{mm}$. This is however less than the blade width at mean radius so the blade width will be chosen as the cord length.

Clearly from Figure 60 a linear taper is present within the blade which would beneficially reduce centrifugal loading on the blade.

Blade Stress - Centrifugal Force

Due to the high rotation speed of the blades and disk considerable centrifugal forces must be considered. It is important to design for the worst case scenario thus all centrifugal calculations are done at the maximum RPM which occurs during the “start” condition.

The greatest stress within a turbine blade from centrifugal loading is experienced at the root of the blade and is given by:

$$\begin{aligned} \sigma_r &= K 2\pi N^2 \rho A \\ \text{where } K &= \ 1+d_t \ /3+ \ a+d_t \ /3 \ 1+a \\ \text{and } a &= \text{hub-tip ratio} = R_r / R_t \\ d_t &= \text{tip area/root area} = A_t / A_r \end{aligned} \qquad (0.16)$$

This however does not take the weight of the shroud into account. Calculating the volume of the shroud from the geometric data in Figure 60 and knowing the density the weight can be determined and approximated to a point load acting on the tip of the blade through the center of gravity.

$$\begin{aligned} m_{shroud} &= \rho \left(\ 20.6\times10^{-6} \left[m^2 \right] \ \ 3\times10^{-3} \ m \ \ + \frac{49\times10^{-6} \ 2\pi \ r_{shroud}}{74} \right) \\ m_{shroud} &= 0.0068 \ kg \end{aligned}$$

The centrifugal stresses are clearly greatest when the turbine rotation is highest. This occurs during the start up condition. Using equation (0.16) and adding the resulting stress from the mass of the shroud the *maximum* stress at the root of the blade from centrifugal loading is:

$$\begin{aligned} \sigma_r &= K 2\pi N^2 \rho A + F_{shroud} / A_r \\ &= \ 0.6 \ 2\pi \left(\frac{1440 \ \text{rpm} \quad 17.2}{60} \right)^2 \ 8000 \left[{}^{\text{kg}}\!/_{\text{m}^3} \right] \ 0.0814 \left[\text{m}^2 \right] \\ &\quad + \ 0.0068 \ \text{kg} \quad 2594 \ {}^{\text{rad}}\!/_{\text{s}} \quad 200.1\times10^{-3} \ \text{m} \ \ /28.77\times10^{-6} \left[\text{m}^2 \right] \\ &= 496 \ \text{Mpa} \ +243 \ \text{Mpa} \\ &= 740 \ \text{Mpa} \ @ \ \text{"start" 1440 prop rpm} \end{aligned}$$

[78]

The 0.2% yield strength (YS) of WASPALOY is 897 MPa and a “rough” guideline for design is to have a maximum of 70% YS present. At max loading conditions the stress present is 82%. This implies that the assumed cross-section is reasonably accurate but slightly under-designed. Alternately the assumed shroud geometry may be much heavier than actual. At the transient condition: 660 MPa, at 1200 rpm: 587 MPa, at normal cruise (85% RPM) 492 MPa (SF = 1.82). While this loading is brief (10s) it is still a very large, stress concentrations resulting from sudden changes of geometry at root tip or cracks and therefore can be critical.

Blade Bending Stress

Assuming the velocity profile and gas density are constant throughout the annulus (which surely deviates to some extent from reality) and neglecting compressibility effects the bending moment at the root can be estimated as: $M_\theta \approx \frac{mcW_S}{2nU_m}$ and in the rotor axial direction: $M_a = \frac{mcW_S \tan\beta_m}{2nU_m}$ [78]. Where $\beta_m = \beta_{2m} + \beta_{3m}$. The bending stress can then be calculated:

[78] $$\sigma_B = \frac{x}{I_{yy}}\ M_\theta \cos\phi - M_a \sin\phi\ - \frac{y}{I_{xx}}\ M_a \cos\phi + M_\theta \sin\phi \qquad (0.17)$$

From Figure 65 there is no angle between the principal moments of inertia and the axis $\phi = 0$.

Reducing (0.17) and substituting in values:

$$\sigma_B = \frac{x}{I_{yy}}\ M_\theta\ - \frac{y}{I_{xx}}\ M_a$$

$$\text{Leading edge:}\ \sigma_B = \frac{3.8\ \text{mm}}{829\left[\text{mm}^4\right]}\left[\frac{21.8\ \text{mm}\quad 1565\ \text{kW}}{2\ \ 74\ \ \ 341\ {}^{\text{m}}\!/_{\text{s}}}\right] - \frac{12.4\ \text{mm}}{781\left[\text{mm}^4\right]}\left[\frac{21.8\ \text{mm}\quad 1565\ \text{kW}\quad \tan\ 80^\circ}{2\ \ 74\ \ \ 341\ {}^{\text{m}}\!/_{\text{s}}}\right]$$

$$\sigma_B = 47\ \text{MPa}$$

$$\text{Trailing edge:}\ \sigma_B = 35\ \text{MPa}$$

AI.4 Figures

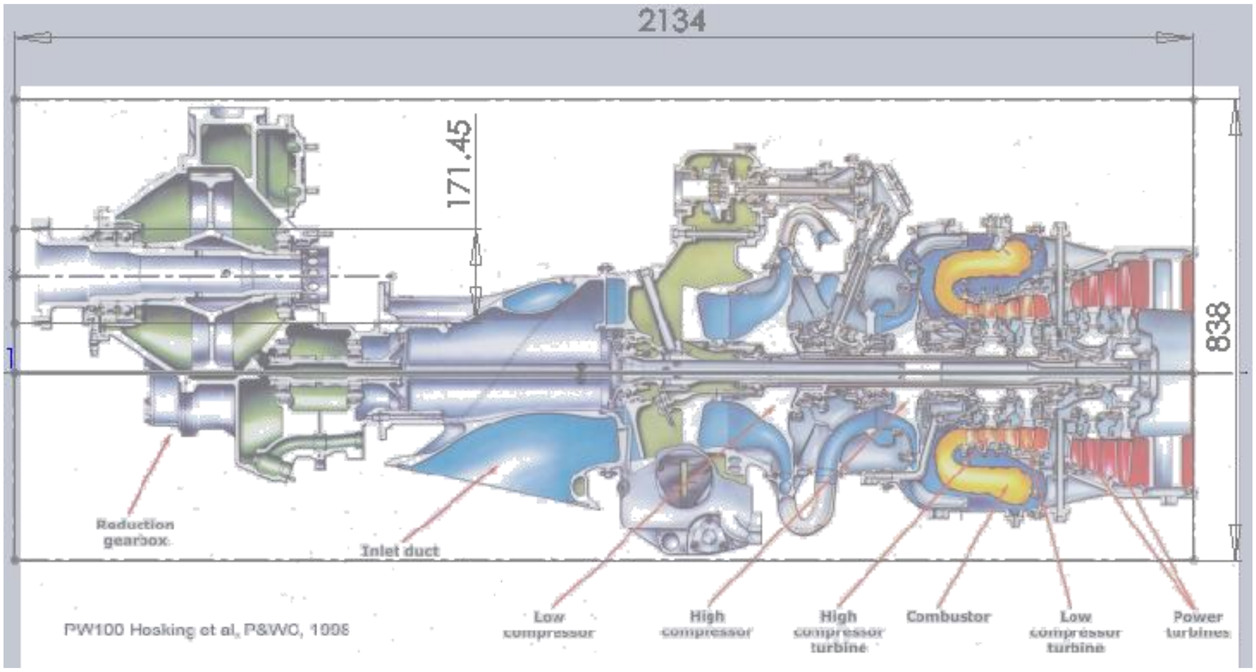

Figure 64: Scaled cross -section of PW-100

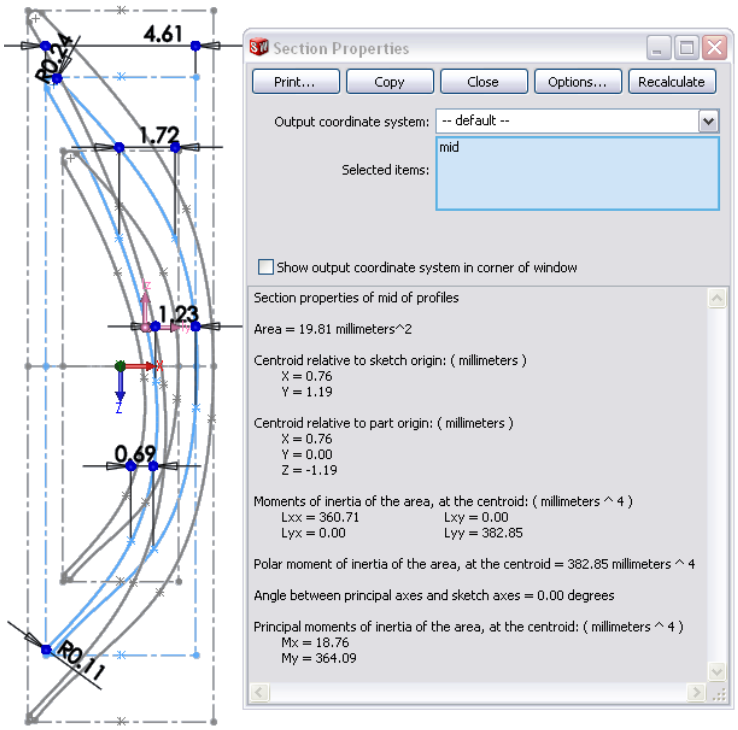

Output coordinate system: -- default --

Selected items: mid

☐ Show output coordinate system in corner of window

```
Section properties of mid of profiles

Area = 19.81 millimeters^2

Centroid relative to sketch origin: ( millimeters )
      X = 0.76
      Y = 1.19

Centroid relative to part origin: ( millimeters )
      X = 0.76
      Y = 0.00
      Z = -1.19

Moments of inertia of the area, at the centroid: ( millimeters ^ 4 )
      Lxx = 360.71                  Lxy = 0.00
      Lyx = 0.00                    Lyy = 382.85

Polar moment of inertia of the area, at the centroid = 382.85 millimeters ^ 4

Angle between principal axes and sketch axes = 0.00 degrees

Principal moments of inertia of the area, at the centroid: ( millimeters ^ 4 )
      Mx = 18.76
      My = 364.09
```

Figure 65: Mid-blade section properties

Appendix II. Blade Stress and Deflection Validation

The stress at the blade root for a uniform cross-section is given as $\sigma_{ct\ \ \max} = 2\pi N^2 \rho_b A$. [1].

Where (σ_{ct})$_{\max}$ is the max stress, *N* is the rotation of the disk (in rev/s), ρ_b is the density of the blade, and *A* is the area of the turbine annulus. The area for the theoretical annulus varies for the 2-D model and the three-dimensional model.

Convert 1500 rad/s -> *N* = 1500/2π = 239 rev/s

$$A = 2\pi \ \ r_{\text{tip of blade}}{}^2 - r_{\text{hub}}{}^2$$

For 2-D

$$A = 2\pi \quad 0.12 \ ^2 - \ 0.22 \ ^2$$

Area of the annulus is given as: $A = \ 1.068 \times 10^{-1} \ \left[\text{mm}^2\right]$

For 3-D

$$A = 2\pi \quad 0.12 \ ^2 - \ 0.8 \ ^2$$

$$A = \ 0.0804 \ \left[\text{mm}^2\right]$$

Substituting:

$$\sigma_{ct\ \ \max} = 2\pi \ \ 239 \ ^2 \ \ 8200 \quad 1.068 \times 10^{-1}$$

$$\sigma_{ct\ \ \max} = 3.14 \times 10^8 = 314 \ \text{MPa} \quad \text{for 2-D}$$

$$\sigma_{ct\ \ \max} = 2\pi \ \ 239 \ ^2 \ \ 8200 \quad 0.0804$$

$$\sigma_{ct\ \ \max} = 2.366 \times 10^8 = 237 \ \text{MPa} \quad \text{for 3-D}$$

Appendix III. Beam Approximation Validation

From: Mechanics of materials –sixth edition, James M. Gere, 2004 Brookes/Cole and

1. Gere, J.M., *Mechanics of materials*. 2004: Brooks/Cole.

Assuming a constant temperature obtained by averaging the nodal temperatures for the entire cross section. The modulus of elasticity is determined to be 156 [GPa].

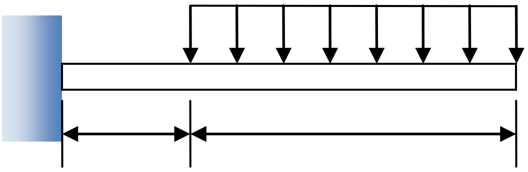

The deflection can be estimated as:

$$\delta_B = \frac{q}{24EI}\ 3L^4 - 4a^3L + a^4$$

$a = 0$ reducing yeilds:

$$\delta_B = \frac{q}{24EI}\ 3L^4$$

substituting values at average temperature values

Solving for moment of inertia

$$I = \frac{t^3 w}{12} = \frac{1\times10^{-2}\ {}^{3}\ \ 1}{12} = 83\times10^{-9}\left[\mathrm{m}^4\right]$$

$$\delta_B = \frac{19\times10^3\ \ \mathrm{N/m}}{24\ \ 156\times10^9\left[\mathrm{N/m}^2\right]\ \left(83\times10^{-9}\left[\mathrm{m}^4\right]\right)}\left(3\left(10\times10^{-2}\ [\mathrm{m}]\right)^4\right)$$

$$\delta_B = \frac{110\times10^3}{310752}\left(3\left(10\times10^{-2}\ [\mathrm{m}]\right)^4\right)$$

$$\delta_B = 1.83\times10^{-5}\ [\mathrm{m}]$$

This does not include the effect of the centrifugal load which in an undamaged blade should cause zero blade deflection. Also, this approximation does not include the effects of the imposed temperature distribution which would logically increase the tip deflection as the higher stresses in symmetric beam bending occur on the surface of the beam where the temperature as modeled is the highest.

Repeating for three-dimensional model and using a moment of inertia obtained from the solid works sketch of I_{xx}=42.21 [mm^4] = 42.21x10^{-12}[m^4] and multiplying the applied pressure load by the width to obtain the equivalent distributed load:

$$\delta_B = \frac{19000\left[\mathrm{N/m^2}\right]\ \ 0.021\ \mathrm{m}\ \ \ 0.08\ \mathrm{m}\ \ ^{4}}{8\ \ 148\times10^{9}\left[\mathrm{N/m^2}\right]\ \ 42.21\times10^{-12}\left[\mathrm{m^4}\right]}$$

$$\delta_B = 3.27\times10^{-4}\ \ \mathrm{m}$$

Appendix IV. Heat Transfer Calculations

Simplifying the problem to a one-dimensional heat transfer problem by considering only the change in the blade thickness direction, the heat transfer rate and intermediate temperatures can easily be determined using the Fourier's law [80]:

$$q_x = -kA\frac{dT}{dx} = \frac{kA}{L}\ T_{s,1} - T_{s,2} \qquad (0.18)$$

Where T_s is the surface temperature of the front and back plane walls, q_x is the heat transfer rate, *L* is the thickness of the plane wall, *k* is the thermal conductivity, *A* is the area of the wall normal to the direction of heat transfer.

A drop of approximately 200°C is expected from literature across both the TBC and substrate. The heat transfer is illustrated in Figure 66.

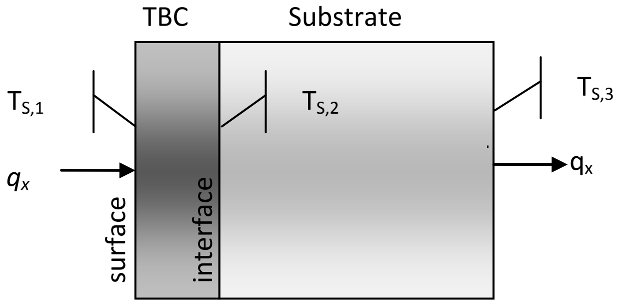

Figure 66: One-dimensional heat transfer across TBC and substrate

Rearranging (0.18) the heat flux across the TBC and the Substrate is defined as:

$$q''_x = \frac{q_x}{A} = \frac{k}{L}\ T_{s,1} - T_{s,2}$$

$$q''_x = \frac{1.6\ \mathrm{W/m\cdot K}\quad 1240\ \mathrm{K}\ - T_{s,2}}{0.0003\ \mathrm{m}} \text{ across the TBC} \qquad (0.19)$$

$$q''_x = \frac{23\ \mathrm{W/m\cdot K}\quad T_{s,2} - 1040\ \mathrm{K}}{0.0047\ \mathrm{m}} \text{ acoss the Substrate}$$

Setting equations 0.18 and 0.19 equal to each other and solving for $T_{s,2}$ yields a $T_{s,2} = 1138\ \text{K}$. Substituting the intermediate temperature value back into (0.19) yields a heat-flux needed to provide the desired temperature distribution.

$$q_x'' = 543966\left[\text{W/m}^2\right] \tag{0.20}$$

A 1 mm wide partition at the center of the cross section was used to represent the close proximity of a cooling channel. Applying (0.20) over this volume yields:

$$q_x''' = \frac{543966\left[\text{W/m}^2\right]}{0.001\ \text{m}} = 543966000\left[\text{W/m}^3\right] \tag{0.21}$$

However this calculation neglects the suction side of the blade. As symmetry exist in the material, geometry, and surface temperatures, an equal heat flux must also exists. Thus the heat flux arriving at the cooling channel is effectively doubled requiring a body heat flux of:

$$\begin{aligned} q_x''' &= 543966000\left[\text{W/m}^3\right]\times 2 \\ q''' &= 1087932000\left[\text{W/m}^3\right] \\ q''' &\approx 1\times 10^9\left[\text{W/m}^3\right] \end{aligned} \tag{0.22}$$

For simplicity a constant body heat flux of -1x10^9 W/m was used. The minus sign has been added to properly denote the heat transfer direction for Abaqus.